INFORMATION TO USERS

This manuscript has been reproduced from the microfilm master. UMI films the text directly from the original or copy submitted. Thus, some thesis and dissertation copies are in typewriter face, while others may be from any type of computer printer.

The quality of this reproduction is dependent upon the quality of the copy submitted. Broken or indistinct print, colored or poor quality illustrations and photographs, print bleedthrough, substandard margins, and improper alignment can adversely affect reproduction.

In the unlikely event that the author did not send UMI a complete manuscript and there are missing pages, these will be noted. Also, if unauthorized copyright material had to be removed, a note will indicate the deletion.

Oversize materials (e.g., maps, drawings, charts) are reproduced by sectioning the original, beginning at the upper left-hand corner and continuing from left to right in equal sections with small overlaps.

Photographs included in the original manuscript have been reproduced xerographically in this copy. Higher quality 6" x 9" black and white photographic prints are available for any photographs or illustrations appearing in this copy for an additional charge. Contact UMI directly to order.

ProQuest Information and Learning
300 North Zeeb Road, Ann Arbor, MI 48106-1346 USA
800-521-0600

BETA AND ELECTRON DOSE IMAGING USING A MICROSPECTROPHOTOMETER SYSTEM AND RADIOCHROMIC FILM

By

GORDON H. CHAN, B.Sc., M.Sc.

A Thesis

Submitted to the School of Graduate Studies

in Partial Fulfilment of the Requirements

for the Degree

Doctor of Philosophy

McMaster University

BETA AND ELECTRON DOSE IMAGING

DOCTOR OF PHILOSOPHY (1999) McMaster University
(Physics) Hamilton, Ontario

TITLE: Beta and Electron Dose Imaging Using a Microspectrophotometer System and Radiochromic Film

AUTHOR: Gordon H. Chan, B.Sc. (University of British Columbia)
M.Sc. (University of Waterloo)

SUPERVISOR: Professor W. V. Prestwich

NUMBER OF PAGES: xiv, 223

ABSTRACT

A dose imaging technique of measuring the distribution of beta particles and high energy electrons, using a microspectrophotometer system and radiochromic film, has been investigated. The investigation entailed the commissioning of the microspectrophotometer and the development of a newly proposed method in film calibration. It was tested successfully by comparing the measured dose, determined using the calibration method, of films irradiated by a ^{32}P source, and the expected dose, determined by beta counting based on the equilibrium geometry with dose loss correction to the film substrate (20%). This method was also demonstrated to extend the usable dose range of the film.

The dose imaging technique was applied to two experiments. The first experiment examines the beta depth dose distribution in Lucite, irradiated by a ^{32}P volume source. The experimental results were compared to Monte Carlo simulation, performed using the ITS code. The experimental distributions were found to agree closely with the Monte Carlo values up to a depth of 3 mm, but were significantly higher beyond.

The second experiment examines the electron dose distribution in Lucite, irradiated by a narrow 10 MeV electron beam. The lateral experimental dose distributions were found to agree well, except at the tail end, with Monte Carlo values up to about 20 mm depth. Elsewhere, the experimental dose was found to be higher. The

disagreement with Monte Carlo simulations at low doses in both experiments perhaps indicates a real discrepancy; further experimental investigations are required. The lateral spread of the beam was also investigated by determining the linear scattering power. The experimental values of the linear scattering power were found to be smaller than those quoted in the ICRU report 35 by a factor of 1.8 or less.

ACKNOWLEDGEMENTS

The completion of this thesis represents the end of my academic journey at the graduate level. This journey, which began over 5 years ago, has been arduous and filled with many hurdles. Fortunately, there have been many wonderful people along the way who have helped me overcome these obstacles. These people truly deserve my recognition.

First and foremost, I would like to thank my supervisor, Dr. W. V. Prestwich, who did not hesitate to take on a student who could have easily fallen into academic oblivion. With his guidance, patience, constant encouragement, and infinite number of ways of explaining things, I was able to complete this thesis with relatively few bumps and bruises. I have also learned a great deal from his wisdom, vast experience in life, always positive attitude, and his interpersonal skills. It has been a great pleasure and privilege to work with him.

Special thanks to the other two members of my supervisory committee, Dr. C. Webber, for providing numerous suggestions on improving my work, and Dr. T. Farrell, for generously donating his time and energy in helping with my research problems. Both members also have great sense of humour, which makes working with them much more enjoyable and productive.

I am grateful to the technician, Kenrick Chin, who maintained most of the research equipment that were involved in this thesis. I would also like to acknowledge

the health physics people, especially Steve Staniek, for overseeing the safety aspects of all the experiments and providing helpful suggestions.

I am especially appreciative to George Alexandrakis for being such a great friend and keeping me from going insane on numerous occasions. He also contributed many great ideas on various topics of my thesis. My appreciation is extended to my other great friends: Cheryl Brown for proofreading my thesis and being a great buddy and listener, Marcel Marcu who never failed to lend a helping hand, Joanne O'Meara for being a "Dana Scully" (a character on the X-Files) to me, Michelle Arnold who would laugh at all my stupid jokes and antics, and Rob and Lynn Reid for remembering me on every important occasion. I am also indebted to the continuous support given by Dr. Kristin Schleich. She has always given me valuable advice and resources.

My many current and previous officemates had to put up with my unique behaviour and many strange ideas, and yet, they made me feel very welcomed. They deserve to be acknowledged – Tamie Peopping, Marie-Claude Asselin, Fiona McNeill, Jose Brito, Rebecca Murphy, Rebeccah Marsh, and Aslam. I am also thankful to several of my online friends, such as ginee, di, eagles, shark, and maggie. They kept me company while I was burning the late night cathode-ray tube.

I am very much grateful to my family who is always the first to give me the seal of approval. Special thanks to Uncle Zabin and Aunt Connie for being so accommodating and constantly looking after me, and Uncle Dominic and Aunt Amy who offered me wonderful advice. I would also like to acknowledge my cousin, Alyssa, who despite being subjected to my constant whining, remains a great supporter and listener.

Finally, I would like to thank my parents for their unconditional support and encouragement. I am thankful that my dad, who got me interested in chess early in my childhood, gave me the much needed analytical skills required for this thesis.

TABLE OF CONTENTS

LIST OF ILLUSTRATIONS

LIST OF TABLES

CHAPTER 1

INTRODUCTION

Radiation is a process that involves emission in the form of energetic particles or waves. It can occur naturally in our universe and on earth. It can also be artificially made. One of the more important aspects of radiation is its potentially harmful effects on humans and other living organisms. However, it also has many beneficial applications in medicine and industry. Therefore, there has been an enormous amount of research directed toward the development of radiation dosimetry, which involves the determination of radiation dose deposited in a medium by ionization radiation.

In many medical applications, it is imperative to determine the dose accurately and precisely, preferably with high spatial resolution. For example, in cancer treatment, a low estimation of the required dose may not kill a cancerous tumour completely, while an overdose may potentially harm the patient. Currently, the dose deposition in homogeneous media is well understood. But in most cases, the media of interest, such as organs or tumours, are usually surrounded by other inhomogeneous matter. Although the physics of electron interactions with matter is well established, the dose deposition in inhomogeneous media remains an active field of research. There have been many theories, algorithms, and simulations developed to solve the inhomogeneous case. But there are still insufficient experimental data to verify them because most detectors suffer from a lack of spatial resolution, accuracy, or precision. Fortunately, in recent years, the

development of radiochromic films has improved to a point where accurate, high spatial resolution dose imaging is possible. However, the techniques to scan the films are still being developed, mainly to improve the accuracy and the precision.

The goal of the research conducted for this thesis is to develop a new technique in beta and electron dose imaging, using the radiochromic film scanned by a microspectrophotometer system. The methodology is then verified by an intercalibration between gamma and beta irradiations. The technique will be applied to two cases where the electron dose distribution within a homogeneous phantom is measured. The dose distribution will then be compared with known theoretical or expected results. The success of the research will pave the way for dose determination in other cases, such as an inhomogeneous medium. Potential medical applications are plentiful, such as those given by the American Association of Physicists in Medicine (AAPM) Task Group 55 (Niroomand-Rad *et al.* 1998) – ophthalmic applicator dosimetry, brachytherapy and intravascular brachytherapy dosimetry, interface dosimetry, stereotactic radiosurgery dosimetry, radiotherapy beam dosimetry, hot particle dosimetry, proton dosimetry, and possibly neutron dosimetry.

The outline of the thesis is as follows. The thesis is divided into 8 chapters. The first chapter is the introduction and gives the rationale of the research conducted. The background and the theories related to the research form the basis of Chapter 2. In particular, the chapter will first review the physics of electron interactions with matter, followed by the theories of electron dose distribution. It concludes by examining the current research and background of the radiochromic films. Chapter 3 describes the

instruments, namely the microspectrophotometer and its complimentary components, and the work into commissioning them, which involves investigating the stability, the sensitivity, and the resolution, etc. The experimental procedures in carrying out the gamma calibration of the film, the beta irradiation of the film to test the methodology, and the two experiments in which homogeneous phantoms were irradiated by beta rays and electrons, are described in Chapter 4. It is followed by Chapter 5, where a new method in determining dose from measured optical density of irradiated radiochromic films is proposed and discussed, along with the testing of its feasibility. Then the results from all the experiments conducted are shown in Chapter 6. The discussion and the comparison of these results with theories or Monte Carlo simulations are given in Chapter 7, followed by the conclusions in the final chapter.

CHAPTER 2

BACKGROUND AND THEORY

The field of radiation dosimetry began when X-rays were discovered by Wilhelm Röntgen in the 1890s. Since then, the field has expanded rapidly, and applications involving radiation soon followed. Today, the number of applications in industry, and medical diagnosis and treatment is innumerable and growing. Therefore, it is very important that the amount of radiation dose deposited in a medium be correctly predicted. So far, there have been numerous theories and methods in dose calculation and prediction. These theories and methods are still evolving and are constantly being tested and verified by experiments. While there have been many dosimeters developed to measure dose accurately on a macroscopic scale, it is only recently that technological advances in dosimeters enable such measurements to be performed on a smaller scale. In this chapter, the general background and theory of ionizing radiation related to the research conducted for this thesis will be described, followed by the background of radiochromic film.

2.1 Ionizing radiation

Ionizing radiation is generally characterized by the ability of incident particles to cause ionization or excitation of the atoms of a medium with which they interact. The common types of particles responsible for ionizing radiation are X-rays, gamma rays, beta

particles, fast electrons, neutrons, protons, alphas, and heavy charged particles. Of these particles, emphasis will be on beta particles and electrons since they are the main focus of this thesis.

2.1.1 Gamma rays and X-rays

Gamma rays (γ) are neutral quanta, referred to as photons, and a form of electromagnetic radiation emitted by unstable nuclei. The nuclei can either be naturally unstable as in the case of some naturally occurring isotopes, or they can be made unstable by nuclear interactions. Both processes can lead to excited nuclei that decay to the ground state by emitting one or more quanta of gamma radiation. It should be noted that γ-rays and X-rays of a given energy have identical properties. But X-rays originate from charged particles by changing atomic energy levels or slowing down in a Coulomb force field (Bremsstrahlung). The energy of gamma radiation is typically measured in MeV.

2.1.2 Beta particles and electrons

Beta particles (β) can either be positively or negatively charged. But discussion will be restricted to negatively charged β particles since they are the only ones involved in the research. As analogous to the relationship between γ- and X-rays, β particles and electrons of a given energy have identical properties, but differ in mode of origin. β particles are emitted during a beta decay that results from a spontaneous nuclear transformation. But electrons originate from atomic states, rather than nuclear states.

These electrons can be liberated, by heating a conductor for example, or by interactions such as the ionization from external photo interactions (photoelectric, Compton, or pair production) or internal orbital interactions (internal conversion or Auger electrons).

2.2 Radiation dosimetry

The study of radiation dosimetry requires the knowledge or understanding of the quantifiable effects radiation has on the interactions with a medium. The fundamental quantity of radiation dosimetry is the energy imparted by ionizing radiation to the matter in a volume (ICRU 1980). ICRU (1980) defines the absorbed dose, d, as the expectation value of the energy, $\overline{E}$, imparted per unit mass, m, of an infinitesimal volume, ΔV,

$$d = \lim_{m \to 0} \frac{\overline{E}}{m} = \lim_{V \to 0} \frac{1}{\rho} \frac{\overline{E}}{V}, \tag{2.1}$$

where ρ is the density of the matter. The amount of dose deposited depends on the interaction between the incident ionizing particles and the absorbing medium.

2.3 Electron interaction with matter

The interaction of electrons with matter has been extensively studied. By the end of the 1960's, basic electron transport theories were well established. Several review papers and texts have been published (Evans 1955, Rossi 1952, Bethe and Ashkin 1953, Birkhoff, 1958, Berger, 1963, Zerby and Keller 1967). The predominant electron interaction through matter is through Coulomb collisions and can be characterized by inelastic scattering and elastic scattering. Inelastic scattering occurs when incident

electrons lose energy to an absorbing medium, resulting in excitation, ionization, and possibly production of secondary particles, while for elastic scattering, no excitation occurs. Typically, a high energy electron experiences tens of thousands of collisions before coming to rest. For example, a 1 MeV electron typically undergoes about 10^4 – 10^5 collisions until it loses all of its kinetic energy (Attix 1986 (Chap 8), Berger and Wang 1988). To predict the path of an electron, information on the direction and energy of the electron, and the medium it travels through must be known. This information enables the calculation of the electron stopping power, range, and scattering cross section, etc, which form the basis of electron transport theories.

There are generally three types of electron Coulomb-force interactions, based on the closest distance between an incident electron and an atom of a medium, i.e. the impact parameter (b), and the atomic radius (a) (Attix 1986 (Chap 8)). If the electron passes an atom at a considerable distance ($b >> a$), the electron energy transfer to the atom is very small. This process is known as a soft or distant collision. This type of collision is the most numerous since it is the most probable type of interaction, and accounts for roughly half of the energy transferred to the medium. The second type of collision is known as the hard (also known as "knock-on") or close collision. This process occurs when the impact parameter is of the order of the atomic dimensions ($b \sim a$), resulting in the incident electron interacting primarily with a single atomic electron. The interaction leads to the ejection of the electron from the atom in the form of a δ-ray. Hard collisions are approximately treated as elastic electron-electron collisions, and they occur with much less probability than soft collisions. However, due to the large fraction of kinetic energy

loss of the incident electrons in the production of δ-rays, the hard collisions account for roughly the same fraction of energy loss as the soft collisions. Both processes are types of inelastic scattering. The third type of process involves Coulomb force interaction between the incident electron and the external nuclear field of the nucleus. This type of collision occurs when the electron passes very close to the nucleus ($b << a$), resulting in an elastic scatter in all but 2 to 3% of such encounters. In these other cases, the interaction is inelastic, and the electron is slowed down. The slowing down process is also known as radiative stopping and results in the production of a Bremsstrahlung photon, which can have a significant fraction of the incident electron energy. The probability of the production of Bremsstrahlung depends on the square of the atomic number, Z^2, of the absorbing medium (see Evans 1955 (Chap 20), Attix 1986 (Chap 8)).

The probability of an interaction between an incident electron and a target atom can be calculated from the scattering cross section. This cross section should be treated as the "effective area" between the two particles. In the case of the inelastic interactions, an important parameter defined below is the stopping power, which gives information on the energy loss of the incident electrons. The stopping power is related to the probability of interaction, thus the cross section.

The stopping power, $S(E)$, is defined as the expectation value of the rate of energy loss per unit of path length x by a charged particle with kinetic energy E in a medium:

$$S(E) = \frac{dE}{dx}. \tag{2.2}$$

With this definition, it is assumed that the energy lost by the particle in individual interactions is very small. But the frequency of interactions is so high that on a macroscopic scale, the particle seems to lose energy continuously, as if acted on by friction. This assumption is generally referred to as the Continuous-Slowing-Down Approximation (CSDA). Since the stopping power is dependent on the density of the medium, it is convenient to define the mass stopping power by dividing the stopping power by the density, $S(E)/\rho$.

Another important parameter in quantifying the electron path is the range. Attix (1986) defines the range, R, of a charged particle of a given type and energy in a given medium as the expectation value of the path length that it follows until it comes to rest (discounting thermal motion). Because of the different types of electron interaction involved, the electron's path is stochastic. Therefore, the end point of every electron with the same energy is not unique. This lack of uniqueness leads to a feature termed range straggling, defined as the fluctuation in path length for individual particles of the same initial energy. The range can be calculated theoretically in the CSDA. The CSDA range is just,

$$R_{\mathrm{CSDA}} = \int_0^{E_\circ} \frac{dE}{S(E)}, \tag{2.3}$$

where $E_\circ$ is the initial energy of the particle.

2.3.1 Inelastic interactions

As discussed earlier, there are different types of inelastic scattering. The amount of energy loss by electrons in inelastic scattering can be represented by the stopping power. Since there are two distinct processes, namely the collision and radiative stopping, that can slow down the electron, the stopping power can be separated into 2 components in general,

$$S(E) = S_{\text{col}}(E) + S_{\text{rad}}(E), \tag{2.4}$$

where the subscripts, "col" and "rad", denote collision and radiative, respectively. Generally, the collision stopping power dominates at low energy, while radiative stopping power dominates at high energy.

2.3.1.1 Collision stopping power

The collision stopping power is the stopping power due to both hard and soft collisions. It can be calculated, in the form of mass collision stopping power, by

$$\frac{S_{\text{col}}}{\rho} = NZ \int_0^{W_m} W \frac{d\sigma_{\text{in}}}{dW} dW, \tag{2.5}$$

where N is the number of atoms per gram of the absorbing medium, Z is the atomic number, W_m is the largest possible energy transfer, and $d\sigma_{in}/dW$ is the differential cross section for the transfer of energy W from the incident particle to an atomic electron. The differential cross section is different for hard and soft collisions. Hence the mass collision stopping power must be separated into two components depending on some cutoff transfer energy value. The treatment of mass collision stopping power due to the

hard collision has been achieved by Møller (1932), while the soft collision case has been treated by Bethe (ICRU 1997 and references therein) on the basis of the Born approximation, which assumes that the incident electron velocity is much greater than the maximum Bohr-orbit velocity of the atomic electrons (see ICRU 1984b, Attix 1986 (Chap 8)). The details of the treatment and their respective differential cross sections are beyond the scope of the background of this thesis and will not be discussed further. The combined result is,

$$\frac{S_{col}}{\rho} = \frac{2\pi r_e^2 m_e c^2}{\beta^2} \frac{ZN_A}{M_A} \left\{ \ln\left[\left(\frac{E}{I}\right)^2 \left(1+\frac{\tau}{2}\right) \right] + F^-(\tau) - \delta - \frac{2C}{Z} \right\}, \qquad (2.6)$$

where for incident electrons,

$$F^-(\tau) = \frac{1+\frac{\tau^2}{8} - (2\tau+1)\ln 2}{(\tau+1)^2}, \qquad (2.7)$$

and r_e is the classical electron radius, $m_e c^2$ is the electron rest energy, β is the velocity of the incident electron divided by the velocity of light (note: $\beta^2 = 1 - (\tau+1)^{-2}$), $\tau \equiv E/m_e c^2$, E is the electron kinetic energy, Z is the atomic number and M_A is the molar mass of the absorbing medium, N_A is the Avogadro's constant, I is the mean excitation energy of the medium, δ corrects for the density effect that causes a reduction of the collision stopping power due to polarization of the medium by the passing charge (see, e.g., Sternheimer *et al.* 1982, ICRU 1984b, Attix 1986 (Chap 8)), and C/Z is the shell correction term that corrects for the invalidity of the Born approximation at low incident electron velocity (Bichsel 1968, Attix 1986 (Chap 8)).

2.3.1.2 Radiative stopping power

The radiative stopping power is more complicated than its collision counterpart. It can be calculated, in the form of mass radiative stopping power analogous to equation (2.5),

$$\frac{S_{\text{rad}}}{\rho} = NZ \int_0^{W_n} W \frac{d\sigma_n}{dW} dw + Z \int_0^{W'} W \frac{d\sigma_e}{dW} dW , \tag{2.8}$$

where $d\sigma_n/dW$ is the differential cross section for the emission of a photon of energy W due to interaction of the electron with the screened Coulomb field of the atomic nucleus, $d\sigma_e/dW$ is the corresponding differential cross section due to the electron interaction with the screened Coulomb field of one of the atomic electrons, W' is the upper limit of the Bremsstrahlung photons that can be emitted in the electron-electron interactions. The differential cross sections in the above equation are nontrivial and are dependent on the incident electron energy. Several papers based on various models and approximations have been published to calculate these cross sections (see e.g., ICRU 1984b, Seltzer and Berger 1985, Seltzer and Berger 1986). The combined result is,

$$\frac{S_{\text{rad}}}{\rho} = \alpha r_e^2 Z^2 \frac{N_A}{M_A} \left(E + m_e c^2\right) \phi_{\text{rad}} , \tag{2.9}$$

where α is the fine structure constant, ϕ_{rad} is a scaled dimensionless integrated Bremsstrahlung energy-loss cross section dependent on the kinetic energy and the atomic number.

2.3.2 Elastic interactions

In elastic interactions between an incident electron and the nucleus, the electron's path is deflected approximately without energy loss. The probability of this occurrence is described by the differential cross section with respect to the solid angle of the elastic scattering of the electrons, $d\sigma_{el}/d\Omega$. Classically, the elastic scattering of two unlike charged particles with non-relativistic energies due to the Coulomb force is described by the Rutherford differential cross section. In the case of an incident electron interacting with a nucleus with charge Ze,

$$\frac{d\sigma_{\text{Ruth}}}{d\Omega} = r_e^2 Z^2 \left[\frac{\tau+1}{\tau(\tau+2)}\right]^2 \frac{1}{(1-\cos\theta)^2}, \tag{2.10}$$

where θ is the scattering angle. This equation is actually not valid for extremely small angle scattering because it does not take into account the scattering by the electrons in the atom. Therefore, to account for this screening effect, an atomic form factor $F(\theta)$ has been introduced to replace Z by Z-$F(\theta)$ in the above equation (see e.g., Bethe and Ashkin 1953). Furthermore, the equation also assumes that the nucleus is a point charge. If the finite size of the nucleus were to be taken into account, the Z in the above equation would be replaced by a nuclear form factor. In addition, electrons travel at great speed even at "low" energy. For example, a 100 keV electron travels at greater than $0.5c$ in air. Therefore, the Rutherford differential cross section must be modified to include relativity. This modification was achieved by multiplying the Rutherford differential cross section by a factor, which takes spin and relativistic effects into account, using the theory of Mott

(1929). The exact elastic differential scattering cross section is not trivial, and Motz *et al.* (1964) have reviewed numerous models and approximations to the elastic differential cross sections.

2.4 Dose calculations

The absorbed dose was defined earlier in equation (2.1). From that definition, ICRU (1984a) gives a more useful expression for dose deposited due to charged particles:

$$d(\boldsymbol{r}) = -\frac{1}{\rho}\int_{4\pi}\int_{0}^{\infty}\left[\frac{dE}{dx}\widetilde{\Phi}(E,\boldsymbol{\Omega},\boldsymbol{r}) + E\frac{d\widetilde{\Phi}(E,\boldsymbol{\Omega},\boldsymbol{r})}{dx}\right]dEd\Omega, \tag{2.11}$$

where $\widetilde{\Phi}(E,\boldsymbol{\Omega},\boldsymbol{r})\,dEd\Omega$ is the number of electrons that, at a point $\boldsymbol{r}$ with energy E in the interval dE, pass through a unit area with normal in the direction $\boldsymbol{\Omega}$ within the interval of solid angle $d\Omega$, and dE/dx is the total stopping power. The first term in the integrand is the contribution from electrons that deposit a fraction of their energy in the interval dx, and the second term can be interpreted as arising from the electrons that stop within the interval dx. The contribution from the second term is usually very small. In the CSDA, the second term can be dropped, leading to the CSDA dose,

$$d(\boldsymbol{r}) = \int \frac{S(E)}{\rho}\Phi(E,\boldsymbol{r})dE\,. \tag{2.12}$$

This CSDA dose equation is essentially correct provided that electronic equilibrium is established. Electronic equilibrium exists for a volume V if the energy carried by electrons entering V is equal to the energy carried by electrons leaving V. In most cases, the fluence of the incident electrons is very difficult to determine. One method of finding

the fluence is to solve the radiative transport equation, which will be discussed in the next section.

One important product of equation (2.12) is that the absorbed dose due to electrons slowing down in one medium can be obtained by determining the absorbed dose in another medium and the ratio of the mass stopping power of the two media, provided the fluence is the same in both media:

$$\frac{d_{m1}(r)}{d_{m2}(r)} = \frac{\int \left(\frac{S(E)}{\rho}\right)_{m1} \Phi(E,r)dE}{\int \left(\frac{S(E)}{\rho}\right)_{m2} \Phi(E,r)dE} = \frac{(\bar{S}/\rho)_{m1}}{(\bar{S}/\rho)_{m2}}, \tag{2.13}$$

where the subscripts, $m1$ and $m2$, denote media 1 and 2, respectively. For most materials, the mass stopping power ratio is almost independent of energy of the electrons, except at very low energy where the excitation potential, I, is important, or very high energy where radiative process becomes important. This equation also forms the basis for the famous Bragg-Gray cavity theory (see e.g., Attix 1986), with the (unrestricted) mass collision stopping power ratio replacing the total mass stopping power ratio, thus ignoring the production of Bremsstrahlung photons.

2.4.1 Cavity theory

The Bragg-Gray theory states that if a small cavity is introduced into a medium, assuming the cavity is so small that its presence does not affect the electron spectrum in the medium, the dose in the medium can be determined by the dose in the cavity, or vice

versa, by equation (2.13). However, the Bragg-Gray theory does not take into account the loss of dose deposition by high energy secondary particles, such as δ-rays created by the primary electrons as a result of the hard collision. Hence the use of unrestricted mass collision stopping power will slightly overestimate the actual absorbed dose. As a result, several expressions based on the Spencer-Attix formulation (Spencer and Attix 1955) of the Bragg-Gray cavity theory using restricted collision stopping power have been introduced (Andreo 1988). The Spencer-Attix formulation replaces the unrestricted mass (collision) stopping power in equation (2.13) by the restricted mass collision stopping power, which is defined as the fraction of the mass collision stopping power that includes all the soft collisions plus those hard collisions resulting in δ-rays with energies less than a cutoff value (Attix 1986). This cutoff energy is dependent on the cavity size. Therefore, the Spencer-Attix formulation accounts for the absorbed dose from all generations of electrons and the cavity size.

2.4.2 Dose point kernel

Another method of evaluating the absorbed dose in a medium is through the use of the dose point kernel (Loevinger 1950). The dose point kernel refers to the dose distribution, $K(\boldsymbol{r} - \boldsymbol{r}')$, produced at a distance $|\boldsymbol{r} - \boldsymbol{r}'|$ by a point source. Then the dose at any distance $\boldsymbol{r}$ can be determined by the convolution between the dose point kernel and the source strength,

$$d(\boldsymbol{r}) = \int_V K(\boldsymbol{r} - \boldsymbol{r}') Y_\bullet(\boldsymbol{r}') d^3\boldsymbol{r}', \tag{2.14}$$

where $Y_o(r')$ is the source density. The dose point kernel method is applicable to any type of radiation. A corollary of this point kernel method is the plane kernel method, and they can be derived from each other. Using the plane kernel method, the dose at any distance x is determined by the convolution between the plane kernel and the plane source strength.

2.5 Radiative transport

The general theoretical expression for radiative transport is given by the Boltzmann equation. Luo and Brahme (1993) have given an overview of the transport of charged particles using this equation and its approximations. The Boltzmann equation is a unified theory for the transport of all charged and neutral particles. In its general form, with symbol tilda, ~, denoting a derivative with respect to the solid angle Ω (i.e. $\partial / \partial \Omega$), the time-independent Boltzmann equation is,

$$\begin{aligned} \Omega \cdot \nabla \tilde{\Phi}(E,\Omega,r) + \left(\mu + \lambda_s^{-1}\right)\tilde{\Phi}(E,\Omega,r) \\ = \tilde{Y}(E,\Omega,r) + \int\int \tilde{\mu}(E,\Omega \mid E',\Omega',r)\tilde{\Phi}(E',\Omega',r)dE'd\Omega', \end{aligned} \tag{2.15}$$

where $\tilde{\Phi}$ is the angular fluence, μ is the total interaction coefficient (or more commonly, linear attenuation coefficient), λ_s^{-1} is the mean free path for decay, $\tilde{Y}$ is the angular source density, $\tilde{\mu}(E,\Omega \mid E',\Omega',r)$ is the angular interaction coefficient taking the particles in the group with energy and direction (E',Ω') to (E,Ω). Note that the angular interaction coefficient is related to the differential cross section by $\tilde{\mu} = n\tilde{\sigma}$, where n is the particle number density.

2.5.1 Continuous slowing down approximation

For electrons, if the CSDA is assumed, then the last term in the Boltzmann equation can be divided into elastic and inelastic scattering. The result is,

$$\Omega \cdot \nabla \tilde{\Phi}(E,\Omega,r) = \tilde{Y}(E,\Omega,r) + \int \tilde{\mu}(\Omega,r\,|\,\Omega',r)\left(\tilde{\Phi}(E,\Omega',r) - \tilde{\Phi}(E,\Omega',r)\right)d\Omega' + \frac{\partial}{\partial E}\left(S(E)\tilde{\Phi}(E,\Omega,r)\right), \tag{2.16}$$

where $\tilde{\mu}(\Omega\,|\,\Omega')$ represents the interaction coefficient in elastic scattering, and the last term containing the stopping power $S(E)$ represents the slowing down term due to inelastic scattering.

2.5.2 Equilibrium geometry

A useful limit to the Boltzmann equation is the so called equilibrium geometry approximation when the source density is independent of position. This approximation is valid when the source volume dimensions are greater than the range of the particles. In the case of electrons in the CSDA, the Boltzmann equation in the equilibrium geometry after integrating over all solid angles is reduced to,

$$\frac{d}{dE}\left(S(E)\Phi(E)\right) = -Y(E)\,. \tag{2.17}$$

2.5.3 Fermi-Eyges equation

An important approximation that describes electron transport is the Fermi equation (Rossi and Greisen 1941, Rossi 1952 (Chap 2)). This equation is particularly important in predicting the scattering of electron beams (see Section 2.6). Prestwich and Kus (1997) have derived the Yang diffusion equation (Yang 1951), which is a more generalized form of the Fermi equation (including the longitudinal distribution and energy loss), from the Boltzmann equation, using small angle approximation so that,

$$\begin{aligned} \Omega_x &= \sin\theta\cos\phi \approx \theta\cos\phi, \\ \Omega_y &= \sin\theta\sin\phi \approx \theta\sin\phi, \\ \Omega_z &= \cos\theta \approx 1. \end{aligned} \tag{2.18}$$

Then, by defining $\theta_x = \theta\cos\phi$, $\theta_y = \theta\sin\phi$, and ignoring the second order terms in θ_x and θ_y in the Yang equation, the Boltzmann equation was modified to

$$\frac{\partial\tilde{\Phi}}{\partial z} + \theta_x\frac{\partial\tilde{\Phi}}{\partial x} + \theta_y\frac{\partial\tilde{\Phi}}{\partial y} = \frac{1}{4}\mu\left\langle\xi^2\right\rangle\left(\frac{\partial^2\tilde{\Phi}}{\partial\theta_x^2} + \frac{\partial^2\tilde{\Phi}}{\partial\theta_y^2}\right). \tag{2.19}$$

Identifying $\mu\left\langle\xi^2\right\rangle$ as the linear scattering power, T, the above equation is the Fermi equation, which was solved by Eyges (1948) for a depth dependent scattering power as explained in Jette *et al.* (1983), Jette (1984), and Jette (1988). The solution is generally known as the Fermi-Eyges equation or formula. It should be noted that the Fermi equation can also be derived from the Fokker-Planck equation (Börgers and Larsen 1996a, Börgers and Larsen 1996b), which is a small-angle Taylor series approximation to the Boltzmann equation under the CSDA (Luo and Brahme 1993, Börgers and Larsen 1994).

2.5.4 Linear scattering power

The linear scattering power, T, is conventionally defined as the rate of increase of the variance in the angular distribution or the mean square angle of scattering with distance. It assumes the interaction is elastic and can be viewed as analogous to the stopping power in the inelastic collision. As in the case of the stopping power, the mass scattering power is defined as T/ρ to remove its dependency on the density of the medium. The mass scattering power can be calculated theoretically using a method that involves the differential elastic collision cross section, as suggested by Rossi (1952, Chap 2). Using this method, theoretical expressions for the mass scattering power were obtained and given in the ICRU report 35 (1985a) and ICRU report 56 (1997). But they differ slightly because of the choice of the screening angle, which takes into account the screening of the nucleus by the orbital electrons. The expression from the ICRU 56 is,

$$\frac{T}{\rho} = 4\pi r_e^2 Z(Z+1)\frac{N_A}{M_A}\left[\frac{\tau+1}{\tau(\tau+2)}\right]^2\left[\ln\left(1+\frac{1}{\chi_a^2}\right)-1+\left(1+\frac{1}{\chi_a^2}\right)^{-1}\right], \quad (2.20)$$

where χ_a^2 is the screening angle derived by Molière (1947) based on the Thomas-Fermi model,

$$\chi_a^2 = Z^{\frac{2}{3}}\left(\frac{\alpha}{0.885}\right)^2\frac{1}{\tau(\tau+2)}\left[1.13+3.76\left(\frac{\alpha Z}{\beta}\right)^2\right]. \quad (2.21)$$

2.6 Electron beam dose distribution

Electron beam therapy has become a very important tool in the radiation treatment of cancer. Therefore, clinically, it is imperative to determine accurately the electron dose distribution within the media of interest. Currently, the basic interactions of electrons are well understood. Many theories and algorithms based on the approximations to the Boltzmann equation (see Section 2.5) have already been developed. However, the determination of dose distribution in many clinical situations has not been consistently accurate to within 5%, especially in the presence of tissue inhomogeneities and body curvature. Although fairly accurate dose distributions have been obtained by the use of Monte Carlo simulation (see Section 2.7), the simulation usually takes a very long time to complete. Therefore, active research in the theory of electron beams is still ongoing, and a very comprehensive review article was published by Jette (1995).

Before effects on the dose by different electron beam shapes, tissue inhomogeneities, and body curvature can be examined, the dose determination from a simple pencil beam irradiating a homogeneous media must be well established. The pencil beam case is also very useful because any broad beam can be treated as made up of many individual pencil beams. Hence, the dose distribution from any irregular broad beam can be evaluated by summing over all the pencil beams that make up the broad beam. It is the pencil beam case that will be the focus of this thesis. In the early days, the dose distribution by an electron beam was determined by first measuring the distribution in a water phantom at a standard field size and source-to-surface distance (SSD) for a particular machine. Then the measured dose distribution was shifted or extrapolated

according to the actual field size, the SSD, and the body curvature. To account for the inhomogeneities in the patient, the depth dose distribution was multiplied by a predetermined scaling factor using the so called equivalent thickness methods. These methods have been reviewed by Jette (1995 and references therein). However, they are not based on electron transport theories, and studies such as those by Mori (1985) and Ogawa *et al.* (1987) have shown the inaccuracy of these methods.

Another theoretical approach in calculating the electron dose distribution was through the use of the age-diffusion theory. The theory began with the work by Bethe *et al.* (1938), and the general age-diffusion equation was given by Glastone and Edland (1952). The equation can also be derived from the Boltzmann equation. However, it was not until Kawachi (1975) that the theory was applied to the calculation of electron dose distribution. Since then, several models have been proposed to determine the dose distribution in homogeneous media or large inhomogeneities with reasonably accurate results (Jette 1995 and references therein). However, these models require a modification to the fundamental age-diffusion equation, thereby no longer satisfying the age-diffusion theory. The reason is that the electron beam path diffuses little until it reaches near the end of its range, where the diffusion process becomes dominant (Jette 1995).

Currently, there are a number of proposed theories in describing the electron beam transport. One theory that has gained much attention is the expansion and development of the Fermi-Eyges theory. The original Fermi-Eyges theory is based upon small-angle scattering of particles, satisfying equation (2.19). In two dimensions, that equation can be written as,

$$\frac{\partial \tilde{\Phi}}{\partial z} + \theta_x \frac{\partial \tilde{\Phi}}{\partial x} - \frac{T}{4} \frac{\partial^2 \tilde{\Phi}}{\partial \theta_x^2} = 0. \tag{2.22}$$

The Eyges' (1948) solution, for an incident electron pencil beam directed along the z-axis at the origin, is in Gaussian form,

$$\tilde{\Phi}(x, \theta_x, z) = \frac{\exp\left(- \dfrac{A_0 x^2 - 2A_1 x\theta_x + A_2 \theta_x^2}{A_0 A_2 - A_1^2} \right)}{\pi \sqrt{A_0 A_2 - A_1^2}}, \tag{2.23}$$

where the functions A_n (n = 1, 2 and 3) are dependent of depth,

$$A_n(z) = \int_0^z T(\xi)(z - \xi)^n \, d\xi \, . \tag{2.24}$$

Note that the angular fluence distribution only describes the transport of primary electrons, but not secondary particles. The three dimensional form of equation (2.23) is simply the product of the angular fluence $\tilde{\Phi}(x, \theta_x, z)\tilde{\Phi}(y, \theta_y, z)$ and can be integrated over the angles in x and y to remove its angular dependence. The result is,

$$\Phi(x, y, z) = \frac{\exp\left(- \dfrac{x^2 + y^2}{A_2(z)} \right)}{\pi A_2(z)}. \tag{2.25}$$

The primary dose distribution can then be determined using equation (2.12). Hence,

$$d(x, y, z) = \frac{S_r(x, y, z)}{\rho} \Phi(x, y, z), \tag{2.26}$$

where S_r / ρ is the restricted mass collision stopping power at (x, y, z). The variance of the radial distribution, $\sigma_r^2(z)$, or the mean square radial spread is related to the linear scattering power and can be determined by,

$$\sigma_r^2(z) = \frac{\int_0^{2\pi}\int_0^{\infty} r^2 d(r,\theta,z) r dr d\theta}{\int_0^{2\pi}\int_0^{\infty} d(r,\theta,z) r dr d\theta} \approx \frac{\int_0^{\infty} r^3 \Phi(r,z) dr}{\int_0^{\infty} r \Phi(r,z) dr} = A_2(z). \tag{2.27}$$

This equation is only accurate to perhaps 70% of the electron range (Jette 1995) because the definition of the scattering power implicitly assumes that the electrons will travel forever in the absorbing medium.

The Fermi-Eyges multiple scattering theory on electron scattering has been presented in papers or texts, such as Rossi (1952), Scott (1963), and Zerby and Keller (1967). But it was not until the early 1980's when it was used to determine the electron beam dose distribution (Brahme *et al.* 1981, Hogstrom *et al.* 1981, Werner *et al.* 1982). The Fermi-Eyges theory has it limitations, however. Since it is derived using the small-angle approximation, and only the lateral distribution is considered, the theory breaks down at the end of the electron range, where diffusion becomes dominant. Therefore, modifications to the Fermi-Eyges multiple scattering theory have been made. Hogstrom *et al.* (1981) used measured depth dose distribution of the electron beam to provide an input axial factor to compute the lateral dose distribution using the Fermi-Eyges theory. Werner *et al.* (1982) modified the Eyges' solution to the Fermi equation to account for the energy loss of electrons. Lax *et al.* (1983) used three Gaussian functions to construct the Gaussian radial profile of a pencil beam. These modifications, among several others

such as the moment method, the beam redefinition technique, and the representative path method, have been reviewed by Jette (1995 and references therein).

Jette and co-workers have developed the second order multiple scattering theory using second order small-angle approximations in solving the Fermi equation (later generalized to the Fokker-Planck equation and the Yang equation) in a series of papers (Jette 1988, Jette *et al.* 1989, Jette and Bielajew 1989, Jette 1991, Jette and Walker 1992, Jette 1996, Jette and Walker 1997). Although the second order multiple scattering theory provides significant improvement in accuracy over the original Fermi-Eyges equation, the theory does not take into account energy loss or large angle scattering. The neglect of large-angle scattering in the Fokker-Planck approximation has been shown to be inaccurate (Börgers and Larsen 1996b). The energy loss problem in the Yang equation was solved by Tulovsky *et al.* (1994) following Harder's formula (Harder 1965), but using the first order small angle approximation. Later, Prestwich and Kus (1997) derived the Fermi-Eyges equation directly, instead of resorting to the Taylor's expansion. They found good agreement between their results and Monte Carlo simulations.

Other theories in describing the multiple scattering of electrons include the Molière theory (Molière 1948) and the Goudsmit-Saunderson theory (Goudsmit and Saunderson 1940). Both theories can be obtained from the Boltzmann equation (Luo and Brahme 1993), but without energy loss. The Molière theory assumes small angle scattering and uses first order small angle approximation. But unlike the Fermi equation, it takes into account occasional large deflections by individual electrons. The incorporation of the Molière scattering theory into the Fermi-Egyes theory has been

accomplished by Jette (1996). The Goudsmit-Saunderson theory has no restriction on the magnitude of the angular deflections. But, mathematically, it is fairly complex, and the particle distribution can only be evaluated numerically. The numerical solution takes a relatively long time to complete.

In addition, Luo (1985a) and Luo (1985b) have developed a bipartition model that divides the electron beam into two components. The first component describes the penetration of the small-angle scattered electrons, while the second describes the diffusion of large-angle scattered electrons. The model was later refined to include energy-loss straggling and secondary particle production (Luo and Brahme 1992). Recently, the bipartition model was embedded into the Fermi-Eyges multiple scattering theory to produce a more accurate hybrid electron pencil-beam model (Luo *et al.* 1998).

Another model that has shown promising results is the development of the phase space time evolution model. The model and its refinement are described in a series of papers (Huizenga and Storchi 1989, Morawska-Kaczynska and Huizenga 1992, Janssen *et al.* 1994, Korevaar *et al.* 1996, Janssen *et al.* 1997). This model takes into account every aspect of electron interactions and secondary particle production. Although the model is only developed for broad beams, its main advantages are its high accuracy and relatively fast computation time.

2.7 Monte Carlo simulation method

The most accurate method to date in determining electron or beta dose distribution is the Monte Carlo simulation method (Jette 1995 and references therein). The only

drawback of this method is the long computing time required to generate the distribution. The fundamental principle of the Monte Carlo method is to simulate every aspect of a particle's interaction by a computer generated random number governed by a probability function. The path of the particle is then determined by a set of probability functions sampled by a set of computer generated numbers. In beta and electron dosimetry, the probability functions are represented by the cross sections based on various theories as described earlier in this chapter. The quantities, such as the distance traveled by the particle, the direction of travel, and the energy deposited in the medium, are tallied or scored. The precision of the simulation depends on the number of source particles – the larger the number of the source particles, the better the statistics, and thus, the better the simulation. However, the time of simulation increases with the number of particles.

There are numerous Monte Carlo codes available. The most widely used codes for photons and electrons are EGS4 (Electron Gamma Shower 4) (Nelson *et al.* 1985, Nelson and Rogers 1988), ETRAN (Electron Transport) (Seltzer 1988), ITS (Integrated Tiger Series) (Halbleib 1988a) and MCNP (Monte Carlo N-Particle) (Briesmeister 1997). It should be pointed out that the MCNP follows the electron physics in ITS, and ITS is based on ETRAN (Jeraj *et al.* 1999). The Monte Carlo code used in this thesis is the ITS code. This code has been well "benchmarked" by comparison with various experimental data (Halbleib 1988b).

2.8 The radiochromic dosimeters.

One of the most important aspects in radiation dosimetry is the ability to measure dose accurately and precisely, and with high spatial resolution and sensitivity to a wide range of doses. Currently, there is not a single dosimeter that can perform dose measurements with all of these characteristics. Three commonly used dosimeters – ionization chambers, thermoluminescent dosimeters (TLDs), and radiographic films – all lack one or two of the above characteristics. An ionization chamber is an air filled chamber that measures ionization current generated by electrons ionized by incident radiation particles. The ionization current reflects the amount of deposited dose accurately and precisely. But the ionization chamber lacks spatial resolution because of the size of the chamber. A TLD is a solid state detector that measures dose by trapping electrons generated by ionizing radiation. The number of electrons is proportional to the intensity of the incident radiation. But the TLD also lacks the spatial resolution, although ultrathin TLDs of 0.05 mm thick, available commercially, can be stacked together to obtain higher resolution and sensitivity. Radiographic film records the dose deposited by capturing ionized electrons within the film at the trapping centers of its silver halide or silver bromide grains. The trapping process sensitizes the grains and changes the film colour, or its optical density, which is related to the dose deposited. Radiographic film has very high resolution, but it lacks the accuracy required because its response depends on the quality of post irradiation processing of the film. Furthermore, its photon energy response is not uniform, primarily due to a large change in the cross section of silver near the silver's K-edge.

Within the last decade, there has been a breakthrough development in the field of radiation measurements, in particular, radiochromic dosimeters. Radiochromism is a process that involves direct colouration of a medium after it has been irradiated, without any post irradiation processing. It has been in use since the 1800's. The historical background and the chemical makeup of radiochromic dosimeters have been reviewed by the AAPM Radiation Therapy Committee Task Group 55 (Niroomand-Rad *et al.* 1998 and references therein).

The latest radiochromic dosimeters, called Gafchromic Dosimetry Media (GDM), have been developed by the manufacturer International Specialty Products, Wayne, New Jersey. The makeup, characteristics, and response of the GDM have been reviewed thoroughly by Niroomand-Rad *et al.* (1998). The GDM is a thin radiochromic film that does not require post irradiation processing. It is relatively insensitive to the energy of incident photons or electrons and has a spatial resolution of 1200 lines/mm or better (Niroomand-Rad *et al.* 1998). There are several catalogue numbers of the GDM, such as HD-810 (formerly DM-1260), DM-100, and MD-55, for different range of dose measurements. Only the HD-810, DM-1260, and MD-55 are suitable for medical applications. The MD-55 type has several versions. The earlier version has only one radiosensitive layer and is generally referred to as the MD-55-1. The later version has two radiosensitive layers and thus, is more sensitive than the earlier one. It is generally referred to as the MD-55-2, or NMD-55 in some papers. The manufacturer has released various batches of the MD-55-2 films over the years, with each newer batch supposedly more spatially uniform than previous batches. The MD-55-2 films of lot # 941206 and

37175 are the batches used in the research for this thesis, with the latter a newer batch than the former. The MD-55-2 films have been extensively studied by McLaughlin *et al.* (1996), Meigooni *et al.* (1996), and Klassen *et al.* (1997). The suitable dose range for MD-55-2 was given by the manufacturer as 1 to 50 Gy (Fairman 1998). However, the AAPM Task Group 55 recommends a suitable range of 3 to 100 Gy (Niroomand-Rad *et al.* 1998). Klassen *et al.* (1997) claim that it is useable from less than 1 Gy up to 12 Gy at the maximum sensitivity at 676 nm, and up to 500 Gy at a wavelength of low sensitivity.

2.9 Factors that affects film response

The quantity most useful in characterizing the film response is the optical density, also known as the absorbance. Briefly, the optical density is the log of the ratio between the transmission without the film and with the film. A thorough definition of the optical density is given in Chapter 5. Often the term net optical density is used in the literature. The net optical density is usually referred to the transmission through an irradiated film with respect to the same film before irradiation or an unirradiated film.

The type of film of interest in this thesis is the MD-55-2. Since the film has only been available in the last few years, the majority of the research performed on radiochromic films has been on earlier versions of the GDM. However, in many cases, the results from those films can be applied to MD-55-2. In the following subsections, the factors that can potentially affect the film response are discussed. In general, to minimize

error due to external factors, the experimental films should be kept and used in the same conditions as the calibration films.

2.9.1 Dependence on temperature during irradiation

McLaughlin *et al.* (1996) have shown that there is little change in optical density read at 4 optical wavelengths for a MD-55-2 film irradiated with a gamma dose of 40 Gy between 10 to 30 °C during irradiation. However, for temperature above 40 °C during irradiation, the net optical density increases significantly. Their finding suggests that the film response is insensitive to minor changes in room temperature, in which irradiation experiments usually take place.

2.9.2 Stability with time and temperature post irradiation

Meigooni *et al.* (1996) have found that the net optical density (with respect to an unexposed film) at 632.8 nm increases by up to 15% approximately 4 hours after irradiation, and the net optical density appears to continue to increase by less than 3% per week after the initial 4 hours. Their findings are consistent with those reported by Klassen *et al.* (1997) and Reinstein and Gluckman (1999), who both show an increase of about 5 to 6% in optical density at 676 and 633 nm, respectively, at room temperature over the range of 2 to 12 h post irradiation with 14.52 and 30 Gy, respectively. Furthermore, Klassen *et al.* (1997) show that the rate of change in uncorrected optical density, defined as the optical density of the film after irradiation minus the optical density of the same film before irradiation, decreases over time. This decrease rate is

larger for higher dose. But after 120 days, the rate of change of optical density is equivalent to about 0.5 cGy/d independent of the dose from 0 to 14.52 Gy. In addition, Reinstein and Gluckman (1999) found that the rate of change in net optical density is dependent on the storage temperature post irradiation. At 45 °C, the optical density seems to have reached an asymptotic value after 8 h. But at lower temperature, the time to reach the asymptotic value is considerably longer. Moreover, the asymptotic value of the optical density is slightly dependent on the storage temperature, about a 4% increase from the temperature of 20 to 35 °C at about 30 Gy.

These findings lead to the recommendation of film readout at least a 24 hour (preferably 48 hour) period after irradiation (McLaughlin *et al.* 1991, Klassen *et al.* 1997, Niroomand-Rad *et al.* 1998). In addition, to minimize the error due to the different rate of change in optical density with time, the irradiated film should be scanned with an unirradiated film from the same lot, and the unirradiated film should be kept in the same storage temperature as the irradiated film. The storage temperature of the films and the time between irradiation and readout should also be close to those of the calibration films.

2.9.3 Dependence of temperature during readout

The effect of temperature on the optical density during readout has been studied by Klassen *et al.* (1997) and Reinstein and Gluckman (1999). They both found that as the temperature increases, the two absorption peaks on the optical density spectrum (see, e.g., Figures 6.1a – 6.1c) shift to shorter wavelengths, and the absorption peak amplitude decreases. At several wavelengths, the combination of the shift and the decrease in

amplitude effectively counteract each other, resulting in a minimal change of optical density. Fortunately, the temperature effect on the optical density during readout is reversible. Their findings suggest that the temperature of the irradiated films should be the same as the calibration films during their respective readouts. If the temperature cannot be controlled, the readout wavelength should be carefully chosen to minimize the temperature effect.

2.9.4 Film uniformity

The nonuniformity of a film can be described by local and regional fluctuations (Niroomand-Rad *et al.* 1998). Local fluctuations of the film response arise from variables such as the film grain size, spatial and signal resolution of the film scanner, pixel size and depth, and electronic noise. Regional fluctuations of the film response are produced by, for example, a systematic problem in laying the film emulsion layers or a drift in the scanner response. Meigooni *et al.* (1996) reported a regional nonuniformity, defined as the ratio of the maximum-minimum responses, of an early batch (unknown lot number) of the MD-55-2 films to be about 4% in the longitudinal direction, which turns out to be parallel to the direction of the coating application (Niroomand-Rad *et al.* 1998), and about 15% in the transverse direction. Zhu *et al.* (1997) also found regional variations of 8 – 15% in a batch of MD-55-1 films. These investigators concluded that the nonuniformity is likely due to the nonuniform distribution of the radiosensitive material in the film. However, Butson and Yu (1998) reported a regional nonuniformity of less than 1% in one direction, and 2.5% in the other direction for the MD-55-2 film with an

early batch of lot # 941206. Reinstein *et al.* (1997) also found the sample-to-sample net optical density variation, and within sample net optical density variation, for a batch of MD-55-2 (lot # 941206) film to be 2.8% and 3.6%, respectively, at the 95% confidence level. The net optical density there is defined by subtracting the optical density prior to irradiation from the optical density post irradiation. The manufacturer has committed to improving the film uniformity in subsequent batches.

Zhu *et al.* (1997) have proposed a double-exposure method to improve the film uniformity. The method involves first irradiating a film with a uniform known dose. The film is read before and after the irradiation to establish a matrix of uniformity correction factors on the film. Then the film is irradiated with an unknown dose. The resulting nonuniformity corrected optical density is derived by the difference in the optical density between the first and second irradiations divided by the correction factor at each point on the film. The authors claim that their method has reduced the regional variations of 8 – 15% to only 2 – 5% random fluctuations.

2.9.5 Energy dependence

The energy dependence of radiochromic films has been studied by numerous researchers, but much research has focussed on the MD-55-1 films or earlier versions (McLaughlin *et al.* 1991, Muench *et al.* 1991, Soares and McLaughlin 1993, Chiu-Tsao *et al.* 1994, McLaughlin *et al.* 1994). Meigooni *et al.* (1996) have compared the response characteristics of both MD-55-1 and MD-55-2 films and found that the energy dependence of each film irradiated with 6, 18 MV photons, and ^{60}Co gamma rays is

minor (within 5%) in the dose (to water) range of 1 – 50 Gy. Furthermore, McLaughlin *et al.* (1996) showed that the photon energy response of a batch of MD-55-2 film at 20 to 40 keV is roughly 40% lower than that at about 1 MeV. This finding is consistent with that of Chiu-Tsao *et al.* (1994) who found a 44% reduction in sensitivity from ^{60}Co to ^{125}I irradiation to a batch of MD-55-1 films. This reduction in sensitivity has been explained by Prestwich and Murphy (1999) using the cavity theory and the low energy dependence of the stopping power ratio.

The above findings seem to indicate that the relative photon energy response of MD-55-1 and MD-55-2 films are similar for 20 keV or higher, and the research done in photon energy response for the MD-55-1 films can be applied to the MD-55-2 films. This assumption is reasonable since the radiosensitive layers of both types of films are identical. However, the energy response of the MD-55-1 films to electrons should be different from that of the MD-55-2 films at low energy because of the electron attenuation of the extra film substrate surrounding the radiosensitive layers in the MD-55-2 case. At high electron energy, McLaughlin *et al.* (1991) have found that the response due to 10 MeV electron beam and ^{60}Co gamma irradiation agreed to within 5% at 95% confidence level for a batch of MD-55-1 film. This result is applicable to the MD-55-2 films since the dose attenuation in the film substrate is minimal at this energy. However, at energy of 1 MeV or lower, the energy loss in the substrate becomes significant, and corrections must be made.

2.9.6 Effects of ambient light and readout light source

The ambient light required for the handling of the radiochromic films and the readout light source should be chosen so as to minimize their effects on the films. The manufacturer does not provide the sensitivity of the film as a function of wavelength. But they claimed that the sensitivity of the MD-55 films increases monotonically with decreasing wavelength down to about 310 – 320 nm (Fairman 1998). Butson *et al.* (1998) have investigated the effects of ambient light and readout light sources on the MD-55-2 films (lot # 941206). All light sources that were investigated contributed an increase in optical density to the films, with sunlight and fluorescent light being the biggest contributors because of their high UV components. They also found that after 175 h of "exposure", a 1 mW He-Ne laser (632.8 nm) placed 3 mm from the film contributed an equivalent dose rate of about 43 mGy/h. A 60 W incandescent light source placed 15 cm from the film gave an equivalent dose rate of approximately 29 mGy/h. An ultrabright LED with peak wavelength at 660 nm, placed 3 mm from the film, contributed an equivalent dose rate of about 17 mGy/h. Their findings illustrate that the wavelength(s) used for scanning should be as long as reasonable, and the time of scanning or "exposure" at any point on the film should be minimized.

2.9.7 Effects of polarized light during readout

Klassen *et al.* (1997) have extensively investigated the effects of polarized light on the film response. They found that the response of polarized light on the film varies depending on the film orientation. This variation was attributed as mostly due to the

polarization of the middle mylar layer of the film, which displays the characteristics of a ½ wave plate. Since most scanning light sources are linearly or partially polarized, it is important to keep the orientation of the films before and after irradiation, as well as the reference films, consistent.

2.9.8 Other external factors

Other external factors that can potentially alter the film response include humidity, dose fractionation, and dose rate. The effect of humidity on the MD-55-2 films is not known, though McLaughlin *et al.* (1996) have claimed, without proof, that the optical density of the MD-55-2 films is independent of relative humidity during irradiation. However, the effect on earlier versions of the GDM (HD-810 (DM-1260)) during irradiation and storage has been reported to be about ± 2% over a relative humidity range of 0 to 94% (Saylor *et al.* 1988, Janovsky and Mehta 1994). However, the humidity effect during readout at 400 nm was found to decrease optical density by about 15%, while increasing relative humidity from 35 to 100% (Chu *et al.* 1990).

The effect of dose fractionation is also not available for the MD-55-2 films. But the effect between unfractionated and fractionated values has been reported to be minimal (± 1%) on the HD-810 films (Chu *et al.* 1990). The effect on optical density for the MD-55-2 films by ^{60}Co gamma irradiation at 670, 633, and 600 nm has been claimed, without proof, to be independent of dose rate (McLaughlin *et al.* 1996). This claim is consistent with a study, which was unfortunately misreferenced (Niroomand-Rad *et al.* 1998), on an

earlier version of the GDM where response by ^{60}Co irradiation at about 670 and 610 nm was observed to be identical at various dose rates.

2.10 Dose measurement using radiochromic film

Currently, the most common method of measuring dose using radiochromic films is to choose a single wavelength strategically, depending on the desired dose range and external factors such as minimizing the temperature effects (see Section 2.9.3). Then an optical density-to-dose calibration at this wavelength can be established by scanning a set of films with known doses by usually a densitometer system. An unknown dose in a film can then be determined from the calibration. This method will be further described in Chapter 5. Other methods generally revolve around this single-wavelength calibration method.

One method that has gained much attention is Zhu *et al.*'s (1997) double-exposure method (see Section 2.9.4). However, this method is only used to reduce the nonuniformity of the films, not to calibrate them. Klassen *et al.* (1997) adopted this double-exposure method and extended it to include calibration. They found that at λ = 676 nm, the optical density varies with dose linearly at two portions, from 0 to 6 Gy, and 6 to 15 Gy. They irradiated a set of films with "unknown" doses of 5 to 7 Gy, followed by a known dose of 6 Gy 7 days later. The change in optical density, defined as the optical density due to the exposure plus the optical density that would have taken place in the absence of the irradiation, was measured for the first (ΔOD_1) and second (ΔOD_2) exposures two days after respective irradiation. A control group of films used in

determining the change in film sensitivity between exposures was irradiated with a known dose of 6 Gy, and another 6 Gy after 7 days. The change in optical density was measured for both exposures two days following irradiation. The "unknown" dose, d_u was then determined by,

$$d_u = \frac{\Delta OD_1 / \Delta OD_2}{(\Delta OD_1 / \Delta OD_2)_c} \times 6\,\text{Gy}, \tag{2.28}$$

where the subscript, c, denotes the control group. It was found that the calculated values using this method had uncertainties of less than 1% and agreed with their expected values. However, this method has its limitations because it has only been tested for a very small range of doses (5-7 Gy), a long period of time is required between the two exposures, and considerable more time and effort are needed to obtain the results.

The double-exposure method proposed by Klassen *et al.* (1997) deals with the nonlinear characteristics of the dose response curve. However, if a linear dose response relation at a wavelength can be found, a self-calibration method to determine an unknown dose can be utilized. The idea of self-calibration follows that to determine an unknown dose deposited in a film, additional exposure(s) is given to the film. The response of the additional dose(s) can be extrapolated to calculate the unknown dose. To date, this method does not appear to have been used for radiochromic film because of the non-linearity of the dose response.

Reinstein *et al.* (1997) devised a method of predicting the optical densitometer response for various light source characteristics. Their method includes various factors such as the assumption on the light source characteristics and filter, if any, on the light

source. However, this method can be modified to obtain experimentally a net optical density-to-dose response curve. For a polychromatic light source, the optical density-to-dose calibration curve can be simplified from the general dose response curve to,

$$OD(d) = -\log\left(\frac{\int_0^{\infty} I(\lambda, d)d\lambda}{\int_0^{\infty} I_{\bullet}(\lambda)d\lambda}\right), \tag{2.29}$$

or,

$$OD(d) = -\log\left(\frac{\sum_i I(\lambda_i, d)}{\sum_i I_{\bullet}(\lambda_i)}\right), \tag{2.30}$$

where I is the transmitted intensity through the film, and $I_{\bullet}$ is the intensity of the light source. The net optical density-to-dose curve is then obtained by subtracting the $OD(d = 0)$ curve prior to irradiation. This modified method should increase the sensitivity of the film because of the multiple wavelengths used. However, the method breaks down at very high dose because of saturation at various wavelengths, resulting in the saturation of the calibration curve.

Another method, which is not widely used but shows promising results, is to scan the radiochromic films using a document scanner (Stevens *et al.* 1996). The authors scanned unirradiated and irradiated films by a commercially available off-the-shelf document scanner, typically used for scanning images into computers. A black-and-white imaging mode employing 256 gray-scale elements was used to digitize the scanned image. The resolution of the image depends on the resolution available for the scanner,

typically greater than 10 dots/mm. The gray-scale element of each pixel is converted to net optical density relative to the scanner signal for an unexposed film. This conversion allows the net optical density-to-dose calibration curve to be determined, with a minimum detectable dose of 0.7 Gy. It was reported that for that particular scanner, the standard deviation of the individual scanner signal matrix elements about the mean value due to the digital noise was about 2, and the mean scanner signal for a particular film can vary by up to 2%. The document scanner offers affordable, quick, and high resolution scanning. But it suffers from minor problems in stability, nonuniformity of light, and increase of exposure to film due to the scanning light source.

CHAPTER 3

INSTRUMENTATION

The equipment used for dose measurement will be referred to as the McMaster dose imaging system (MDIS). The imaging system is composed of a microspectrophotometer (MSP) and a dosimetric medium, the radiochromic film. As the name suggests, the MSP consists of three major components – a microscope, a monochromator, and a photomultiplier. In addition, there is a tungsten-halogen light source, an X-Y stage where the radiochromic film is placed, and a computer to which the imaging system is interfaced. Figure 3.1 shows a diagram of the MDIS, and each component will be described in the following sections.

3.1 The microspectrophotometer

The MSP was built by Sciencetech Inc. to measure the light intensity transmitted through a dosimetric medium. In fact, part of the research in this thesis was dedicated to commissioning this instrument.

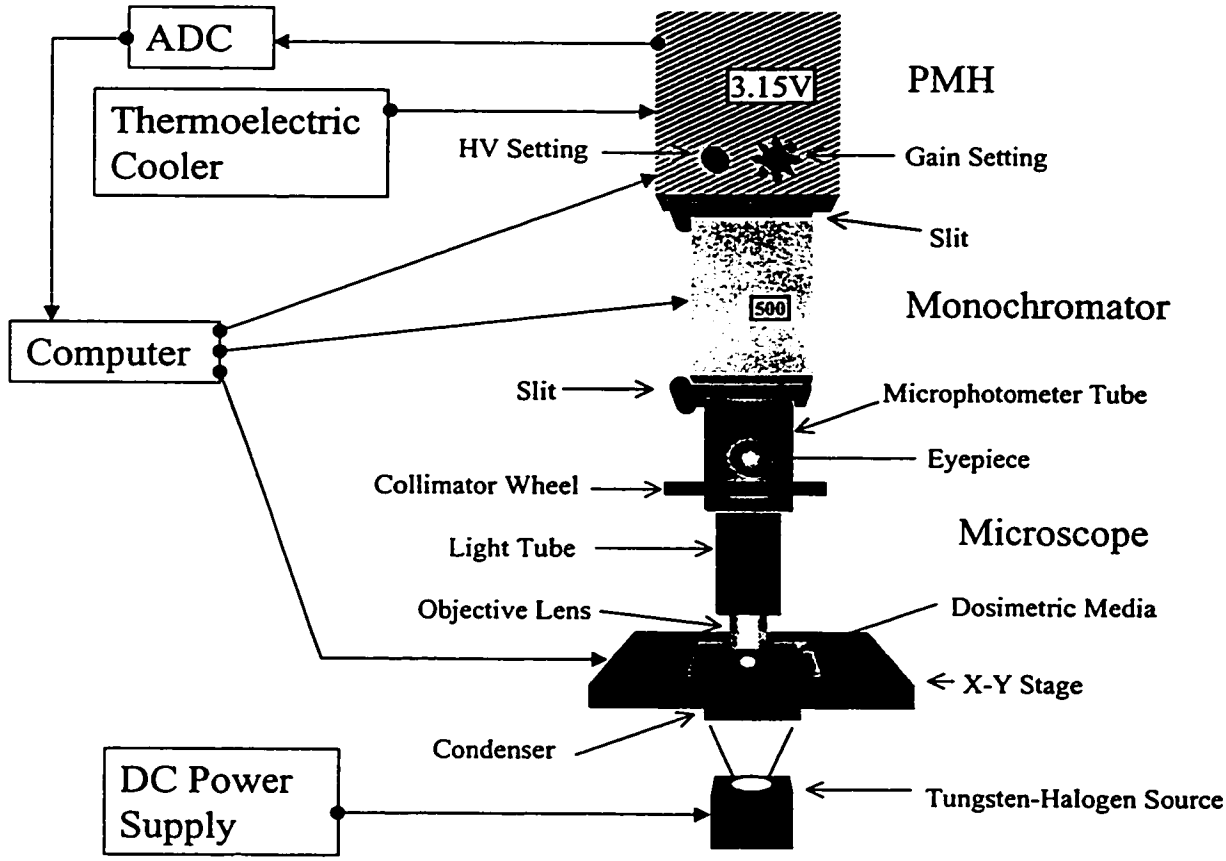

Figure 3.1 Diagram of the McMaster Dose Imaging System

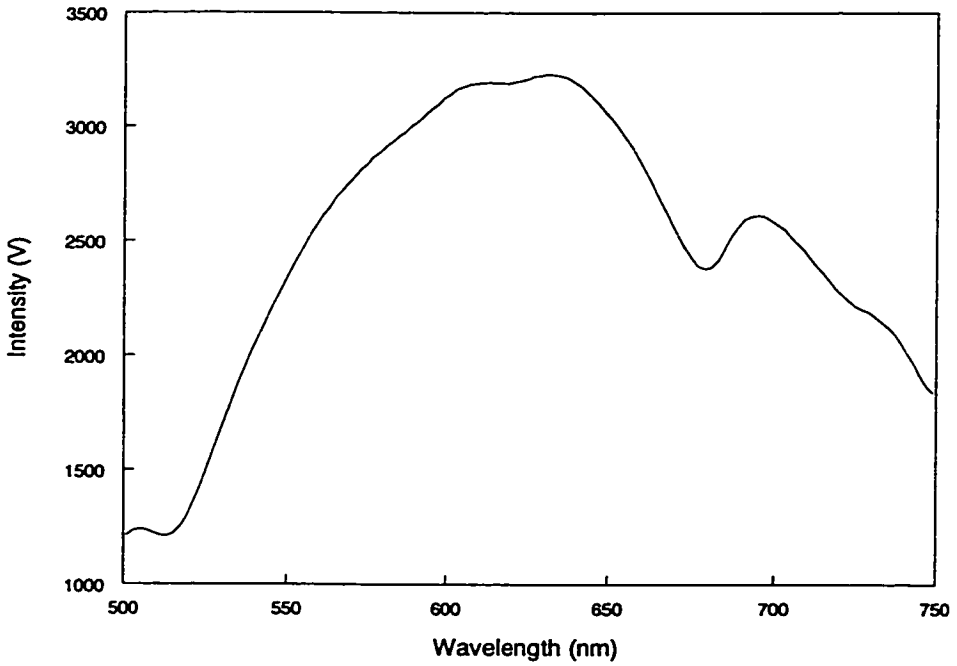

Figure 3.2 Spectral response of tungsten-halogen lamp

3.1.1 The tungsten-halogen lamp

The tungsten-halogen lamp is the light source that provides "white" light to the MDIS. Figure 3.2 displays the spectrum of the lamp. The spectrum resembles a blackbody spectrum at about 4600 K with the peak wavelength at about 630 nm. The presence of the halogen gas and other chemicals keeps the tungsten filament from evaporating when heated. Thus, the filament is allowed to be heated to a much higher temperature, resulting in a whiter emission. However, their presence is also likely to have altered the blackbody spectral shape slightly. This spectrum is suitable for reading the radiochromic film because the GDM used has major and minor peaks at between 620 and 670 nm in the absorption spectrum.

The lamp is located at the base and in the back of the microscope, and the light is pointed horizontally toward the front of the MSP. The light goes through a convex lens before being reflected by a flat mirror into a condenser, attached just below the X-Y stage. The aperture of the light on the X-Y stage can be controlled by the iris diaphragm located at the base of the condenser. The smallest aperture size, approximately 1 mm, is usually chosen so as to reduce the amount of light scattered into the photomultiplier tube.

A Kodak Wratten gelatin filter (catalog no. 149 5498) was also mounted semi-permanently just beneath a flat lens situated below the condenser. The filter is in place to cut off the transmitted light with wavelength shorter than 500 nm so as to eliminate the UV dose to the radiochromic film during readout.

The power to the lamp is provided by a DC power generator, and its operating voltage and current are chosen to be about 5 V and 2 A, respectively. This power setting is selected to provide a strong enough signal so that stray light from other sources would not contribute significantly to the signal. The lamp has to be powered on for at least 30 minutes to allow the temperature of the filament to reach equilibrium, i.e. to become stable, before any measurements can be performed.

3.1.2 The X-Y stage

The X-Y stage was built onto the existing stage of the microscope and is located between the condenser and the objective lens. The stage is where the dosimetric medium, i.e. the radiochromic film, is placed. Special film holders were designed to hold the film tightly in place and were required to be rigid. The height of the stage must be adjusted

manually by turning the coarse adjustment control (knob), located at the bottom of the microscope, to provide the desired sensitivity and resolution to the photomultiplier. Then the stage must be leveled by adjusting the height of the post that supports the right side of the stage, where the stepping motors are located. Once the stage appears to be leveled, fine adjustments are still required. The focus must be adjusted by turning the fine adjustment control, located right behind the coarse adjustment control, for the height adjustment. In addition, the light alignment must also be adjusted by the two alignment screws, located underneath the stage, such that the peak of the light source appears in the center of the field of view as seen in the eyepiece. The two screws control the apparent vertical and horizontal position of the light source. If maximum sensitivity is desired, then the coarse and fine adjustment controls and the screws must be adjusted simultaneously until a maximum response is detected in the photomultiplier.

Two stepping motors are attached to the stage to provide movement in the x (horizontal) and y (vertical) directions. The range of the movement is 2.479" (63.0 mm) in the x direction and 2.43" (61.8 mm) in the y direction, and the minimum step size is 0.00025" (6.35 μm). The speed of the movement of the stage was measured to be approximately 3.15 mm/s. Furthermore, every time the stepping motor stops, a delay of a fraction of a second is added to allow the system to stabilize before any light intensity measurement is made.

It was discovered after all the experiments were finished that the weight of the two stepping motors could cause a small tilt to the stage if the stage was moved near the end of the range. This small tilt can result in a small change in the light intensity because

the condenser is attached to the base of the stage. The maximum change observed in the light response was approximately 1% when the stage was moved from one end to the other, in both x and y directions. Since in most cases, the scanning was performed away from the end of the range, and this change is not very significant, no correction to the data was considered necessary.

3.1.3 The microscope

The microscope is a Leitz microscope photometry system that has been modified to have other components of the MSP built around it. Its main function is to allow for spot measurements of microscopic size. Once the light passes through a dosimetric medium on the X-Y stage, it enters the objective lens located at the base of the light tube. There are 6 objective lenses available with 6, 10, 25, 40, and 100 times magnification. The light tube is 170 mm long and is attached to the flange of the microphotometer tube, which contains a pinhole collimator wheel and two plano-convex lenses. The wheel has 8 pinhole settings, and their diameters are 0.01, 0.03, 0.1, 0.3, 1.0 mm, plus two open holes with diameters of 5 mm, and one plugged for background measurements. The two lenses have short focal lengths and are located in the rear of the microphotometer tube. Their purpose is to focus the pinhole image onto the input slit of the monochromator.

The microphotometer tube was added onto the original microscope. Unfortunately, the exact placement of the plano-convex lenses and their properties are not known. Based on the description from the operating manual of the MSP and some measurements performed, certain properties involving various components of the MSP

were inferred. Table 3.1 lists the light signal measured at various pinhole diameters and slit sizes, at a wavelength of 662 nm and a high voltage of 561 V, using the objective lens with a magnification of 10×. It should be noted that the last row of the Table is the background measurement, and all the other measurements have been background corrected. Moreover, the signals at the pinhole diameter of 5 mm in columns 3 and 4 were saturated at the value of 10.60 V. The measurements using the pinholes with diameters of 0.01 and 0.03 mm were not performed because the light intensities are extremely small.

Pinhole Diameter (mm)	Gain Setting (×)	Signal (V) (no slit)	Signal (V) (slit size = 1 mm)	Signal (V) (slit size = 0.5 mm)	Signal (V) (slit size = 0.25 mm)
5	1	> 10.60	> 10.60	10.00 ± 0.01	5.10 ± 0.01
1	10	7.58 ± 0.01	7.54 ± 0.01	7.29 ± 0.01	5.25 ± 0.01
0.3	100	7.33 ± 0.01	7.28 ± 0.01	7.13 ± 0.01	6.25 ± 0.01
0.1	1000	3.53 ± 0.05	3.43 ± 0.05	3.21 ± 0.05	2.79 ± 0.05
0 (Bkgd)	1000	-0.85 ± 0.01	-0.84 ± 0.01	-0.85 ± 0.01	-0.84 ± 0.01

Table 3.1 Light signal measurements at various pinhole diameters and slit sizes

The Table shows that as the pinhole diameter or the slit size decreases, the light intensity signal also decreases. In column 3, the signal was measured without an input slit to the monochromator. The intensities at every pinhole, except the 5 mm one, are slightly larger than the respective signals measured with the slit size of 1 (column 4) and 0.5 mm (column 5). The small difference seems to suggest that the effective input slit is controlled by the pinhole collimator, rather than the input slit size, in every case except the one with the largest pinhole diameter. The reason that there is a small drop in

intensity as the slit size decreases may be due to the reduction of stray light created by lens aberration. In the case of the 0.25 mm slit size (column 6), the signals measured with the pinhole of 5 mm diameter, and possibly of 1 mm as well, appear to be controlled by both the pinhole collimator and the slit.

Assuming that all the light transmitted through the pinhole collimator will eventually enter into the photomultiplier, and the source has a flat light intensity profile, then the ratio of the intensities should be directly proportional to the ratio of the areas of the pinhole collimators, thus proportional to the square of the ratio of the pinhole diameters. This relationship appears to be valid for the 1 and 0.3 mm pinholes in the cases of no input slit and slits with widths of 1 and 0.5 mm. The ratio of intensities is about 10, while the ratio of pinhole areas is about 11. This agreement is consistent with the above suggestion that these two pinholes are essentially the effective input slits for the monochromator. However, for the 0.25 mm slit, the ratio of intensities is only 8.4, which may indicate that the effective input slit is not due to the pinhole alone in the case of the 1 mm pinhole, or the center of the slit does not match perfectly with the center of the pinhole. In addition, this agreement does not extend to the 0.1 mm pinhole for all the slit sizes because the ratio of the intensities with the 0.3 mm pinhole is about 20, while the ratio of pinhole areas is only 9. It is still not certain what causes this discrepancy, and it is speculated that perhaps a fair amount of stray light created by lens aberration is lost in the microphotometer tube. The loss of the stray light should also occur in the measurements using larger pinholes. But this loss would not be very noticeable because of their larger signals.

The selection of the magnification and the pinhole size depends on the desired resolution of the scanning. If the transmitted light through the film is focussed onto the pinhole collimator, then the effective aperture is roughly determined by,

$$\text{Effective Aperture} = \frac{\text{Pinhole Size}}{\text{Magnification}}. \tag{3.1}$$

The above equation is only valid for the pinholes that also act as the effective input slit. If high resolution is not a concern, then the magnification should be at the minimum (6×), and the pinhole collimator should be set to open (5 mm) to increase the sensitivity. This setting would give an effective aperture greater than 0.83 mm.

3.1.4 The monochromator

The monochromator is a Sciencetech 9030 model and is located between the microphotometer tube and the photomultiplier. It contains a diffraction grating that diffracts the incoming "white" light into exiting monochromatic light. The diffraction grating has a resolution of better than 1 nm with a grating of 1200 lines/mm and has a spectral range of 0 – 1000 nm, with a reproducibility of 0.25 nm. It also has a line dispersion of 8 nm/mm. Since slits of 0.25 mm were placed on the ends of the monochromator, the bandpass can be determined roughly by multiplying the line dispersion by the convolution of the two slit widths, giving a value of about 3 nm. This calculation is only applicable in the case where the calculated bandpass is significantly larger than resolution.

The monochromator was calibrated using a mercury arc lamp. The mercury arc lamp has many sharp lines at discrete wavelengths, and this feature is demonstrated in Figure 3.3. The graph displays a log plot of the spectral curve of the mercury lines after the monochromator had been calibrated.

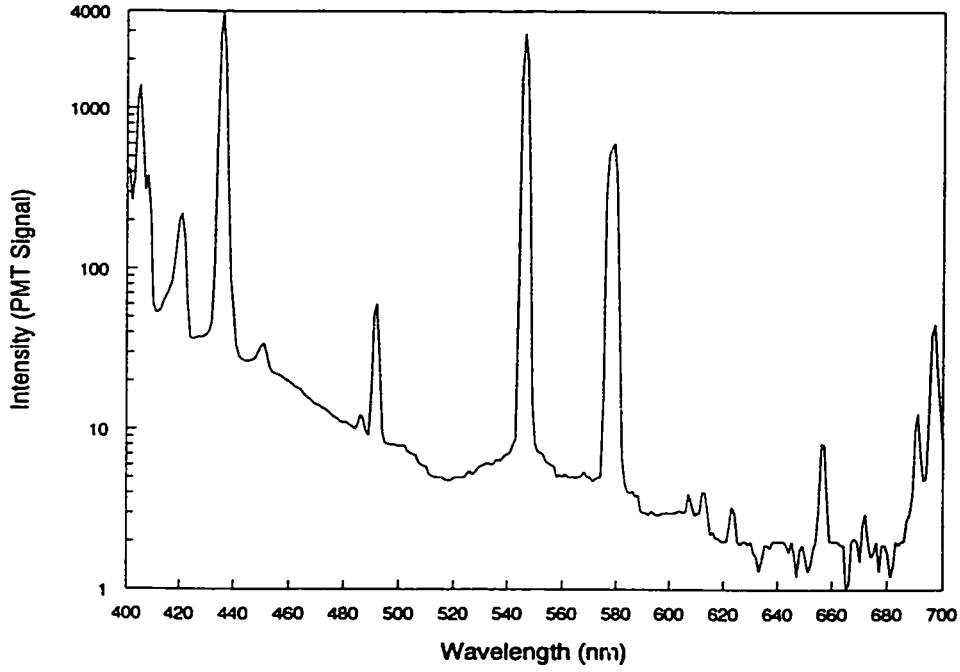

Figure 3.3 Calibration using mercury arc lamp

3.1.5 The photomultiplier system (PMS)

The photomultiplier is located just above the monochromator separated by a slit. The PMS includes a Hamamatsu photomultiplier tube (PMT), a Sciencetech PMH-04 Peltier cooled photomultiplier housing (PMH), a Sciencetech PMH-04c thermoelectric cooler controller, and a high voltage (HV) supply.

The PMT is a 1⅛" side window tube that came with the PMS. The PMH is a self-contained compact unit for the PMT operation in analog mode. The PMH must be cooled during operation to allow the signal from the PMT to stabilize by maintaining a constant temperature inside the housing, and to reduce the thermionic noise in the signal. The thermionic noise is a result of the noise in the resistors and the noise due to the excitation of electrons in the photocathode or the dynodes in the PMT. The resistor noise is very small compared to the noise due to the excited electrons. In the latter, the probability of such excitation can be estimated by the Boltzmann equation governing the probability of the population of particles in different energy states, i.e.,

$$P \propto e^{-\frac{\Delta E}{kT}}, \tag{3.2}$$

where ΔE is the energy required to excite the electrons from either the photocathode or the dynodes.

Figure 3.4 illustrates the log of noise level at various inverse temperatures of the PMH. The curve appears to have two distinct portions: a linear portion at high $1/T$ (> 0.0037 K^{-1}), and an almost linear portion at low $1/T$. This seems to show that there are many different energy barriers in the PMT, and a higher temperature is required to excite the electrons to overcome higher energy barriers. Furthermore, the work function of the photocathode is greater than 3 or 4 eV for most metals and as low as 1.5 to 2 eV for suitably prepared semiconductors, and photocathodes are generally designed to convert as many incident light photons as possible into low-energy electrons (Knoll 1989). Therefore, the energy barrier, ΔE, of the photocathode may be distinct from that of the

dynode, which must be larger than its bandgap energy, typically of the order of 2 to 3 eV. The linear portion with a flatter slope, i.e. an indication of a smaller ΔE, thus longer maximum wavelength, may be the result of photoelectrons escaping from the photocathode, while the almost linear portion with the steeper slope may be the contribution from photoelectrons leaving the photocathode and the dynodes.

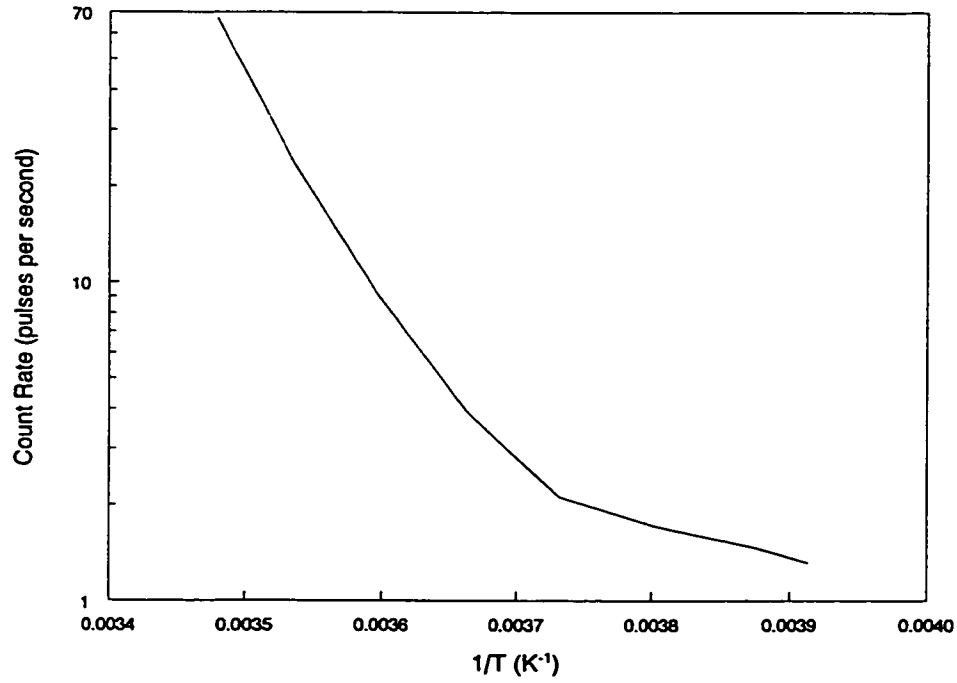

Figure 3.4 Count rate of PMT noise as a function of $1/T$

The PMH is cooled by the thermoelectric cooler controller, which monitors the temperature by a sensor mounted on the PMT carrier, and the heat is removed by running tap water through the PMH unit. The temperature can be set to a minimum of close to -20 °C. Normally, the operating temperature is set to 0 °C since the noise level is relatively small, about 4 counts per second at that temperature, and the resulting dark

signal will be subtracted from the PMT signal. At this temperature, the time it takes for the PMH to cool from room temperature to become stable is approximately 30 minutes. The water must be kept running to prevent a thermal runaway when the temperature controller is operating. A fail-safe device was installed to halt the thermal runaway by automatically shutting down the controller if it detects a temperature reading higher than 30 °C for a sustained amount of time.

The HV supply provides high voltage across the PMT. It can be adjusted to supply a voltage from 0 to 1200 volts. A higher voltage would give a stronger signal. The electronic signal can also be amplified by changing the electronic gain of the circuitry. Four gain settings are available, and they are at 1, 10, 100, and 1000 times. In general, a higher gain is selected at lower transmitted light. The signal is processed by a low pass filter. A time constant, τ, of 0.01, 0.1, 1, 10, 100, and 1000 ms can be selected. The signal response follows $1 - e^{-t/\tau}$ so that typically the time, t, it takes for the response to settle is about 4τ. The band pass of the low pass filter is $1/2\pi\tau$, and the root mean square of the noise is proportional to the square root of the band pass. Therefore, a small time constant will produce a noisy output, but a large time constant will take a longer time to produce a stable signal. For a good compromise between the signal-to-noise ratio and the response speed, a setting of $\tau = 1$ ms was selected for most of the measurements. The signal output is in volts and represents the intensity of light measured by the PMT.

3.1.6 The computer and analog-to-digital converter

The MSP is controlled by a Pentium® 100 MHz computer running on Microsoft Windows 3.1. The analog output from the PMT is sent to a 12-bit dual-slope analog-to-digital converter (ADC), chosen for its high stability, interfaced with the computer. A Visual Basic program, originally written by Kenrick Chin, allows users to select the spectral range, the wavelength step size, the x, y range and step size, the number of points required to be averaged for each measurement, and the correction of the dark signal. At the end of every set of measurements, the program will generate an output file listing the intensity signal and its variance measured by the PMT at pre-selected x, y coordinates and wavelengths. However, both the input and the output parameters can be tailored by modifying the program.

The ADC is a 12-bit device. The maximum value was arbitrarily designed to be 4.096 V, with a maximum resolution of 0.001 V. Therefore, the HV, gain setting, collimator aperture, and magnification must all be chosen carefully to avoid signal saturation beyond the maximum acceptable signal. In addition, for reasons yet to be known, the Visual Basic program tends to stop responding if it runs continuously for a period of time longer than about 12 hours, or if the output data file is greater than approximately 1.2 megabytes. It is speculated that the halting is due to a flaw in the operating system of the computer.

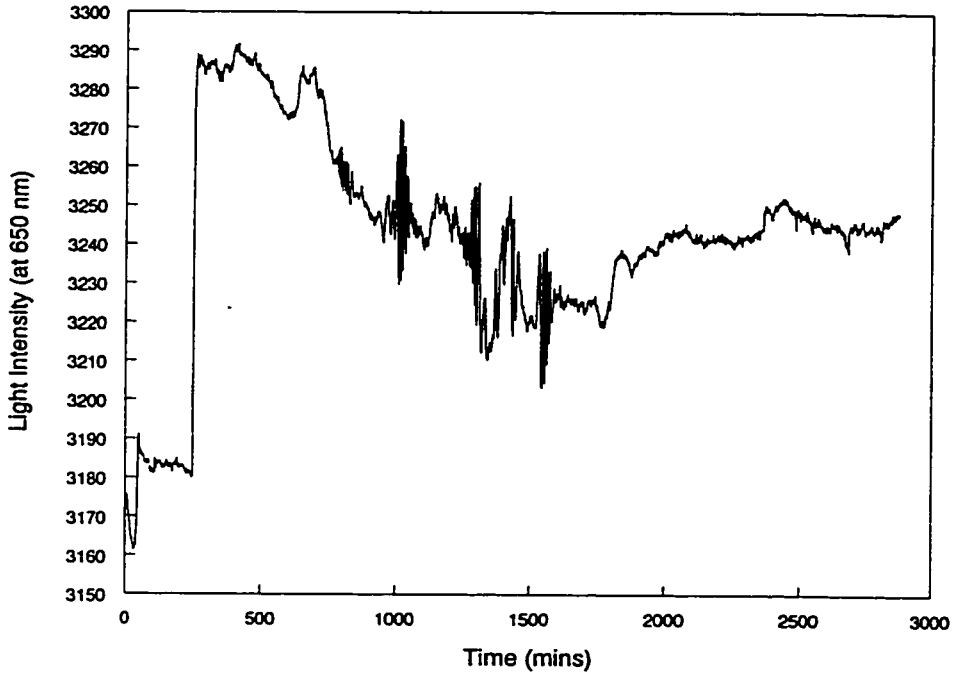

Figure 3.5 Stability of MSP light signal

3.2 Stability of the MSP

The stability of the MSP depends on the stability of its components, namely the DC power supply and the tungsten-halogen lamp, the PMT and the thermoelectric cooler controller, the HV supply, the electronic gain, and the ADC. The stability of the MSP is crucial since a change in light intensity may be interpreted as the wrong dose deposited into the dosimetric medium. Figure 3.5 displays a typical graph of the stability of light intensity of the MSP over a period of 2 days. The intensity began with a steady drop of about 0.5% over the first 30 minutes before rebounding up about 1% in 10 minutes. Then it began to drop slowly for another 200 minutes before it increased sharply again over 3% in fewer than 3 minutes. The intensity continued to drop gradually over the period of one

day before it climbed back slowly, with local random and periodic intensity variation of as much as 2% within as small as a 10 minute period.

To examine where the instability of the MSP came from, each component of the MSP was isolated and tested. First, the DC power supply was replaced and then the ADC. But similar instability patterns were observed in the light output. Then the original and the new ADC's were compared directly, and as expected, almost identical patterns were observed. These measurements do not necessarily exclude the components mentioned above from causing the instability since the replaced components could potentially be the cause as well.

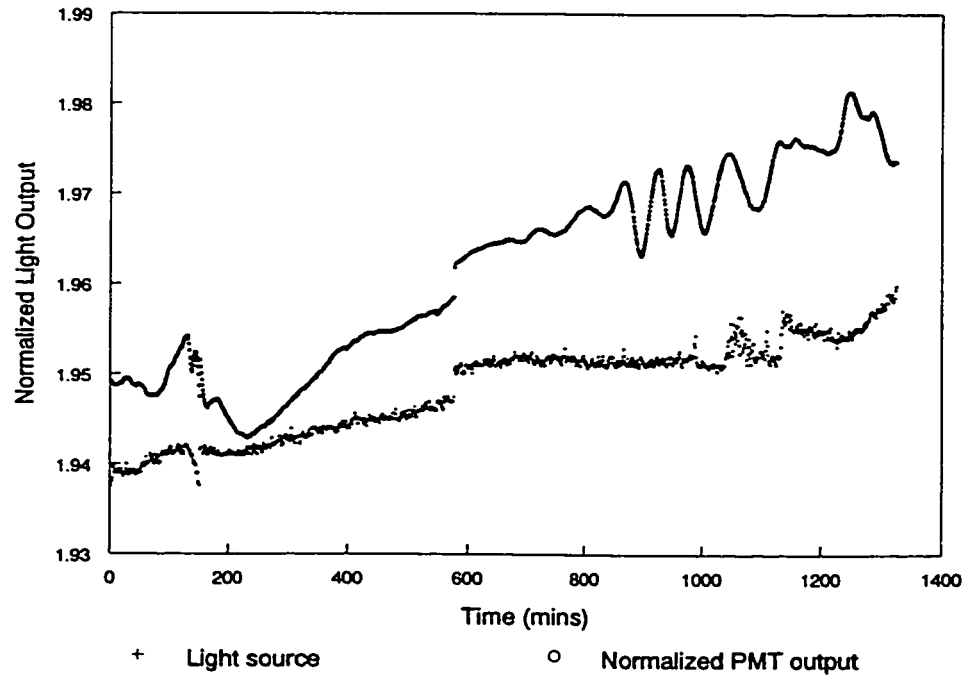

Figure 3.6 Comparison between direct light source and normalized PMT output

Next, the light source was turned off, and the dark signal in the PMT was recorded at a fixed HV and electronic gain. The result showed a random pattern in the background intensity as would be expected, though a long term slow varying drift was also observed. Finally, a photodiode was placed near the light source. The photodiode output, which measured the light intensity directly, was compared to the ADC output, which measured the light intensity through the PMT. The measurements are illustrated in Figure 3.6. The graph shows that the main features of the light source output (the lower curve) – i.e. the drop in intensity at about time = 150 min, the sharp jump near 600 min, and the oscillations beginning at about 1000 min – can also be seen in the normalized PMT output (the upper curve). But the PMT output also has a number of features not seen in the light source output. This leads to the speculation that more than one component is responsible for the instability of the instrument.

It was once suspected that the temperature on the PMH might be the source that caused the long term fluctuations in the light intensity. Therefore, a thermistor was attached to the outer PMH to measure the change in temperature on the PMH. But the thermistor output did not correlate with the photodiode or the ADC output. For the short term fluctuations, mechanical vibrations of the equipment was ruled out as the cause since no noticeable change in light intensity was observed after manually shaking every component of the MSP.

It is still not clear from where all the instabilities originate. It is speculated that the AC power source in the building could also be a source of the instability. Since replacing certain components of the MSP did not make a significant difference, the

instability of the MSP has dictated the way light intensity measurements were made. In Figure 3.5, the worst case of instability is the 3% sharp increase of intensity in fewer than 3 minutes. However, the worst case ever observed in the same period is over 5%. Fortunately this sharp increase occurrence is fairly infrequent. It may not happen at all in a week, but occasionally, it can also happen more than once in a day. Although this occurrence cannot be avoided, a repeat of any measurement would almost definitely remove this problem. A more problematic phenomenon is the local random and periodic intensity oscillations in a short period. These oscillations occur quite frequently. In the worst case scenario, the intensity can increase or decrease by close to 3% in a 10 minute period. Based on this revelation, all measurements were made within 3 minutes before or after scanning a reference film so that the error in the light transmission through a film due to this instability was kept below 1%.

3.3 Reproducibility of spatial scans

The reproducibility in the movement of the X-Y stage is very important in the spatial scanning of any dosimetric medium. There are two stepping motors that move the stage in x or y direction by rotating the threaded shafts attached to the motors. The threads of the shaft then in turn move the stage every time the shaft is rotated. However, once the movement stops and is then reversed, the counter rotation of the shaft can cause a backlash. This backlash can result in a systematic shift of the stage, thus shifting the coordinates of the dosimetric medium. Therefore, the stepping motors and the shafts must be designed by the manufacturer to compensate for this backlash movement.

To test the reproducibility of the scan, a vertical line was drawn on a film by a medium sized marker, and the film was then placed and secured on the X-Y stage. Using a step size of 0.1 mm and an effective aperture of 0.1 mm, $N = 20$ points were scanned from the left of the line to the right in the x (horizontal) direction. The same horizontal scan was repeated for another 10 times. Taking the very first scan of the line, $I_s(x_i)$, as the arbitrarily standard scan, any systematic shift in the subsequent scans, $I(x_i)$, can be detected by finding the minimum of the χ^2 as a function of the shift in x, i.e. Δx, between the standard scan and the subsequent scans. For each subsequent scan, the $\chi^2(\Delta x)$ is defined as,

$$\chi^2(\Delta x) = \sum_{i=1}^{N} \frac{[I_s(x_i) - kI(x_i + \Delta x)]^2}{\sigma_s^2 + \sigma_i^2}, \tag{3.3}$$

where σ_s^2 and σ_i^2 are the variances of $I_s(x_i)$ and $I(x_i)$, respectively, and k is the scaling factor between $I_s(x)$ and $I(x)$. This scaling factor can be determined by taking the partial derivative of $\chi^2(\Delta x)$ with respect to k and equating the derivative at zero. Then k can be evaluated by,

$$k = \frac{\sum_{i=1}^{N} w_i I_s(x_i) I(x_i + \Delta x)}{\sum_{i=1}^{N} w_i I^2(x_i + \Delta x)}, \tag{3.4}$$

where

$$w_i = \frac{1}{\sigma_s^2 + \sigma_i^2}. \tag{3.5}$$

Then, for each scan, the $\chi^2(\Delta x)$ was evaluated by shifting x at $\Delta x = 0$, and $\pm$ 0.1 mm. The minimum $\chi^2(\Delta x)$ and its shift were determined by assuming a parabola through the three evaluated points. Figure 3.7 shows the amount of shifting as calculated for the 10 scans using the χ^2 method described above. The uncertainties were calculated from the parabolic fit of the χ^2 and will be discussed in detail in Chapter 5. The shift appears to be random, and the largest shift in this set of data including the uncertainties is about 0.8 μm, which is about 13% of the smallest step size (6.35 μm) of the x-y scan. It is assumed that the stepping motor controlling the y direction would have similar results.

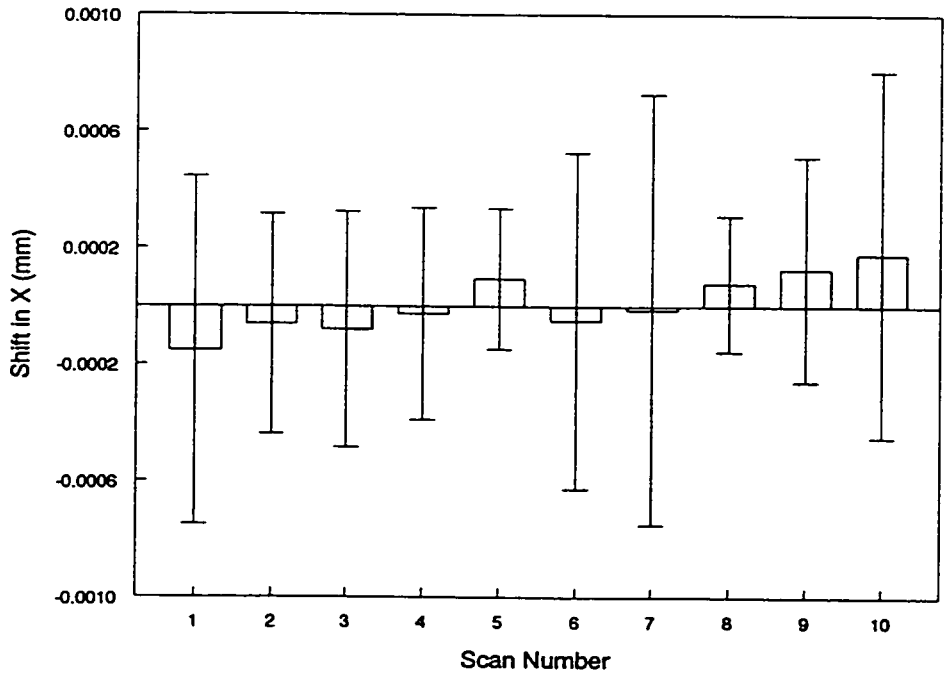

Figure 3.7 Histogram of shift in x

3.4 Resolution of the MSP

It is important to determine the resolution of the MSP because it determines the smallest structure that can be imaged. Moreover, once the resolution of a structure is determined, the objective magnification, the pinhole collimator aperture, and the scanning step size can be chosen to match the desired resolution. The resolution of the MSP was determined by two methods.

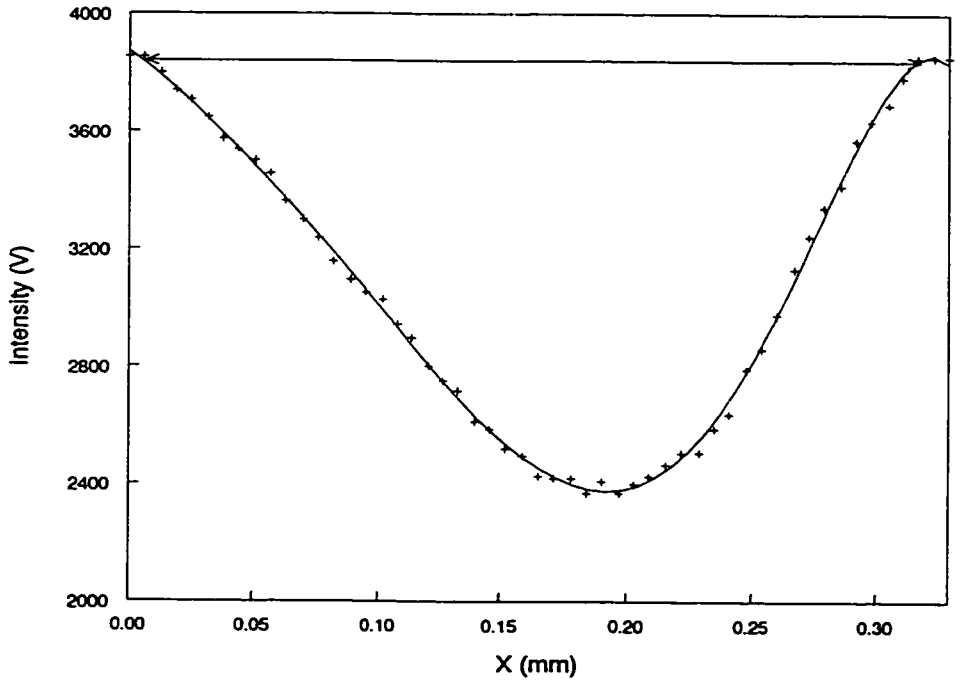

Figure 3.8 Resolution of a 70 μm wire

The first method involved scanning a straight thin wire in the direction perpendicular to the wire. The response function, $R(x)$, of the scan is then the convolution between the resolution function, $r(x)$, and the structure, $S(x)$, that was scanned. Hence,

$$R(x) = \int_{-\infty}^{\infty} r(u)S(x-u)du\,. \tag{3.6}$$

Ideally, the wire should be infinitesimally thin and opaque so that $S(x)$ can be represented by a delta function, and the response function would essentially be the resolution function of the MSP. But in practice, the wire has a thickness, and it must be corrected for. Figure 3.8 displays a horizontal x-scan at 662 nm of a 70 μm thick wire using the 5 mm pinhole, objective magnification of 25×, and a slit width of 0.25 mm. The focal plane was on the pinhole collimator, focussed on the wire edges. Note that the slit opening is in the x direction, i.e., parallel to the direction of the scan. Therefore, in theory, the resolution is not affected by the slit. The curve on the graph does not appear to be symmetric. This asymmetry is probably due to the fact that the wire was not perfectly straight. If so, the width of the curve on the graph would also be slightly broadened depending on the amount of bending of the wire. The resolution was determined by finding the width at the "base" of the inverse peak, as indicated by the arrows drawn on the graph, minus the width of the wire. In this case, the width of the "base" is approximately 0.29 mm, thus giving the resolution of the x-scan to be roughly 0.22 mm. This is in close agreement with the effective aperture, as calculated by equation (3.1), of 0.20 mm. This close agreement is not unexpected since the effective aperture should be the limiting factor for low resolution scans.

The scanning of a thin wire works well for resolution greater than the width of the wire. But when the resolution becomes close to or smaller than the wire width, diffraction around the wire and the structure of the wire itself would become the

dominating features of the curve. Therefore, a second method is preferred. The second method involves scanning a straight edge in the direction perpendicular to the edge. In theory, the straight edge should be infinitely sharp and opaque such that it can be represented by a step function. Then the response function of equation (3.6) becomes

$$R(x) = \int_{-\infty}^{x} r(u)E(x-u)du\,, \tag{3.7}$$

where $E(x-u)$ is the step function defined as,

$$\begin{aligned} E(x-u) &= 1 \qquad \text{if } u \le x, \\ &= 0 \qquad \text{if } u > x. \end{aligned} \tag{3.8}$$

Therefore, the resolution can be determined by taking the derivative of $R(x)$:

$$\frac{dR(x)}{dx} = r(x)\,. \tag{3.9}$$

Experimentally, it is difficult to find a perfectly straight edge on a microscopic scale. More importantly, differentiating a discrete function of experimental data may result in very low precision because the derivative is very sensitive to the noise in the data. In addition, as will be discussed later, the diffraction of the edge may also pose a problem.

Figure 3.9 shows a horizontal x-scan of an edge of a thin plastic card. The scan was performed at 662 nm using a pinhole diameter of 300 μm, objective magnification of 25×, and a slit width of 0.25 mm. The focal plane was again on the pinhole collimator, and the focus was on the edge. Note that the edge was carefully centered in the field of view in the eyepiece of the microscope and was arbitrarily given the x coordinate of zero. The graph has an unexpected shape in that the intensity begins to increase gradually at

about x = -70 μm until it almost reaches the edge where it begins to rise sharply. In addition, the edge is not at the average intensity of the maximum (I_o) and minimum intensities. It is roughly located at 0.25 I_o, though centering error could also be the cause of this "misalignment". These phenomena, however, are consistent with the fresnel diffraction of an edge. The fresnel diffraction of an edge predicts that the edge occurs at 0.25 I_o at every wavelength, and the diffraction pattern is dependent on the distance from the edge, both horizontally (on the edge plane and away from the opaque side) and vertically (in the direction away from the light source), and the wavelength of the light.

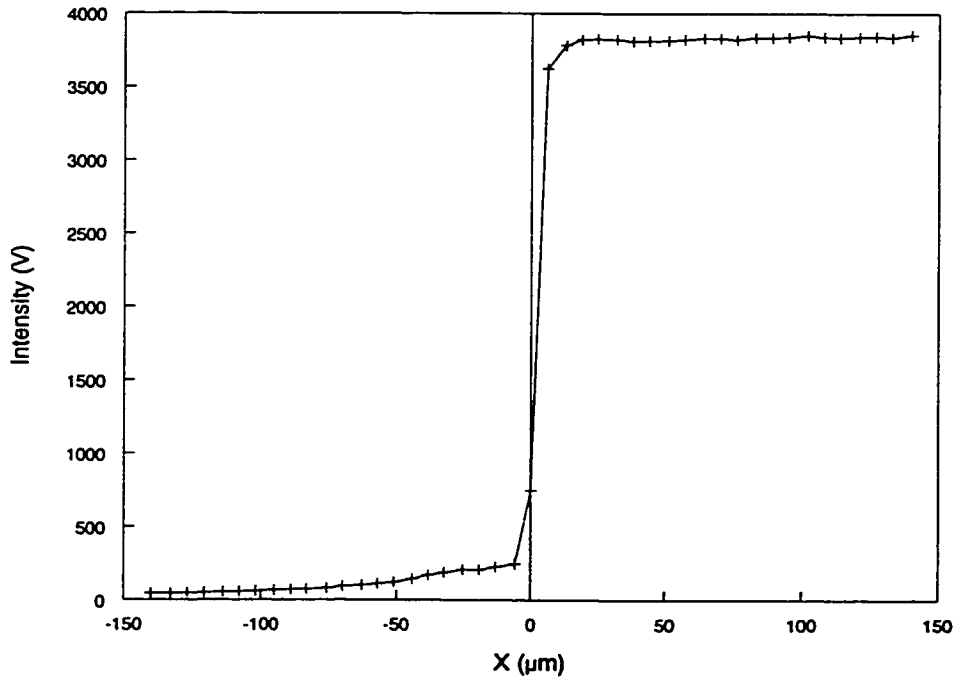

Figure 3.9 x-scan of a straight edge

To determine the resolution, the intensity pattern in Figure 3.9 was differentiated with respect to x. The result is demonstrated in Figure 3.10. In this case, the resolution was determined by estimating the width of the peak at its base, which is approximately 20

μm. This value is larger than the effective aperture of 12 μm. This discrepancy demonstrates that the effective aperture is not the limiting resolution in this case. Other factors such as the focussing on the pinhole collimator, the lens aberration, the optics in the monochromator, and even the edge structure itself could be the limiting factor. It should be pointed out that the secondary peaks around the central peak are probably due to the edge diffraction. However, the fresnel diffraction does not predict secondary peaks on the opaque side of the edge. It is speculated that their appearance may be due to the fact that the plastic card has a finite thickness. Thus, there are in fact, two corners on the edge, and the focus can be adjusted to either the top or the bottom edge. It is possible that diffraction from one of the edges could contribute to the secondary peak on the opaque side.

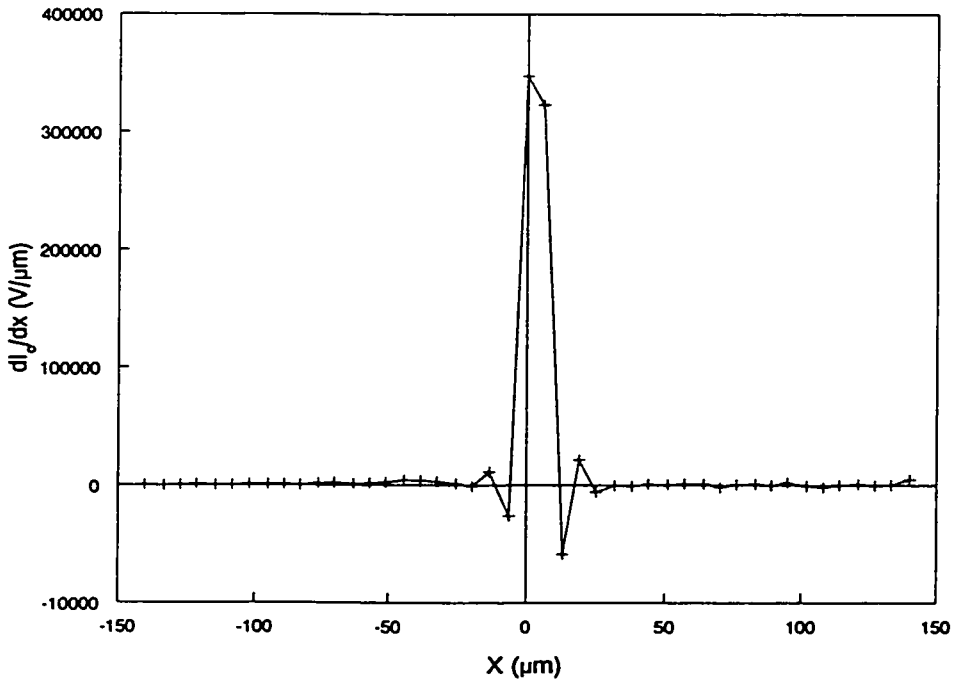

Figure 3.10 Derivative of the edge *x*-scan

Magnification (×)	Pinhole Aperture (μm)	Effective Aperture (μm)	Resolution in x (μm)	Resolution in y (μm)	Comments
25	5000	200	*220 ± 15	65 ± 5	* wire method
25	1000	40	50 ± 5 *(45 ± 5)	40 ± 5	* wire method
25	300	12	19 ± 2	25 ± 5	No change in resolution observed when input slit removed
25	100	4	19 ± 2	19 ± 2	
10	5000	500	600 ± 50	150 ± 10	
10	1000	100	100 ± 10	100 ± 10 *(400 ±50)	* max response on edge plane
10	300	30	30 ± 2	40 ± 5	
10	100	10	19 ± 2	25 ± 5	

Table 3.2 Resolutions determined at various objective magnifications and pinhole sizes

The resolution of other combinations of objective magnification (column 1) and pinhole size (column 2), using a slit width of 0.25 mm, is listed in Table 3.2. Column 3 is the effective aperture as calculated from equation (3.1), and columns 4 and 5 are the resolution in x and y directions, respectively, determined by the edge method unless stated otherwise. The uncertainties were determined by estimating the width of the peak. The results show that the best resolution that can be achieved is 19 ± 2 μm. The effective aperture essentially determines the resolution in the x and y directions greater than 19 μm, except for the case of the 5 mm pinhole in the y direction. This revelation indicates that the resolution in this case is likely to be limited by the slit width of 0.25 mm. A quick calculation reveals that the resolution can be approximately obtained by dividing the slit width by the objective magnification and then multiplied by a factor of six. Therefore,

the effective magnification of the two plano-convex lenses, located between the pinhole collimator and the slit, should be 1/6.

Using an objective magnification of 25× and a pinhole aperture of 1 mm, the resolution in the x direction was determined by both the wire and edge methods for comparison. The result demonstrates that both methods give roughly the same resolution within uncertainties. Other combinations of magnification and aperture were also attempted. But results were difficult to compare because of the high imprecision of either one of the methods. For high resolution, the structure of the wire dominates when using the wire method. While for low resolution, the derivative using the edge method produces a very broad oscillating peak, making it difficult to determine the width of the peak.

It should be noted that in many cases when the structure on the scanning medium is slowly varying, the focus does not have to be on the plane of the medium. Instead, the height of the X-Y stage can be adjusted to give the maximum response from the PMT. The advantage of finding the maximum sensitivity is that the signal tends to be more stable, while the maximum resolution relies on how well the focus can be achieved by the human eye, and the signal is very prone to the tilting problem of the X-Y stage. However, this maximum sensitivity is achieved at the expense of losing resolution. In Table 3.2, at an objective magnification of 10× and a pinhole size of 1 mm, the resolution in the y direction was determined at the maximum sensitivity. It was found that the resolution was 4 times the maximum resolution. It is not expected that this result is applicable for other magnifications and pinhole apertures. But it does provide a rough

idea of the largest scanning step size that should be used without sacrificing the resolution.

3.5 Other potential problems

The MSP is a very delicate instrument, and there are a number of potential problems that one should be made aware of. 1) The dust in the room can affect the light transmission if the dust grains sit on the lens or the dosimetric medium. It is believed that the dust comes from the ventilation system in the building. Therefore, before each measurement was made, an air puffer was used to blow the dust grains away from the instrument and the dosimeter. The MSP is now enclosed in a light tight case which also reduces dust. 2) The temperature affects both the light source and the dosimetric medium. Assuming the light source as a black body, the Stefan-Boltzmann law predicts the total radiancy, $R(T)$, is proportional to the T^4, where T is the temperature of the filament of the lamp. Hence, if ambient room temperature changes by ΔT, then the percentage change in the radiancy is,

$$\frac{\Delta R}{R} = 4\frac{\Delta T}{T}. \tag{3.10}$$

Therefore, assuming a filament temperature of 4600 K, a change in room temperature of 10 K will contribute to a change of radiancy of about 0.9%. The temperature in the laboratory, where the MDIS is located, is usually maintained at 22 ± 2 °C. However, occasionally, the temperature can become quite high or low due to a malfunction of the thermostat in the building. On those days, measurements were avoided. 3) The humidity

can affect the PMH, which needs to be cooled constantly during operation. At high relative humidity, water droplets can condense on the outside of the PMH. The water droplets can then fall onto the dosimetric medium, thus contaminating it. The humidity may also affect the light transmission through the dosimetric medium as was discussed in the previous chapter. A dehumidifier was put in place to reduce the moisture in the air. 4) It was found that the MSP was not completely light tight. However, no noticeable difference in the amount of light detected by the PMT was observed whether the room light was on or not. Despite the lack of noticeable difference, all measurements were done in dim or no ambient light since the radiochromic film is sensitive to light shorter than 600 nm. 5) The light source was found to be partially polarized before it passes through the dosimetric medium. Its effect is discussed in the following section.

3.6 The radiochromic film

The background and theory of the radiochromic film have been presented in Sections 2.8 – 2.10. As mentioned, the radiochromic films used in the research were the GDM of type MD-55-2 with lot # 941206 and 37175. The former lot is an earlier batch than the latter; therefore, is supposed to be less uniform. This was confirmed when the horizontal and vertical scans were made on these films. At 668 nm, it was found that the regional nonuniformity, defined as the difference in the intensities between the maximum and minimum response divided by the mean response, of the earlier batch to be about 7% in one direction, and 5% in another. The local nonuniformity varies tremendously because of the presence of occasional bad spots or "spikes". For the later batch, the local

nonuniformity, defined as the relative standard deviation of the transmitted intensity with respect to the mean, of three small films was found to be less than 0.5% at 668 nm. However, the regional nonuniformity and the standard deviation of the three films with respect to the mean were both found to be less than 3%. The comparison of uniformity with published results, such as those by Meigooni *et al.* (1996) or Zhu *et al.* (1997), is not very useful because past researchers have defined the film nonuniformity differently and with irradiated films. Instead, a more useful piece of information is the effect of nonuniformity on dose. If the nonuniformity is expressed as the difference between maximum and minimum optical densities, then the regional nonuniformity of 3% would correspond to roughly 1 Gy in dose.

The potential presence of polarization of the readout light source, the tungsten-halogen lamp, was investigated using a polarizer. The polarizer was placed on the X-Y stage of the MSP (see Figure 3.1). The polarizer was then rotated slowly while the light response at 610 nm was recorded at the PMT. It was discovered that response reading ranged from a maximum of about 3.83 V to a minimum of 2.33 V. Since the minimum response is not zero, the readout light source is only partially polarized. The polarizing effect on the film was then examined by replacing the polarizer with a piece of unirradiated radiochromic film. The light response was again recorded while rotating the film. It was found that the response variation, defined as the difference between maximum and minimum intensities divided by the mean intensity, was approximately 1% at 610 and 662 nm. This discovery shows that the polarizing effect on the film is

minimal. However, the film orientation should still be preserved in every scan because of the high precision measurements involved in all the experiments in this thesis.

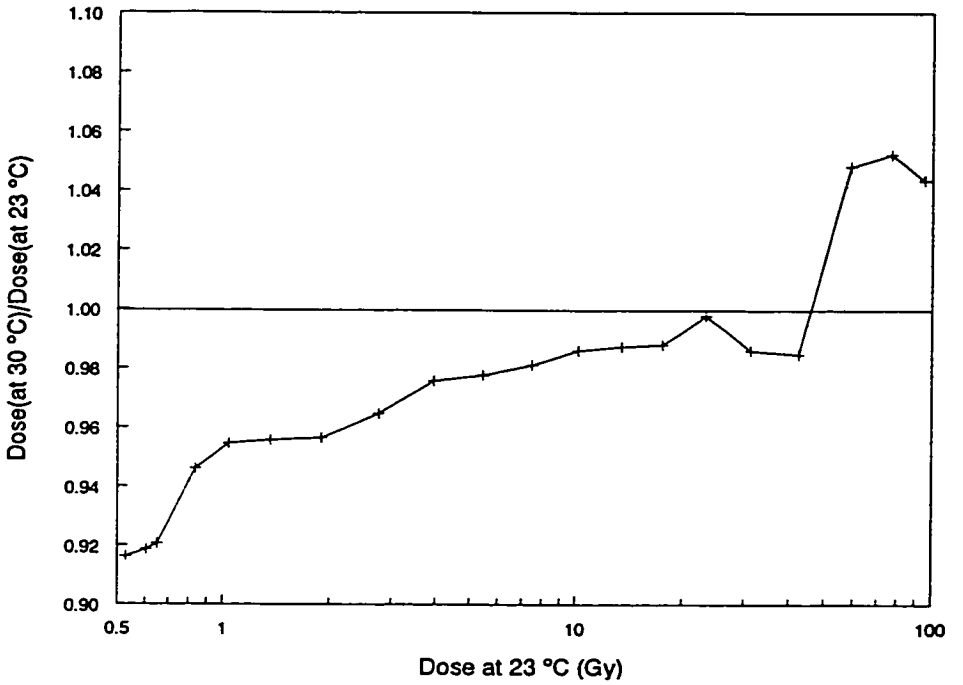

Figure 3.11 Temperature effect on film response

The effects of temperature on the GDM during irradiation and storage after irradiation were not investigated. But efforts were made to keep the films at room temperature at all stages of the experiments. An opportunity to examine the temperature effect on the film response during readout arose when the thermostat in the laboratory became temporarily malfunctioned. Two sets of measurements on a film with a varying dose distribution were made at 23 and 30 °C. The results are compared by calculating the ratio of the dose at 30 °C to that at 23 °C. The conversion to dose from measured optical density using multiple wavelengths will be described in detail in Chapter 5. The ratio as a function of the dose at 23 °C is displayed in Figure 3.11. The graph illustrates that below

about 55 Gy (at 23 °C), the dose at the higher temperature is lower than that at the lower temperature, and vice versa above 55 Gy. The maximum deviation occurs at very low doses, where the ratio is less than 0.92. This is not unexpected since, at increasing temperature, the optical density spectrum decreases in amplitude and shifts to shorter wavelengths. The combination of these two changes would result in either an increase or decrease in dose depending on the wavelengths chosen. However, the graph demonstrates the importance of scanning the film at a fixed temperature before and after irradiation for both the calibration films and the films for other experiments.

CHAPTER 4

EXPERIMENTAL PROCEDURES

Four sets of experiments involving irradiation were performed. The objective of the experiments is to irradiate a set of radiochromic films by γ-rays, β particles, or high energy electrons. The films were irradiated in a specific geometry so that the dose deposited into surrounding media could be measured, calculated, or simulated. The optical density measured from the films using the MDIS was then converted to dose (see Chapters 5 and 6), and the dose could then be compared to the calculated or simulated values. The success of the experiments can lead to future work involving more complicated geometries, such as dose deposition in a medium with heterogeneous interfaces.

The first experiment was on the uniform irradiation of radiochromic films by a ^{60}Co source to provide calibration data for other types of irradiation. Then in the second experiment, uniform β irradiation by a ^{32}P source was investigated. The β dose irradiation was performed to confirm that it could be determined from the ^{60}Co calibration. Therefore, it also provided an overall test of the methodology. The confirmation of the dose led to two more experiments involving the measurement of dose distribution within a medium by β and electron irradiations.

4.1 ^{60}Co γ irradiation

The γ irradiation was performed at the Hamilton Regional Cancer Center (HRCC), using the Cobalt C Theratron 780C unit. The unit is primarily employed for patient treatment and is located in the basement of the cancer center. The ^{60}Co source is stored in a lead casing in the source head of the Theratron. Below the source head is a bed that can be accurately adjusted by height and orientation. The room in which the ^{60}Co unit is located is shielded by 2 m thick of concrete. Outside the room, there is a control panel that controls many functions of the unit, including the period of irradiation.

E (keV)	Particle	*I* (%)
318.13	β^-	99.925
346.93	γ	0.0076
665.26	β^-	0.022
826.06	γ	0.0076
1173.237	γ	99.9736
1332.501	γ	99.9856
1491.38	β^-	0.057
2158.57	γ	0.00111
2505.00	γ	0.000002

Table 4.1 Decay properties of nuclide ^{60}Co

4.1.1 Properties of ^{60}Co

The ^{60}Co source is a γ and β emitter, both as a result of β^- decay. The half life of ^{60}Co is 5.2714 y. Table 4.1 lists the decay properties (Firestone 1996 and references therein). Column 1 lists the energy of decay particles (column 2) in keV. For β particles, the listed energy is the maximum energy of the particles. The last column is the

probability of decay of the particles (or branching ratio). The Table shows that there are three major decays of significance. They are β^- at $E = 318.13$ keV (96 keV average), and γ at $E = 1.173$ and 1.332 MeV.

4.1.2 ^{60}Co source calibration

The calibration of the ^{60}Co source was performed by a medical physicist or technologist at the HRCC. The procedure of the calibration is based on the Task Group 21 dosimetry protocol of the AAPM (Schulz *et al.* 1983). The equipment used for the calibration was a Capintec 0.6 cc ionization chamber, which itself was calibrated at the National Research Council at Ottawa. The calibration procedure involved placing the ionization chamber into a specially designed polystyrene phantom so that it was under 5 cm of build up and surrounded by polystyrene of saturation thickness. The center of the ionization chamber was aligned with the center of the ^{60}Co gamma beam. The distance between the source and the surface (SSD) of the polystyrene was 80 cm. The ^{60}Co unit had an encapsulation that stopped the β particles. Therefore, the only major contributions to the ionization chamber measurement were the 1.173 and 1.332 MeV γ photons. The field size, which is related to the source collimator width, was chosen to be 10×10 cm^2 on the phantom surface. At this distance and field size, the source activity at the ionization chamber had been found to be very uniform.

The ionization chamber current, with minor corrections such as ion recombination, reflects the amount of ionization occurring inside the chamber, which is

filled with air. The corrected current is proportional to the rate of dose deposited in the gas, and the dose rate was corrected to that at room temperature of 22 °C and standard pressure of 1 atm. The dose rate to the polystyrene was determined by using the Spencer-Attix formulation of the cavity theory (see Section 2.4.1). Finally, the dose rate was converted to the dose rate to water by the ratio of the mass energy absorption coefficients of the water and the polystyrene.

4.1.3 Radiochromic films calibration

4.1.3.1 Film preparation

A set of about 30 radiochromic films of size approximately 1 × 1.5 cm^2 each was cut from a batch of GDM MD-55-2 films (lot # 37175). The original films were of 5 × 5 in^2 (127 × 127 mm^2) each. Before cutting, each film was placed between two clean pieces of regular white paper. Then they were put on a paper cutter against an edge. The film was then cut into thin strips by the cutter knife. The reasons the paper cutter was chosen are its efficiency and accuracy in cutting. Afterward, with the film strips still between the paper strips, smaller films were cut to the desired size by a pair of scissors. The cutting was done in a dim room, with light coming from a small portable light panel away from the films. Since the films can be scratched or contaminated easily, clean latex gloves were worn, and only the edges of the film were handled, preferably by Teflon coated tweezers.

Each film was inspected visually for scratches or smudges. If dust grains were found on a film, they were blown off by a hand held puffer, used for cleaning camera

lenses. Due to the static build up on the film because of cutting and frequent handling, sometimes the dust grains had to be removed by gently picking them off of the film with a cotton ball. The use of a brush is not recommended, however, because it may leave scratches behind. 20 films without scratches or smudges were selected. Of those, 12 were randomly selected for irradiation, and 8 were allocated to be reference films. Therefore, for every 3 films chosen for irradiation, two reference films were assigned. Each film was then marked with a short line close to one corner by a permanent red felt pen to define its orientation.

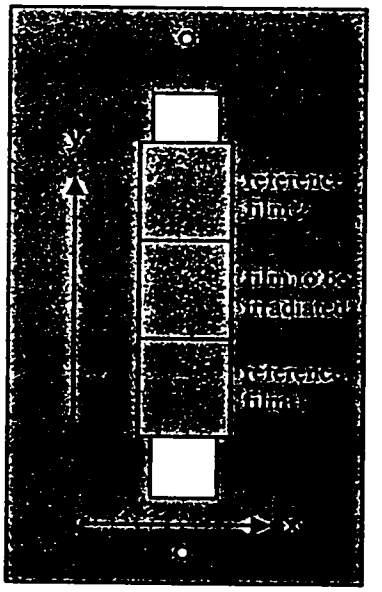

Figure 4.1 Diagram of the film holder

Before irradiation, every film to be irradiated was placed between two reference films in a specially designed film holder, and they were scanned simultaneously by the MDIS. Therefore, the reference films could detect and perhaps correct for any changes in

the signal due to, for example, the instabilities in the power supply, temperature, and humidity. Figure 4.1 displays the bottom plate of the film holder, with the films placed in the position as shown. The top plate, not shown, is similar to the bottom plate. The plates are utilized to sandwich the films to prevent movement during scanning. The film holder is placed on the X-Y stage, and the plate is secured onto the stage by screws. An objective magnification of 6× and a pinhole collimator size of 5 mm were used in the scanning. The height of the stage was adjusted for maximum sensitivity. These settings were chosen to reduce the noise due to the nonuniformity of the film and to improve the PMT signal-to-noise ratio. 10 spots on each film were scanned from 500 to 750 nm at a step size of 2 nm in the order of the first reference film, the film to be irradiated, and the second reference film. Then the scanner moved to the second spot (in the x direction) on the first reference film, and the scanning procedure was repeated 9 more times. The spatial scanning step size was 0.03" (0.762 mm) in the x direction. After irradiation, the irradiated films with their respective reference films were scanned in the same manner and the same positions as before to determine their optical densities.

4.1.3.2 Film irradiation

Once the films were pre-scanned, they were taken in a light tight black box to the HRCC ^{60}Co unit for irradiation. The reference films were also taken to "record" any ambient radiation that the other films might be exposed to. The films to be irradiated were placed in the polystyrene phantom similar to the one used to calibrate the ^{60}Co source, i.e. 5 cm beneath a build up and surrounded by saturation thickness (see Figure

4.2). Unfortunately, the polystyrene phantom was not very clean. To prevent contamination of the film by the phantom, two thin sheets of clean paper, normally used for holding weighing samples on a microbalance, were put on and below the film. Only one film at a time was irradiated at the same SSD and source field size as the source calibrating ionization chamber. In addition, it should be noted that the fluorescent lights in the irradiation room were turned on briefly to place and position the film properly before irradiation. While the irradiation took place, the fluorescent lights were turned off. But there were still dim incandescent lights in the room that could not be switched off.

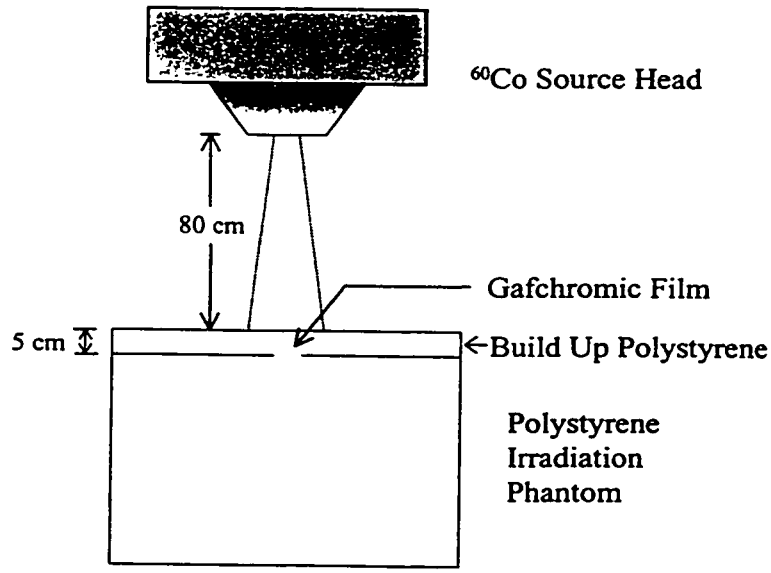

Figure 4.2 Diagram of the ^{60}Co source head and the phantom

The control panel outside the ^{60}Co unit allows an operator to set a timer that controls the irradiation period. However, the period of irradiation must be corrected for the transit time of the source, moving from its storing casing to its open position and

back, by adding 0.01 s to the total exposure time. This correction time had been determined by the medical physicist or technologist who performed the calibration. In addition, the maximum period that could be set by the timer was 20 minutes. Therefore, the timer had to be reset, and the transit time had to be corrected every 20 minutes for the films that required long exposure time. It should be noted that the irradiation took place only one day after the ^{60}Co source was calibrated, and all of the films were irradiated within a period of one week. Hence, decay correction to the calibrated dose rate was not necessary since the half life of ^{60}Co is 5.2714 y.

It should be pointed out that immediately after each irradiation, the irradiated film appeared to have uneven patches of blue colour over the entire film. At first, it was thought that the unevenness might be due to the pressure from the weight of the build up polystyrene. But it was discovered one day later that the unevenness seemed to have disappeared. In the end, 11 films were irradiated from 0.33 to 222.57 Gy, spaced semi-logarithmically. The remaining one film was not used due to a possible experimental blunder. The irradiated films were scanned 2 days after irradiation to obtain the optical density-to-dose conversion (see Chapter 5).

4.2 Uniform ^{32}P β irradiation

The purpose of the uniform β irradiation is to investigate the possibility of γ-β intercalibration and to test the optical density-to-dose method; thereby, confirming the expected dose deposited in the film by ^{32}P. The β source chosen for this experiment was

^{32}P because it is a pure β emitter, and its equilibrium spectrum as seen by the film is in the same order of magnitude as the spectrum of the recoil electrons produced by Compton scattering of the ^{60}Co γ photons. The β source and the films were placed in a specially designed irradiation facility so that the dose in the films could be calculated based on the equilibrium dose method.

4.2.1 Properties of ^{32}P

The ^{32}P source is a pure β emitter and has a half life of 14.262 d. Its only mode of decay is β^-, and it emits only one type of β particle with end point energy of 1.71066 MeV (0.6949 MeV average). At this energy, the particle has a CSDA range of approximately 8.2 mm in water, and 7.1 mm in polymethyl methacralate, or more commonly known as Lucite or Plexiglas.

4.2.2 The irradiation facility

The irradiation facility is a container for the ^{32}P solution. It was designed to provide irradiation to radiochromic films in a particular geometry and also has allow the experimenter to perform the irradiation safely and easily. In fact, the design was not easy to accomplish, and there have been many changes since the original one. The original design involved placing the radiochromic film, protected and stabilized by a thin piece of Mylar, on a Lucite block of thickness greater than the range of ^{32}P β particles. Then the block was immersed into a container, which was modified from a Tupperware container,

filled with the ^{32}P solution. The main problem with this design is that the Lucite block became very contaminated despite decontamination, making it unsafe to handle. Subsequent designs reduced the chance of contamination by eliminating direct contact between the block, which holds the film, and the source. Furthermore, each new design also improved on decreasing the air gap between the source and the film, and reducing the evaporation of the source.

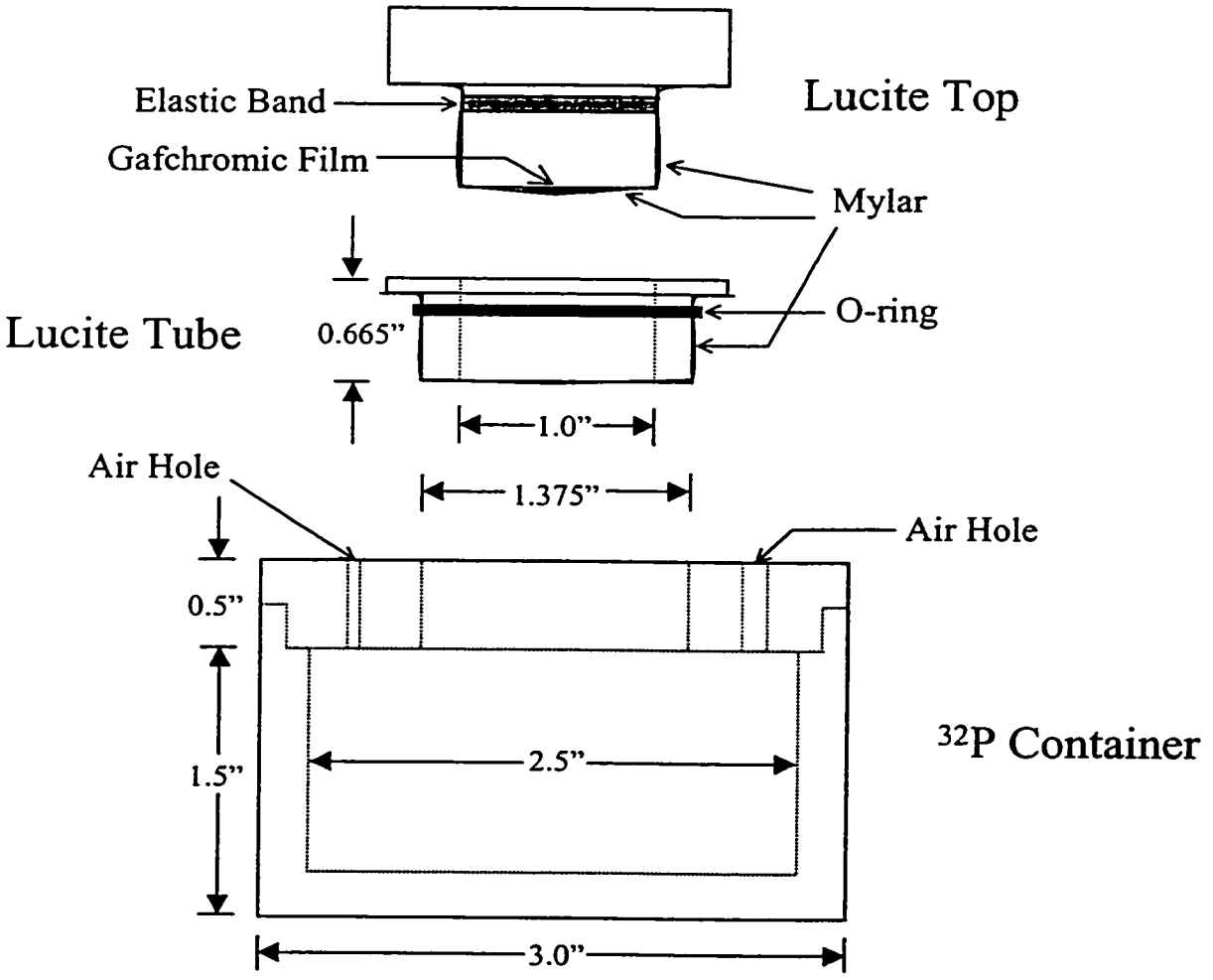

Figure 4.3 Diagram of the ^{32}P irradiation facility

Figure 4.3 shows the side view of the final version of the ^{32}P irradiation facility. The container was made from a Lucite rod with a diameter of 3" (76.2 mm) machined into a hollow container with a wall thickness of 0.25" (6.35 mm). The container was designed to hold 100 mL of liquid, and the wall was intended to eliminate most of the β dose from the source. At the maximum energy (1.7 MeV) of the ^{32}P β particles, the CSDA range in Lucite is approximately 7.1 mm or 0.28", with a Bremsstrahlung radiation yield of about 0.55 %. The cover, permanently sealed to the container, has one opening in the center and two air holes on each side, with one air hole slightly bigger than the other. The opening allows a hollow Lucite tube to be inserted semi-permanently. A piece of Mylar sheet of 2.5 μm thickness was stretched and glued to the underside of the tube, and the tube insertion was secured by an O-ring. The purpose of the Mylar sheet is to provide a barrier between the source and the radiochromic film, and along with the O-ring, to reduce evaporation of the solution. Once the Lucite tube is secured to the cover, the ^{32}P solution can be transferred to the container through the bigger air hole by using a syringe. Upon completion of the transfer, the air holes are plugged. But before the actual experiment could take place, deionized water was used to test the evaporation rate from the container. The test was carried out by observing the variation in weight of the water filled container. It was found that after 3 days, the amount of water loss was smaller than the detection limit of 0.1 g. Finally, the film to be irradiated is placed on the underside of a Lucite top (see Figure 4.3). The irradiation procedure will be described later in Section 4.2.5.

4.2.3 ^{32}P source preparation

25 mCi (925 MBq) of a ^{32}P source in the form of ortho-phosphoric acid (H_3PO_4 in H_2O) was purchased commercially and shipped via a courier. The source arrived in a carrier-free 0.05 mL solution and was stored in a thick glass vial enclosed in a lead container. Hence, the source needed to be extracted and diluted before it could be transferred into the Lucite container. To begin, 2 L of approximately 0.1 M HCl solution was prepared by diluting concentrated HCl into filtered deionized water. The HCl solution does not react with ^{32}P chemically and is acidic enough to extract the source, as much as possible, from the vial. The use of the deionized water is important because chemical residues in the water can react with ^{32}P, thus altering the uniformity of the activity of the solution. Then, the vial top was opened behind a beta shield, made with a 0.5" thick plastic sheet, with the supervision of a health physicist. Note that disposable latex gloves, film and ring badges had to be worn when handling the liquid source. A volume adjustable pipette, with a proper beta hand shield attached, was used to put 250 μL of the HCl solution into the vial with the source solution. After a few seconds of mixing, the combined solution was removed by the same pipette into a 100 mL volumetric flask, which was placed in a shielded beaker. The source extraction procedure was repeated 3 or 4 times to ensure most of the original source solution was extracted. The volumetric flask was then filled to 100 mL with the HCl solution. The combined solution was manually mixed very carefully and quickly. Then, it was allowed to stand for several hours before irradiation took place.

The diluted source solution in the volumetric flask was then transferred to the ^{32}P container using a 60 mL syringe. The syringe was shielded by a 1 cm thick plastic tube to reduce most of the β exposure to the hands. In later experiments, a lead shield was added onto the plastic tube to shield the Bremsstrahlung dose created by β interaction with the plastic. A long stainless steel needle was also required for the syringe. The needle had to be long enough to reach the bottom of the volumetric flask and also be small enough to go through the bigger air hole of the ^{32}P container. In addition to acting as the entrance hole for the needle during the transfer, the air holes also prevented any bubbles from building up on one side of the container. After 99 mL of the diluted source solution had been transferred, the remaining 1 mL was dispensed into a 1 L volumetric flask for radioassay. It should be noted that it was very difficult and not always possible to put all 99 mL into the container because of the inevitability of an air gap building up in the center of the container. After the source solution was transferred, the air holes were plugged by small pieces of putty. The container was ready for irradiation.

To perform the radioassay, the 1 mL solution dispensed into the 1 L volumetric flask was further diluted by the HCl solution to 1 L. Several samples from this further diluted solution were later taken to a liquid scintillation counter to be counted. The activity of the samples inferred the activity concentration of the ^{32}P source in the container. To double check the activity concentration and to monitor unexpected evaporation loss, another 1 mL was taken from the container upon successful completion of the irradiation experiments, and again, two weeks after the conclusion of the experiments. The two 1 mL samples were then transferred to two separate 500 mL

volumetric flasks and filled with the HCl solution. Samples from this diluted solution were counted as before.

4.2.4 Source activity

The activity concentration of the source solution in the ^{32}P container was determined by counting the removed samples. The dose in the film could then be determined based on the activity of the source. Originally, the samples were to be counted directly by a 4π β-counter. Unfortunately, the counter was not always available or fully functional. Therefore, the samples were counted by a liquid scintillation counter, which has been previously calibrated using a coincidence counting technique (Niven 1998). The coincidence counting technique involved counting a ^{24}Na source by both the 4π β-counter and a NaI γ-counter simultaneously. ^{24}Na emits both β and γ particles simultaneously in every decay. Thus, the coincidence counting of both particles allows the absolute activity of the source to be determined by eliminating the geometric efficiency dependence of the detectors. Once the absolute activity of the ^{24}Na source was determined, the counting efficiency of the liquid scintillation detector could then be calculated. The efficiency of counting ^{32}P could not be determined directly because ^{32}P does not emit any γ photons. Therefore, its efficiency was inferred by the counting of ^{24}Na because of its β energy proximity to ^{32}P. For the liquid scintillation counter, the efficiency of counting ^{32}P was taken to be $100 \pm 1.5\%$.

The activity concentration in the ^{32}P container was determined by measuring the count rate, C, of the samples with volume $V_{sample2}$ taken from the diluted solution in the V_{flask2} = 500 or 1000 mL volumetric flasks. The activity concentration in the container at the time of irradiation was calculated by,

$$[A] = \frac{A}{V_{flask1}} = \frac{C}{60\varepsilon} \frac{V_{flask2}}{V_{sample1} V_{sample2}} e^{\frac{t \ln 2}{T}}, \tag{4.1}$$

where C is the count rate in counts per minute (cpm) measured, ε is the counting efficiency of the detector, 60 is the conversion factor from cpm to counts per second, V_{flask1} = 100 mL is the volume of the ^{32}P container, $V_{sample1}$ = 1 mL is the sample volume removed from the container, T is the half life of ^{32}P, and t is the time from the beginning of irradiation to counting.

4.2.5 Experimental preparation and procedure

The radiochromic films were prepared in very much the same way as the ones used for the ^{60}Co irradiation (see Section 4.1.3.1). Once again, 20 films were selected out of over 30 that were cut from a batch with lot # 37175. Then 12 were selected for irradiation, and 8 were for reference. The films were also scanned in the same manner as their counterparts in the ^{60}Co irradiation, before and after the β irradiation. It should be pointed out that this experiment was attempted several times using older versions of the ^{32}P irradiation facility and GDM films, but without much success due large to the inadequate design of the irradiation facility.

Before the irradiation, the film was placed on the underside of a Lucite top, as illustrated in Figure 4.3, and held by a piece of 2.5 μm thick Mylar sheet. The Mylar sheet wrapped around the bottom part of the Lucite top and was secured by a thin elastic band. Then the film was irradiated by inserting the top into the Lucite tube. After the insertion of the top, the film was irradiated in a geometry such that one side of the film faced the ^{32}P solution with depth greater than the β range, and the other side faced the Lucite top of thickness also greater than the β range. In the end, 11 films were irradiated one at a time over a course of 2 weeks. The uncorrected dose deposited in the films ranged from 0.3 to 266 Gy.

4.3 Edge-on ^{32}P β irradiation

The edge-on irradiation experiment was designed to measure the dose distribution within a Lucite block irradiated by a volume ^{32}P source. The experiment was performed twice. The first trial was done immediately after the uniform ^{32}P irradiation experiment was over, while the source was still fairly active. The second trial was performed independently. The goal of the second trial was mainly to confirm the dose obtained in the first trial, and to address the potential problem of ambient UV radiation in the laboratory.

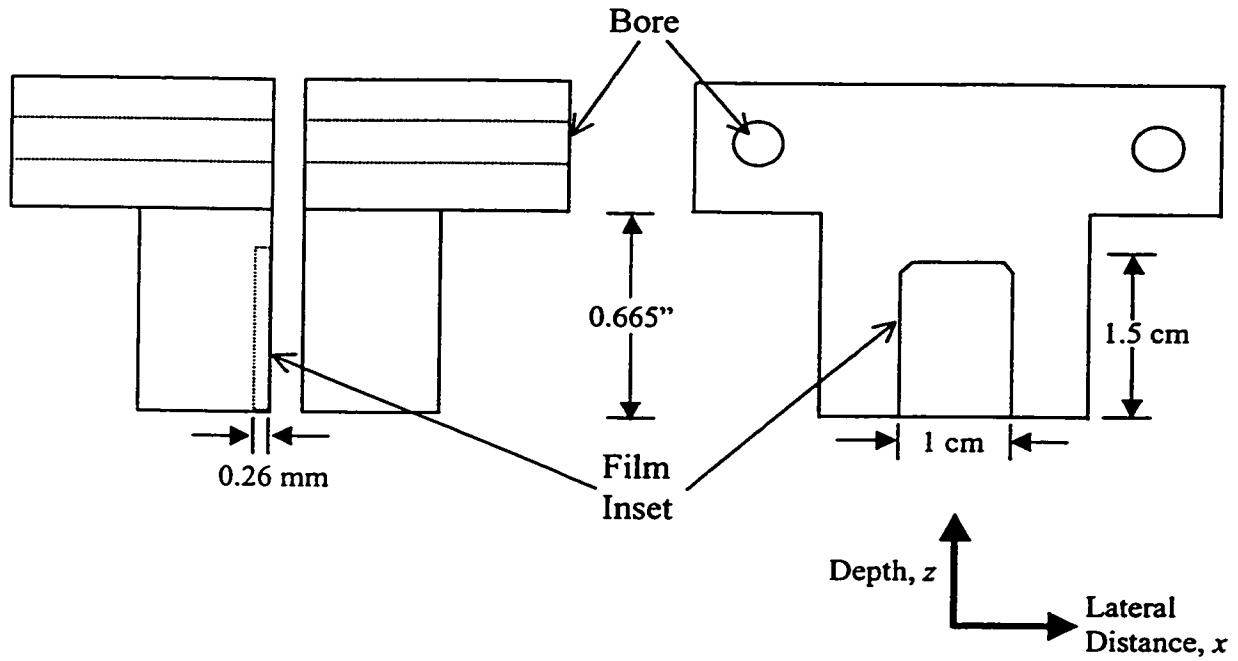

Figure 4.4 Diagram of the split cap. (Left) Main view. (Right) Side view of the left split cap.

4.3.1 Experimental design and preparation

The experimental design is very similar to that of the uniform ^{32}P β irradiation. The source container is the same one used in the uniform irradiation. However, in the edge-on β irradiation, a radiochromic film was placed between a split cap in a direction such that the film was perpendicular to the source solution. Figure 4.4 shows a drawing of the split cap. The film was cut to fit into the dimensions of an inset 0.26 mm deep on one of the split caps, and was secured by putting pressure on the film by tightening two plastic screws. It was found, however, that if too much pressure was put on the film, it could be creased, or scratched even with the slightest lateral movement by one of the split caps. But if not enough pressure was applied, the film could fall partially or completely

out of the cap. Furthermore, after the screws were tightened, small gaps appeared from both lateral edges of the cap. To solve both problems, a thin piece of Mylar was used to wrap the film to protect it from being scratched. A small amount of Lubriseal™, a hydrocarbon based product, was then applied to paste the Mylar to the cap and to fill in the gaps. Without the worry of the film being scratched, more pressure could be applied to hold the film in place.

4.3.2 Film preparation before irradiation

The selection of the film was more stringent than those films selected for the uniform irradiation. Typically, the maximum local variation of transmission on a film is less than 3%, excluding occasional bad points. The film not only had to pass the initial visual inspection. It was also scanned by the MDIS at a fixed wavelength to ensure the absence of any bad points. The film was pre-scanned along with two other reference films in a similar way to the other films for the uniform irradiation, at the same set of wavelengths. However, the objective magnification for this experiment was chosen to be at 10×, while the pinhole aperture of 1 mm and the height of the stage set to achieve maximum sensitivity remained unchanged. Furthermore, 11 points were scanned horizontally (in the x direction parallel to the short sides of the film, i.e. parallel to the source boundary) on each film with 0.02" (0.508 mm) between horizontal points. The scanning order, however, was the same as that for the films in the uniform irradiation experiment. The films were also marked near one corner to define its orientation. In addition, the front edge of the film to be irradiated was lined up so that it appeared to be

in the center as viewed in the eyepiece of the MSP when scanned across the x direction. The front edge was arbitrarily given a y coordinate of zero.

4.3.3 Film readout

The film was irradiated in the ^{32}P container until its edge dose was about 270 Gy in the first trial and about 400 Gy in the second. In both trials, the irradiation lasted for approximately 2 weeks. It was found in the first trial, the lights in the laboratory, where the irradiation took place, were occasionally left on for hours and possibly days by other experimenters. Therefore, in the second trial, the experiment was carried out when the other experimenters were away, and a black cardboard paper was put over the irradiation facility to shield it from any ambient light.

After irradiation, the irradiated film was inspected visually to determine if scratches or smudges appeared on the surface. Several tiny spots, of what appeared to be Mylar residues, were found. The irradiated film was painstakingly aligned so that its orientation would be as close as possible to the original position before irradiation. The irradiated film was first scanned along with the two reference films in exactly the same way as before irradiation, using the same step size and effective aperture. If a bad spot, such as a scratch or a smudge occupied one of the pre-scanned positions, then it would be avoided. Instead a new scan in the y direction of the three films was chosen. The optical density would eventually be calculated based on the new positions in the post irradiation scan, and the closest old positions in the pre-irradiation scan. After the first post irradiation scan, the irradiated film was scanned in the y direction from the front edge to

the far end of the film. The scan was performed 10 times in the same x coordinates as the first post irradiation scan. Note that the points on the irradiated film that were scanned earlier had to be included in this scan. The spatial scanning step size in the y direction was 0.01" (0.254 mm) in the first trial, and 0.02" (0.508 mm) in the second.

4.4 Edge-on 10 MeV electron beam irradiation

An electron irradiation experiment to measure the dose distribution within a large Lucite block irradiated by a 10.05 MeV electron beam was also performed. The experiment was performed at the National Research Council (NRC) at Ottawa by two scientists, Norman Klassen and Carl Ross.

4.4.1 The phantom

The phantom is made essentially of two large Lucite blocks put together (see Figure 4.5). When put together, the phantom has a dimension of $7 \times 7 \times 7$ in^3 ($177.8 \times 177.8 \times 177.8$ mm^3). The blocks are held together by 4 long plastic bolts and nuts. One of the blocks has an inset with area of 5×5 in^2 (127×127 mm^2) and 0.26 mm depth so that an uncut GDM film can be placed snugly into it, and one side of the inset extends to the face of the phantom. This face of the phantom will be referred to as the top side of the phantom since this is where the electron beam would enter. A small rectangular frame is added to the center of the top side of the phantom. This frame allows a smaller film, which is marked with 4 dots to match the corresponding slots of the phantom, to be

placed under it. The purpose of this film is to obtain information on surface lateral beam profile.

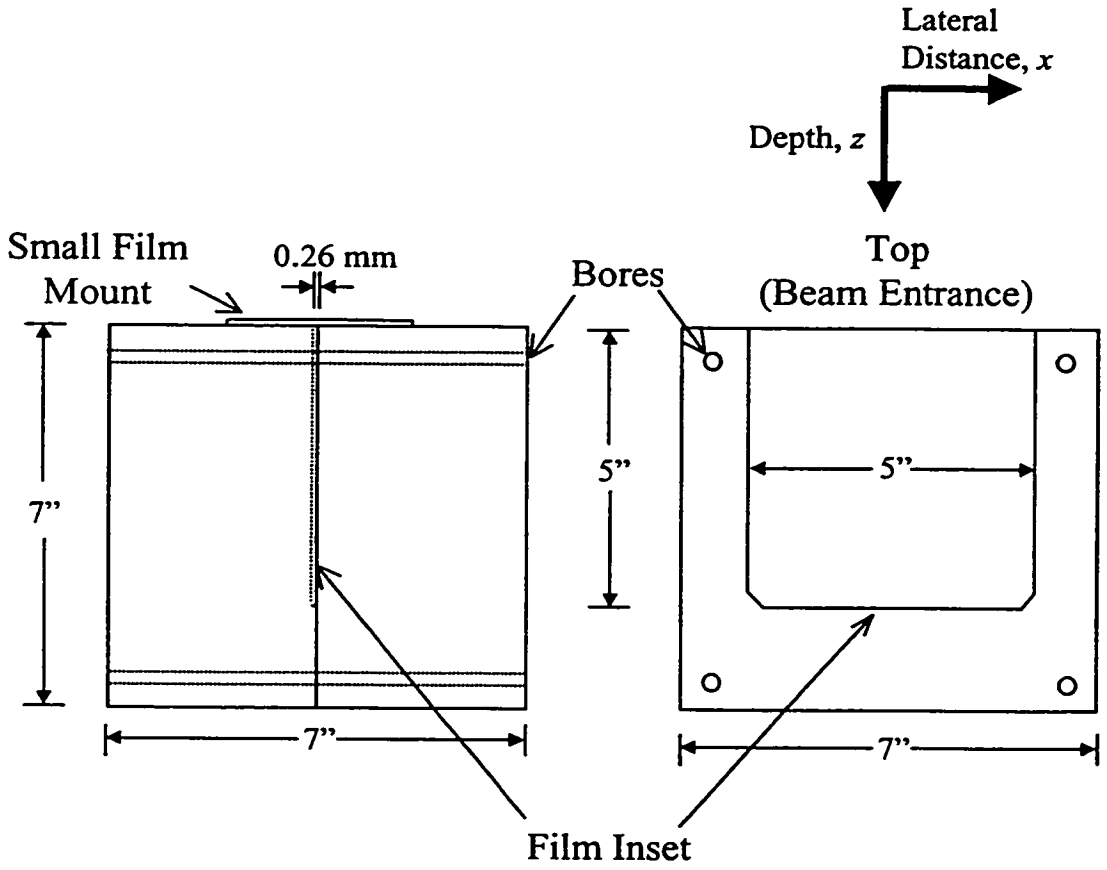

Figure 4.5 Diagram of the Lucite phantom. (Left) Main view. (Right) Side view of the left Lucite block.

4.4.2 Film preparation

A batch of 3 uncut GDM films of lot # 941206 was used in this experiment. These films are older than the ones of lot # 37175 and have been found to be quite nonuniform (Meigooni *et al.* 1996, Zhu *et al.* 1997) in their optical densities.

Unfortunately, when the irradiation equipment was available at the NRC, newer versions of the GDM films were not available.

The films were not pre-scanned for two reasons. First, the entire film without being cut could not fit on the X-Y stage. Second, in theory, not every part of the film would be irradiated by the electrons. Therefore, the unirradiated part of the film could be used as the reference region for the optical density.

4.4.3 Experimental setup and procedure

The experimental setup and procedure were given by Klassen and Ross (1997). The equipment that was used to produce the electron beam was a linear accelerator (linac). The electron beam had an energy of 10.05 MeV, and the full width at half the maximum energy of the distribution was 0.4%. The systematic uncertainties of the peak of the energy distribution were estimated to be less than 0.4%. The physical width of the electron beam was 3 mm, and the average electron current was 0.1 nA. The phantom was positioned such that its top side was facing the beam, i.e., the embedded large film was vertical, and the small film was on top. The phantom was placed in a jig so that the electron beam would strike the center of the phantom. In this position, the beam had to travel through a 0.005" stainless steel window and 9 mm of air before reaching the phantom. This positioning was made possible by using a He-Ne laser beam, which was set to the axis of the electron beam.

Three films were irradiated separately. Their approximate irradiation periods were 5, 50, and 640 s. The beam current was monitored indirectly by measuring the

Bremsstrahlung photons in the downstream of the phantom by a 35 cc ionization chamber. It should be mentioned that before the actual experiment took place, the scientists who performed the experiment did two irradiation measurements using their own films to confirm that the beam was on the center of the phantom.

4.4.4 Film readout

After the experiment, the films were sent back to be analyzed. Since the full size films were too large for the X-Y stage, they had to be cut into two pieces. A plastic film holder was designed to hold a film with the maximum size of 5×3 in^2 (127×76.2 mm^2). The film holder is essentially comprised of two frames. The first frame fit snugly on the X-Y stage. It has an inset that allowed a film to be placed on it. The second frame was put on top of the first frame after the film had been placed. The second frame had a "cushion", made of weather stripping, attached. The "cushion" allowed pressure to be put on the edges of the film without damaging it. The pressure was put on the edges so as to prevent the film from moving and also sagging in the center. This pressure was created by tightening the screws that went through both frames into the stage bores.

The irradiated films were each scanned by using an objective magnification of 10×, with pinhole aperture of 1 mm. The height of the stage was adjusted to provide maximum sensitivity. The scan was done in the x direction (lateral direction perpendicular to the beam axis) at a fixed wavelength first. Then the scan was repeated at a different wavelength until all 126 wavelengths, from 500 to 750 nm at a step size of 2 nm, were completed. Once the x-scans were completed, the scanner would move to a

new y coordinate and repeat the x-scans again. A typical horizontal scan at all wavelengths could take over 2 hours to complete. But prolonged exposure by the scanning light source to any parts of the film could lead to an increase in dose recorded by those parts of the film. Since the aperture, about 1 mm, of the light transmitted through the film is typically larger than the scanning step size, it is imperative to scan as few points, and as quickly at each point, as possible. The spatial scanning width and step size depended on the dose and the gradient dose distribution on the film. For the scans near the front edge of the film (at the beam entrance), the step size used was 0.02" because of the large dose gradient. But the scanning width in the x direction was also smaller because the beam had not spread much near the front edge. The scanning width was determined by finding the regions where the dose deposited was not significantly different than the inherent noise in the film. These regions will be referred to as the blank regions. In the regions away from the front edge of the film, the blank regions might not be found because of the wider beam spread at increasing depth. Therefore, the scanning width was selected to be the limit of the horizontal stepping motor. The optical density of these regions was then referenced to the blank regions located near the front edge or far corners of the film if the optical density was lower there.

CHAPTER 5

OPTICAL DENSITY-TO-DOSE CONVERSION

The GDM radiochromic film, as discussed earlier in Section 2.8, is a thin, transparent dosimeter that changes from almost colourless to blue when exposed to ultraviolet light and ionizing radiation. The amount of colour change, or its optical density at certain wavelengths, is dependent on the absorbed dose in the film and can be determined by measuring the transmitted intensities through the film before and after it is irradiated. However, before the film is used for measuring radiation dose, it has to be calibrated. In general, the calibration can be performed by irradiating a set of films with known doses. Then an unknown dose given to a film can be determined by comparing the optical density of this film with that of the calibration films. Two methods are described in this chapter.

5.1 Common method

Currently, there are a number of methods to convert the measured optical density into dose. Strictly speaking, the optical density, OD, also known as the absorbance, is defined as,

$$OD(\lambda) = \log\left(\frac{I_{\circ}(\lambda)}{I(\lambda)}\right), \tag{5.1}$$

where $I_{\circ}(\lambda)$ and $I(\lambda)$ are the intensity responses without and with the film, respectively. However, the parameter of interest is commonly referred to as the net optical density or net absorbance, where $I_{\circ}(\lambda)$ and $I(\lambda)$ are the film responses before and after irradiation, respectively. For convenience, from here on, mention of the optical density is implicitly taken to be the same as the net optical density. The uncertainty in the $OD(\lambda)$ can be calculated by,

$$\sigma(OD) = \frac{1}{\ln(10)} \sqrt{\left(\frac{\sigma(I_{\circ})}{I_{\circ}}\right)^2 + \left(\frac{\sigma(I)}{I}\right)^2}, \tag{5.2}$$

where $\sigma(I_{\circ})$ and $\sigma(I)$ are the uncertainties in the $I_{\circ}(\lambda)$ and $I(\lambda)$, respectively. The most common method is to choose a fixed wavelength, λ, and then fit an interpolation spline or a polynomial curve to a set of known doses as a function of measured optical densities, $d(OD)$, for calibration. Then the unknown dose deposited in a film can be determined by measuring its optical density, OD_u, at the fixed λ, and the dose can be evaluated by the fitted function, $d(OD_u)$. Figure 5.1 displays a typical spline fitted $d(OD)$ curve at $\lambda = 668$ nm. Note the saturation effect at an optical density of 2.6, and the onset of nonlinearity in the region of $OD > 2$. This response limits the useful range to about 50 Gy.

The fixed wavelength is usually selected depending on the dose range. For doses smaller than 50 Gy, λ is usually chosen at or near the major absorption peak (see, e.g., Figures 5.2 and 5.3) due to its high sensitivity, thus higher signal-to-noise ratio. Because

of the saturation mentioned above, for doses greater than 50 Gy, λ is usually chosen at or near the minor absorption peak, or the trough in between the major and minor peaks.

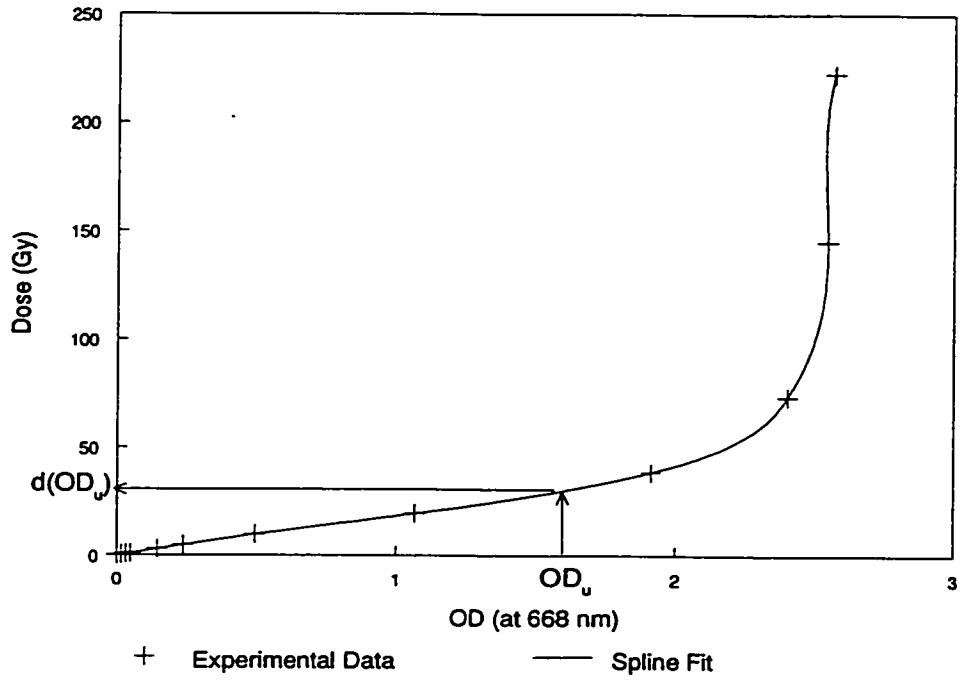

Figure 5.1 Dose as a spline fitted function of *OD*

This fixed-wavelength method (FWM) provides good conversion for a range of doses from about 3 to 100 Gy (McLaughlin *et al.* 1996, Zhu *et al.* 1997). But as the dose increases beyond 50 Gy, the optical density at the major peak at about 675 nm begins to saturate, and the accuracy of the optical density-to-dose conversion is reduced. Figure 5.2 displays the spectral *OD* curve at absorbed dose from 39 to 223 Gy. This curve shows the saturation of the major peak at 74, 145, and 223 Gy, and the saturation of the minor peak at 223 Gy. Note that the data were obtained from the ^{60}Co irradiation (see Chapter 4), and the absorbed dose was calibrated to water. The irradiation procedure has been described in detail earlier in Chapter 4.

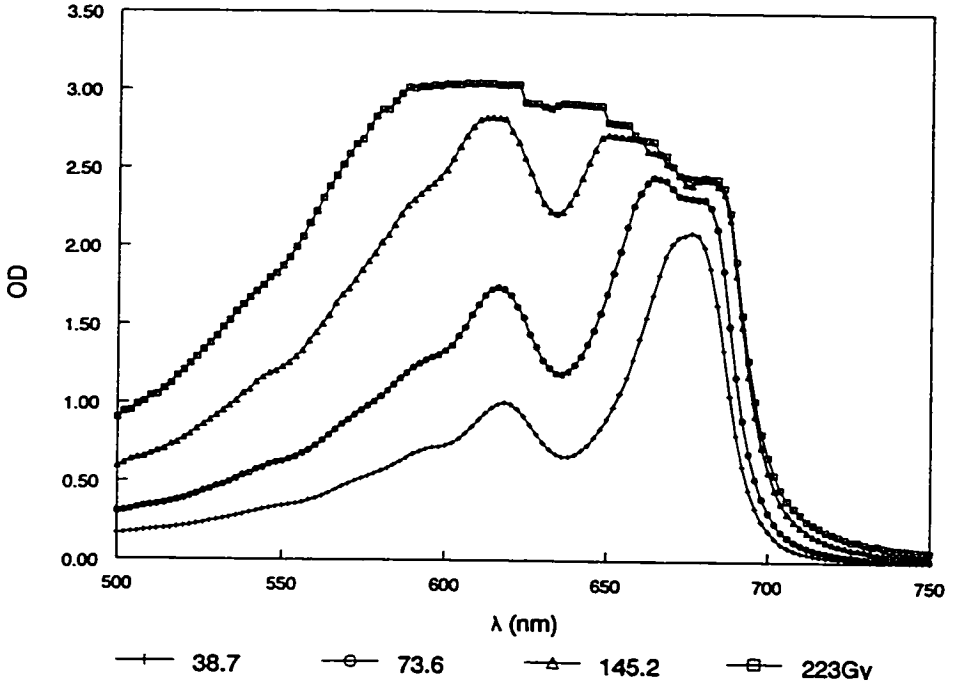

Figure 5.2 *OD* as a function of λ at high doses

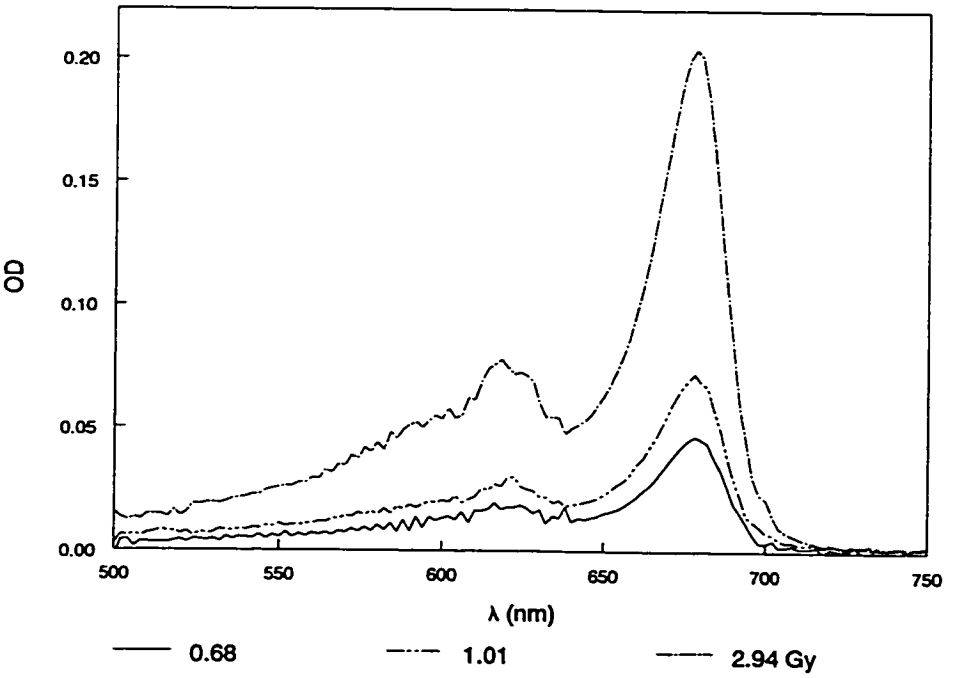

Figure 5.3 *OD* as a function of λ at low doses

When the dose is below 3 Gy, interference due to internal reflections in the thin film itself (Klassen *et al.* 1997) may reduce the sensitivity and accuracy of the film response. The interference noise is illustrated clearly in Figure 5.3. The spectral curve also shows that the interference is more pronounced at low signal-to-noise regions, and the period of the interference in λ is somewhat irregular. Details concerning the interference are described in Section 5.2.1. In addition, it should be mentioned that in Figures 5.2 and 5.3, both the major and minor peaks shift to shorter wavelengths with increasing dose, adding to the nonlinearity of the $d(OD)$ curve.

5.2 New method

A newly created method of determining an unknown dose in the film is proposed here as follows. First, a set of 11 calibration films with known doses was acquired. The films were irradiated by the ^{60}Co unit at the HRCC with doses to water from about 0.33 to 223 Gy, spaced almost logarithmically. Then the films were scanned by the MDIS at wavelengths from 500 to 750 nm at a step size of 2 nm. The data determine the optical density as a function of wavelength and dose, $OD(\lambda,d)$. They comprise a discrete sample of the OD surface in wavelength-dose space.

5.2.1 Thin-film interference and filtering

Due to the GDM film thickness of approximately 260 μm, thin-film interference is very pronounced at low doses, and at wavelengths with low signal-to-noise ratio. The

film itself is comprised of 7 layers made of 3 different materials (Klassen *et al.* 1997, Niroomand-Rad *et al.* 1998). The interference is due to the internal reflection of the light at any of the inner surfaces in the film. To demonstrate how the interference arises, an example of a simple case of a uniform layer is given below.

For an incident light passing through a uniform film in air with a thickness, l, constructive interference may occur for the internally reflected light if the appropriate phase condition is satisfied. This condition will occur if the thickness of the film equals an integral number of half-wavelengths so that the reflected light out of the film is in phase with the refracted light, since there is no phase shift in the reflected light. The total path length traveled for successive reflections is $2l$ so that the condition can be summarized by,

$$2l = m\lambda_f , \tag{5.3}$$

where m is any positive integer, and λ_f is the wavelength in the film. For destructive interference,

$$2l = \left(m - \tfrac{1}{2}\right)\lambda_f . \tag{5.4}$$

The above equations indicate that very small change in the film thickness, l, can result in a large change in the interference. The intensity of the interference also depends on the amount of light absorption by the film. If the absorption is high, then the internally reflected light for the nth round trip would be attenuated by $e^{-2n\alpha l}$, where α is the attenuation coefficient. This phenomenon can be seen in Figure 5.3 where the region

with high absorbance, i.e. $OD(\lambda)$ from about 660 to 690 nm, has generally smaller interference noise than the regions with low absorbance.

In a real GDM film, however, the various layers with different thickness and index of refraction make the condition for interference harder to predict because the internally reflected light would also undergo a phase shift from a less dense to a more dense layer, and every layer surface can cause reflection. In addition, since the film does not have perfectly uniform thickness, the response at different points on the film may vary in amplitude of the interference noise.

The interference noise can be reduced or smoothed by a mathematical process called filtering. If the $OD(\lambda)$ function could be separated into two components: the true response component and the noise component, then the noise can be filtered by integrating the $OD(\lambda)$ over a suitable range of λ. If the noise component is periodic, then the integral over the period of the noise is zero. But in this case, there is no unique period. The filtering was done by averaging every 5 consecutive $OD(\lambda)$ points over 8 nm to produce a new, smoothed $\overline{OD(\lambda)}$, calculated by,

$$\overline{OD(\lambda_{N+2})} = \sum_{i=N}^{N+4} \frac{OD(\lambda_i)}{5}. \tag{5.5}$$

The standard deviation of the new $\overline{OD(\lambda)}$ was calculated by averaging the square root of the sum of the variances in the unfiltered $OD(\lambda_i)$. The number of points needed for the filtering was determined by trial and error, and the averaging of 5 points appeared to be adequate in smoothing out the noise. Figure 5.4 demonstrates the effect of filtering on the

$OD(\lambda)$ curve at 1 Gy. The filtering reduces the amplitude of the noise, but also the amplitude of the peaks slightly.

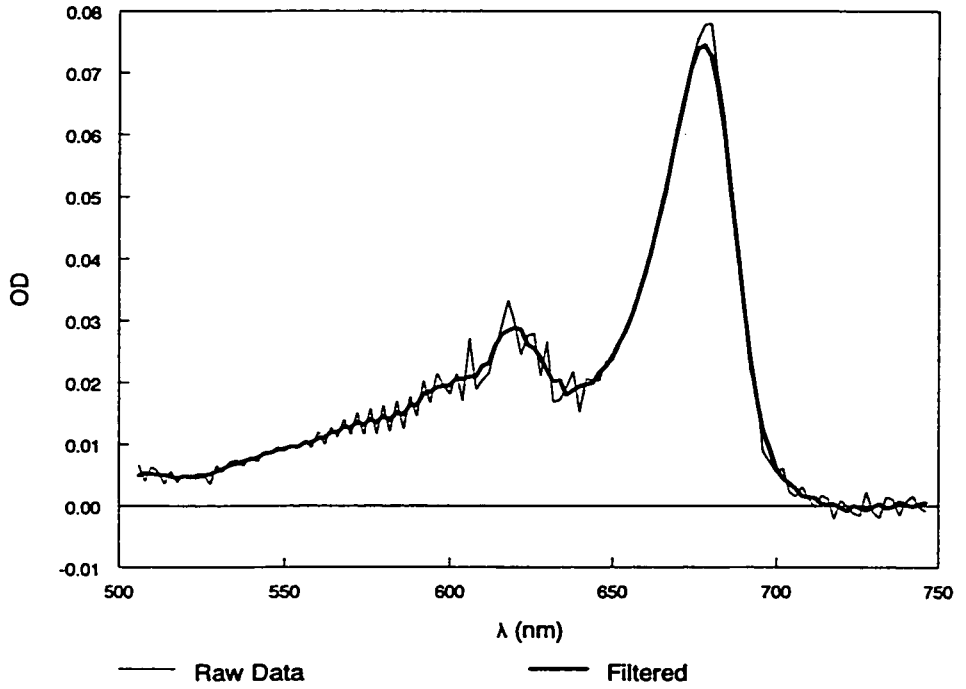

Figure 5.4 Filtering effect on $OD(\lambda)$

It should be pointed out that the noise in the $OD(\lambda)$ cannot be completely eliminated for two reasons. First, equations (5.3) and (5.4) show that the interference is dependent on the wavelength in the film. Therefore, the period of the interference in the $OD(\lambda)$ varies with λ. Second, although the $OD(\lambda)$ is defined as the log of the ratio of the film response intensities before and after irradiation, in practice, the measurement is always performed with respect to one or more blank reference films (see Chapter 4). Therefore, the interference pattern in the intensity response will always be different from

that in the $OD(\lambda)$. Figure 5.5 illustrates the difference of the optical densities between the filtered and non-filtered curves shown in Figure 5.4. On this curve, the period of the interference noise appears to be random in some regions, and regular in others. This is probably due to the pseudo-superimposition of the interference noise from the irradiated film and the reference films. Therefore, ideally, one should filter the intensity noise from every film before computing the optical density. But experimentally, filtering the $OD(\lambda)$ calculated by unfiltered intensities appears to be adequate in smoothing the interference noise.

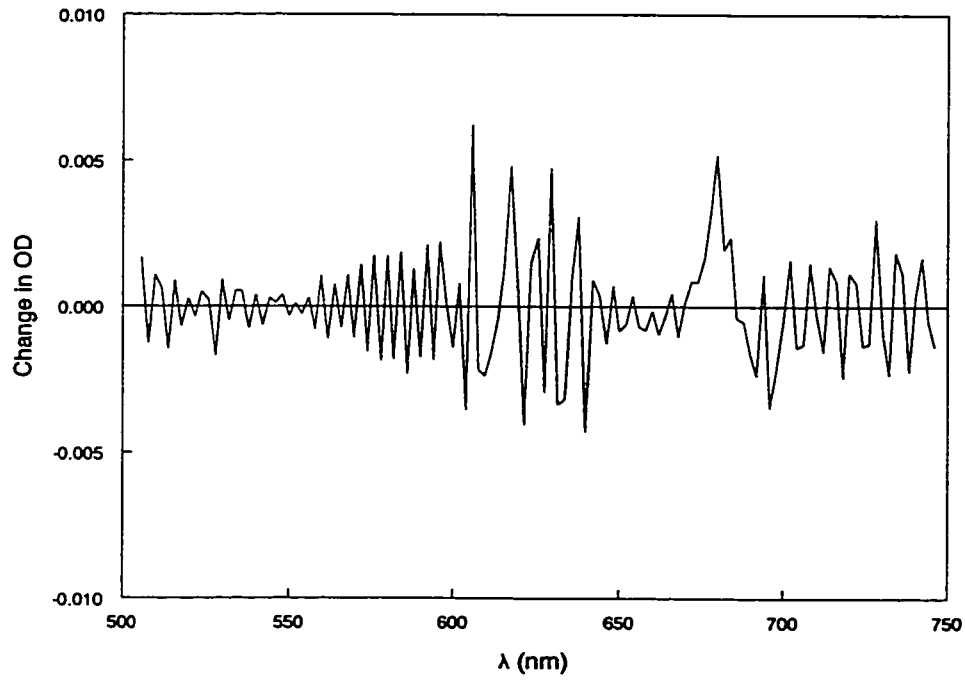

Figure 5.5 Difference in filtered and unfiltered $OD(\lambda)$

5.2.2 2-d spline interpolation and χ^2

The calibration surface, $OD(\lambda,d)$, was fitted with a two-dimensional bicubic interpolation spline, $S(\lambda,d)$. The two-dimensional spline fit was done by using a Fortran subroutine, Regrid, written by Dierckx (1993). The fit is achieved basically by passing a bicubic surface through every point on the $OD(\lambda_i,d_j)$ in the form of

$$\begin{aligned} S(\lambda,d) = {} & a_i(\lambda-\lambda_i)^3 + b_i(\lambda-\lambda_i)^2 + c_i(\lambda-\lambda_i) + \\ & a'_j(d-d_j)^3 + b'_j(d-d_j)^2 + c'_j(d-d_j) + k_{ij} \ . \end{aligned} \tag{5.6}$$

Then, at every end point in a bicubic surface "interval", the slopes and the curvatures must be the same for other surfaces that join at the same point in both λ and d directions.

The optical density as a function of wavelength, $OD_u(\lambda)$, of the film deposited with an unknown dose was then measured, filtered in the same way as the calibration data, and compared with the fitted spline function, $S(\lambda,d)$, by defining the chi-square as a function of the calibration dose, $\chi^2(d)$, as

$$\chi^2(d) = \sum_i \left(\frac{S(\lambda_i,d) - OD_u(\lambda_i)}{\sigma_u(\lambda_i)} \right)^2 , \tag{5.7}$$

where $\sigma_u(\lambda_i)$ is the standard deviation in the measurement of the $OD_u(\lambda_i)$. For convenience, the "bar" symbol, which denotes the filtering, on the optical density has been dropped. The dose that gives the minimum χ^2, i.e., the minimum difference between the $S(\lambda,d)$ and the $OD_u(\lambda)$ weighted by the $\sigma_u(\lambda)$, is the conversion dose.

5.2.3 χ^2 minimization

There are many minimization codes available. They can be roughly divided into two categories, local and global. Local minimizers are generally very robust, but users must provide a guess value near the local minimum. In theory, $\chi^2(d)$ should only have one minimum. But due to the noise of the film response, especially at low doses, there may be other local minima. Therefore, global minimizers are preferred in this case. The tradeoff is the longer amount of time they take to complete the run. The global minimizer used is Sigma, written by Aluffi-Pentini *et al.* (1988). It searches for the absolute minimum of a given function, which in this case is $\chi^2(d)$, and returns a value of the abscissa at the minimum ordinate.

5.2.3.1 Feasibility

To test the χ^2 minimization method, a set of films, irradiated by a ^{60}Co source with doses from 5 cGy to 100 Gy, was used. The *OD* as a function of λ (from 500 to 750 nm at a step size of 1 nm) and d was measured for all the films and spline fitted as described in Section 5.2.2. The spline fitted data would act as the calibration. Then a set of artificial $OD(\lambda)$ data was created by manipulating the calibration data in the following manner. To begin, a random value deviated with a Gaussian (Normal) distribution, in the form of

$$p(y)dy = \frac{1}{\sqrt{2\pi}} e^{y^2/2} dy , \tag{5.8}$$

was generated using a function code, Gasdev, obtained from Press *et al.* (1992 and references therein). Values generated by this method have a zero mean and a unit variance. Then for each λ, the generated value was multiplied by the standard deviation of the *OD*. The multiplied value was then added to the *OD* to create the new OD_n. The standard deviation of the OD_n is the same as that of the *OD*. Finally, the χ^2 between the OD_n and the spline fitted calibration data was calculated, and the minimum of χ^2 was determined as described earlier.

In theory, the minimum χ^2 would have a value equal to the degrees of freedom in the measurement. In this case, the degrees of freedom are 251 since λ is from 500 to 750 nm at the 1 nm step size. The error in estimating the dose, $\sigma(d)$, can be determined by varying d about the minimum such that χ^2 is increased by 1 from its minimum value (Bevington and Robinson 1992). If a parabola is fitted to three $\chi^2(d_i)$ points with evenly spaced d_i, where i = 1, 2, or 3, such that the minimum d is between d_1 and d_3, then the error in d, $\sigma(d)$, is given by

$$\sigma(d) = \Delta d_i \sqrt{2\left(\chi^2(d_1) - 2\chi^2(d_2) + \chi^2(d_3)\right)^{-1}}\,, \tag{5.9}$$

where Δd_i is the difference in d between adjacent dose points.

Original Dose (Gy)	Data Set 1			Data Set 2			Data Set 3		
	d (Gy)	$\sigma(d)$	χ^2	d (Gy)	$\sigma(d)$	χ^2	d (Gy)	$\sigma(d)$	χ^2
0.0508	0.0496	0.0008	255.3	0.0496	0.0008	247.5	0.0512	0.0008	251.2
0.1006	0.0995	0.0009	255.9	0.0995	0.0008	240.0	0.1011	0.0009	250.3
0.2501	0.2515	0.0053	255.2	0.2483	0.0053	247.4	0.2512	0.0063	251.4
0.4992	0.4957	0.0020	254.5	0.4962	0.0020	238.4	0.4998	0.0020	250.5
0.9975	0.9939	0.0039	254.5	0.9948	0.0039	247.0	1.0000	0.0039	251.0
2.4995	2.4978	0.0016	254.1	2.4978	0.0016	246.2	2.5005	0.0016	251.0
4.9981	4.9953	0.0027	256.5	4.9947	0.0026	239.0	4.9991	0.0027	250.5
10.003	9.999	0.003	256.0	9.999	0.003	239.7	10.005	0.003	250.2
25.001	24.997	0.004	256.3	24.998	0.004	239.9	25.004	0.004	250.2
50.001	49.998	0.003	254.3	50.000	0.003	247.3	50.004	0.003	250.9
100.003	99.994	0.008	254.1	100.009	0.008	247.5	100.008	0.008	251.4

Table 5.1 Test results on the χ^2 minimization method

Table 5.1 shows the results of the test on the χ^2 minimization method using the artificially created data. The first column is the original dose used for calibration. Three sets of artificial data were created. For each set, the three columns represent the dose calculated using the χ^2 minimization method, the uncertainty variation associated with the dose, and the χ^2 value in the evaluation, respectively. It appears that every calculated dose is within $2\sigma(d)$ of the original dose. In addition, the values of the χ^2 are all very close to the expected value of 251, which are the degrees of freedom in the artificial data. For all of the calculated doses, except at 5 cGy, their uncertainties are very small (< 1%) when compared to the dose values. This indicates that the uncertainties resulting from the χ^2 minimization method due to random error alone are, in most cases, negligible when taking into consideration other random and systematic errors, such as the film nonuniformity, the temperature, and the humidity, etc.

The above test was performed by manipulating the original calibration dose values. For completeness, a set of artificial $OD(\lambda)$ data was also created at a dose different than any of the original calibration doses. The dose of 35 Gy was arbitrarily chosen, and a set of $S(\lambda,35)$ was obtained from the interpolated spline of $OD(\lambda,d)$ of the calibration data. Then the artificial $OD(\lambda)$ was generated by applying the random Gaussian deviation method to $S(\lambda,35)$, as described before. Table 5.2 shows the results of 5 simulations. The dose values are all within the expected dose of 35 Gy, and the values of the χ^2 are consistent with those in Table 5.1.

Set	d (Gy)	$\sigma(d)$	χ^2
1	34.9982	0.0043	313.9
2	35.0017	0.0041	286.4
3	35.0021	0.0043	301.7
4	35.0061	0.0038	236.3
5	34.9976	0.0041	273.3

Table 5.2 Test results with expected $d = 35$ Gy

Figure 5.6 displays the χ^2 as a function of d graph using the set #2 simulated data. The $\chi^2(d)$ has been normalized to the expected degrees of freedom of 251. The graph demonstrates how the unknown dose and its uncertainty can be obtained graphically.

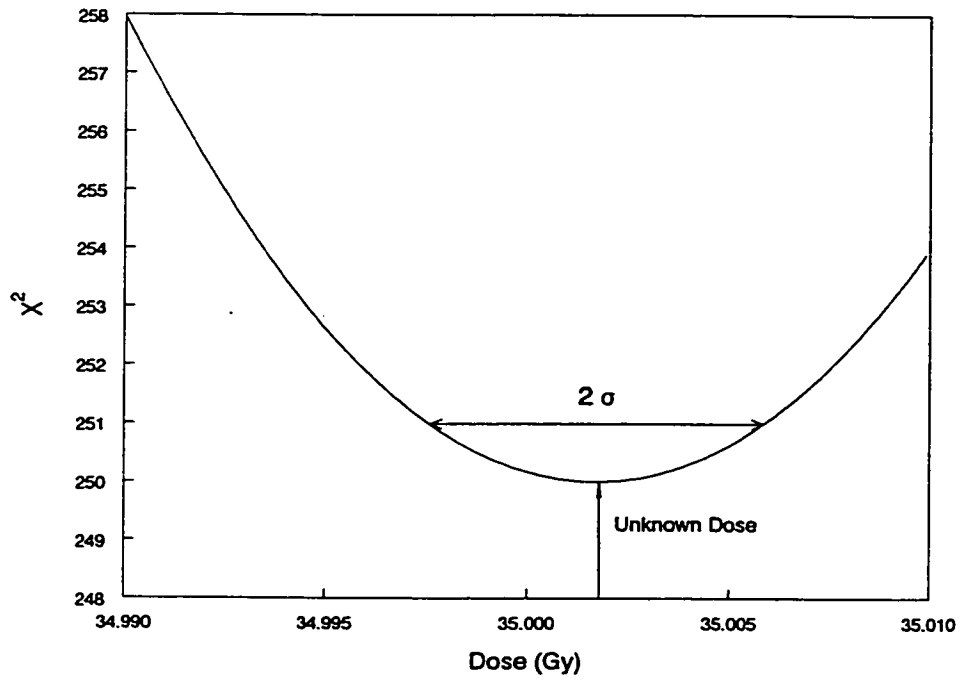

Figure 5.6 χ^2 as a function of dose

5.2.4 2-step process

It has been found that the χ^2 minimization over the full range of filtered $OD_u(\lambda)$ did not always return the best result, especially at the extreme low and high doses. The reason is that, at very low doses, the optical density has very small signal at wavelengths outside the major and minor peak regions. At very high doses, the intensity response is very weak at the major and minor peaks. Therefore, a significant amount of noise from these regions would be included if the χ^2 minimization is performed on all wavelengths.

To avoid these regions, an initial χ^2 search for the minimum dose was performed by limiting the wavelengths from 506 to 600 nm. The result of this search would determine the wavelengths used for the second, and more accurate, search. Table 5.3

below lists the range of wavelengths chosen for the second search, depending on the dose returned from the initial search. The range was chosen primarily to avoid the low signal-to-noise regions, and thus, increase the overall sensitivity in the measurements.

Dose Returned From Initial Search	Range of Wavelengths Used for the 2nd Search
$d_i < 1$ Gy	640 — 690 nm
50 Gy $\geq d_i \geq 1$ Gy	506 — 746 nm
50 Gy $< d_i$	506 — 600 nm

Table 5.3 Range of wavelengths for the 2nd search

5.3 Advantages

The interpolating-spline fitting and χ^2 minimization method (ISFCSMM) has a number of advantages over the FWM. 1) In the FWM, the nonlinearity of the calibration curve, $d(OD)$, limits the range of dose that can be measured to about 100 Gy if the wavelength is selected near the peaks. The increase of dose limit can be extended with decreasing wavelength. But this also results in a loss of sensitivity. Moreover, the selection of the wavelength to maximize the sensitivity depends on the dose, which is unknown. Therefore, a pre-determined wavelength may not be possible. However, the ISFCSMM can determine the dose at least higher than 220 Gy without, potentially, suffering a significant loss of sensitivity. The extension of the dose limit is possible because the χ^2 minimization determines the optimum dose using multiple wavelengths that are sensitive to a very wide range of doses. 2) The FWM is very susceptible to the thin-film interference noise because one cannot tell if the film response is on the crest or

the trough of the interference. The ISFCSMM drastically reduces this problem by filtering the noise using adjacent wavelengths. It also extends the lower dose limit to below 0.5 Gy. It should be mentioned that the filtering process worked very well in smoothing the spline fitted ^{60}Co calibration data. However, it might not work as well for all the experimental data in determining the unknown dose. It turns out that filtering the experimental data successfully is not as important because the χ^2 minimization method searches for the minimum value of χ^2. If the experimental data were very noisy, the ISFCSMM would still return a value very close to the correct dose, even though the minimum χ^2 might be much larger than the expected degrees of freedom. 3) The ISFCSMM obtains much more information than the FWM on the $OD(\lambda)$, and the information may be used to check for potential error in the dose determined. For example, if there is a scratch or a smudge on a spot of interest on the film, the χ^2 may become unusually large, and the $OD(\lambda)$ curve may appear very differently than is expected. Therefore, the dose obtained could be further analyzed or disregarded.

CHAPTER 6

RESULTS

In this chapter, the results from all the experiments carried out as described in Chapter 4 are presented in the following sections. The experiments involved irradiating films in a specific geometry by γ-rays, β particles, or electrons. The irradiated films were scanned at least 48 hours after irradiation by the MDIS. The output of the scans was recorded by a computer. The computer then generated a file listing the coordinates, wavelengths, transmitted intensities and their variances of all the points that were scanned.

6.1 ^{60}Co γ irradiation

The purpose of the ^{60}Co irradiation is to provide calibration for the radiochromic films. Before irradiation, the 12 films that were selected were individually pre-scanned with respect to their respective two reference films. Then they were irradiated by the ^{60}Co unit for various exposure times. A few days after the irradiation, they were scanned again with their respective reference films.

6.1.1 ^{60}Co irradiation results

Table 6.1 shows the data of the ^{60}Co irradiation. Column 1 is the assigned film number, and column 2 is the period of irradiation corrected by the source transit time.

The final column lists the actual dose, which was calculated by multiplying the period of exposure by a dose rate to water of 1.9334 Gy/min. This dose rate, already corrected to 22 °C and 1 atm, was measured directly by the technicians at the HRCC at the exact settings as the film irradiation. By measuring the optical density of each irradiated film, the optical density-to-dose calibration was established.

Film Number	Period of Irradiation (min)	Dose Deposited (Gy, ±1%)
1	115.12	222.57
2	75.08	145.16
3	38.04	73.55
4	20.02	38.71
5	10.02	19.37
6	5.02	9.71
7	2.52	4.87
8	1.52	2.94
9	0.52	1.01
10	0.35	0.68
11	0.17	0.33

Table 6.1 ^{60}Co irradiation results

6.1.2 Determining the optical density

The optical density of a film can be determined by measuring the transmitted intensity as a function of wavelength before and after the irradiation, as defined earlier in equation (5.1) in Section 5.1. However, experimentally, the equation of the optical density needs to be modified because the components of the MDIS were not stable, and the film response varied due to external factors such as those described earlier in Section 2.9. To minimize the instabilities, each film was scanned, along with two reference films

simultaneously, before and after the irradiation. Let the intensity transmission as a function of wavelength through the film before and after the irradiation be $I_\circ$ and I, respectively, and the transmission of the two reference films before and after the irradiation be I_{r1}, I_{r2} and I'_{r1}, I'_{r2}, respectively. Then the optical density as a function of wavelength was calculated by,

$$OD = \log\left(\frac{I_\circ}{\langle I_r\rangle} \times \frac{\langle I'_r\rangle}{I}\right), \tag{6.1}$$

where $\langle I_r\rangle = (I_{r1} + I_{r2})/2$, $\langle I'_r\rangle = (I'_{r1} + I'_{r2})/2$, and the uncertainty in the OD was calculated by,

$$\sigma(OD) = \frac{1}{\ln(10)}\sqrt{\left(\frac{\sigma(I_\circ)}{I_\circ}\right)^2 + \frac{\sigma(I_{r1})^2 + \sigma(I_{r2})^2}{(I_{r1} + I_{r2})^2} + \frac{\sigma(I'_{r1})^2 + \sigma(I'_{r2})^2}{(I'_{r1} + I'_{r2})^2} + \left(\frac{\sigma(I)}{I}\right)^2}, \tag{6.2}$$

where σ denotes the uncertainty. Since every film, including the reference films, was scanned at 10 different points on the film, the 10 resulting $OD(\lambda)$'s were averaged to obtain a higher precision.

As mentioned in the last chapter, the $OD(\lambda)$ curve needed to be smoothed in order to filter the noise due to the thin-film interference. The interference noise was filtered fairly successfully by averaging every 5 points over 8 nm. The smoothed optical density as a function of wavelength for each dose is shown in Figures 6.1a, b and c. Note that the uncertainty bars are too small to be shown in Figures 6.1a and b.

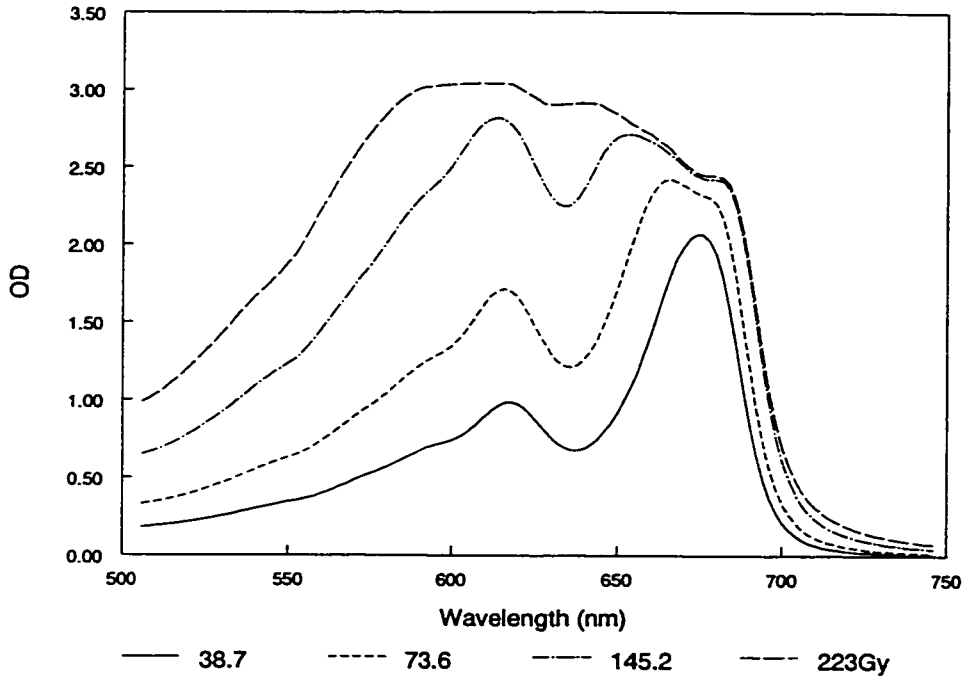

Figure 6.1a Smoothed $OD(\lambda)$ at high doses

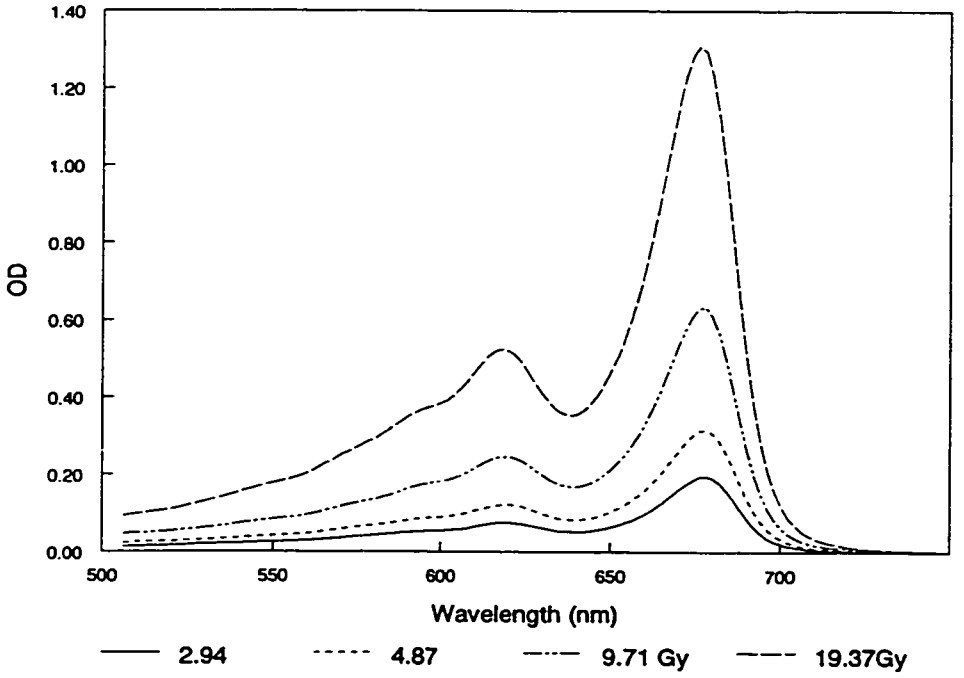

Figure 6.1b Smoothed $OD(\lambda)$ at medium doses

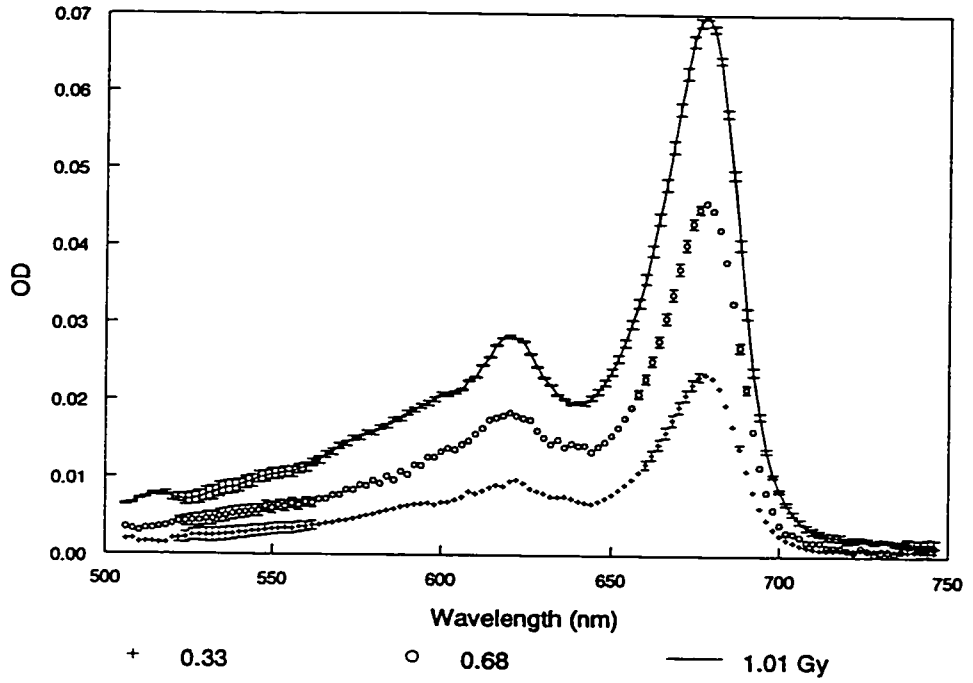

Figure 6.1c Smoothed $OD(\lambda)$ at low doses

6.2 Uniform ^{32}P β irradiation

The uniform ^{32}P irradiation experiment was designed to compare the expected β dose deposited in the films with the calculated dose determined from the ^{60}Co calibration so as to test the method described in Chapter 5. As in the case of the ^{60}Co irradiation, a set of 12 films was prepared, and each was scanned with its respective reference films before and after the ^{32}P irradiation. The irradiation experiment lasted for approximately two weeks, and all of the films were scanned at least 48 hours after the whole experiment was completed.

6.2.1 Expected dose

The films were irradiated by being placed in the ^{32}P irradiation facility such that one side of the film faced the "semi-infinte" ^{32}P solution, while the other side faced the "semi-infinite" Lucite block. Therefore, the dose on the surface of the film was determined based on this equilibrium geometry. In theory, the effective dose in water at the source-film boundary is half the equilibrium dose of the ^{32}P solution, and the dose on the film surface was calculated as follows. In chapter 4, equation (4.1) was used to calculate the activity concentration in the ^{32}P solution at the time of irradiation, $[A(t)]$. The dose rate in the source solution was determined by,

$$\dot{d}(t) = \frac{\overline{E}A(t)}{m} = \frac{\overline{E}}{\rho}[A(t)], \tag{6.3}$$

where $\overline{E}$ = 0.6949 MeV is the average energy of the ^{32}P beta spectrum, and ρ is the density of the solution, which is essentially water. Therefore, the dose rate at the boundary, $\dot{d}_b$, is half of $\dot{d}$. If the films were irradiated at the source boundary without any barrier, then the total dose received on the film surface, d_s, could be determined by,

$$\begin{aligned} d_s &= \int_0^{t_P} \dot{d}_b(t')dt' = \dot{d}_b(0)\int_0^{t_P} e^{-\frac{t'\ln(2)}{T}}dt' \\ &= \dot{d}_b(0)\frac{T}{\ln(2)}\left(1 - e^{-\frac{t_P\ln(2)}{T}}\right), \end{aligned} \tag{6.4}$$

where $\dot{d}_b(0)$ is the dose rate at the source boundary at the time of irradiation, t_P is the period of irradiation, and T is the half life of ^{32}P. However, the actual dose deposited in the film radiosensitive layers, the components that are responsible for the colour change

of the film post irradiation, must be corrected for the loss of dose due to the air gap in the ^{32}P container, the 2 Mylar sheets, and the film substrate in front of the radiosensitive layers. The correction was performed by manipulating Cross *et al.*'s (1992) Monte Carlo data that simulate depth dose distributions for various geometries and sources.

6.2.1.1 Cross' simulation

Cross *et al.* (1992) simulated the plane source kernel, K, (nGy·cm^2/Bq·h) as a function of depth z, by a uniform ^{32}P plane source with infinite lateral extent in water. However, the films were actually irradiated by a "semi-infinite" ^{32}P volume source. In order to make the dose correction possible, the plane source must be corrected to a "semi-infinite" volume source. Therefore, the dose at a given depth, $d(z)$, was calculated by taking the convolution between the plane source kernel, K, and the source density, $Y(z)$:

$$d(z) = \int_{-t}^{0} K(z - z')Y(z')dz', \tag{6.5}$$

where t is the thickness of the source. Since $Y(z')$ is constant, this equation can be simplified by a simple change of variable, resulting in,

$$d(z) = Y \int_{z}^{z+t} K(u)du. \tag{6.6}$$

For β dose much higher than the Bremsstrahlung dose, the above integral, to a good approximation, only needs to be integrated to the range of the β dose in the medium.

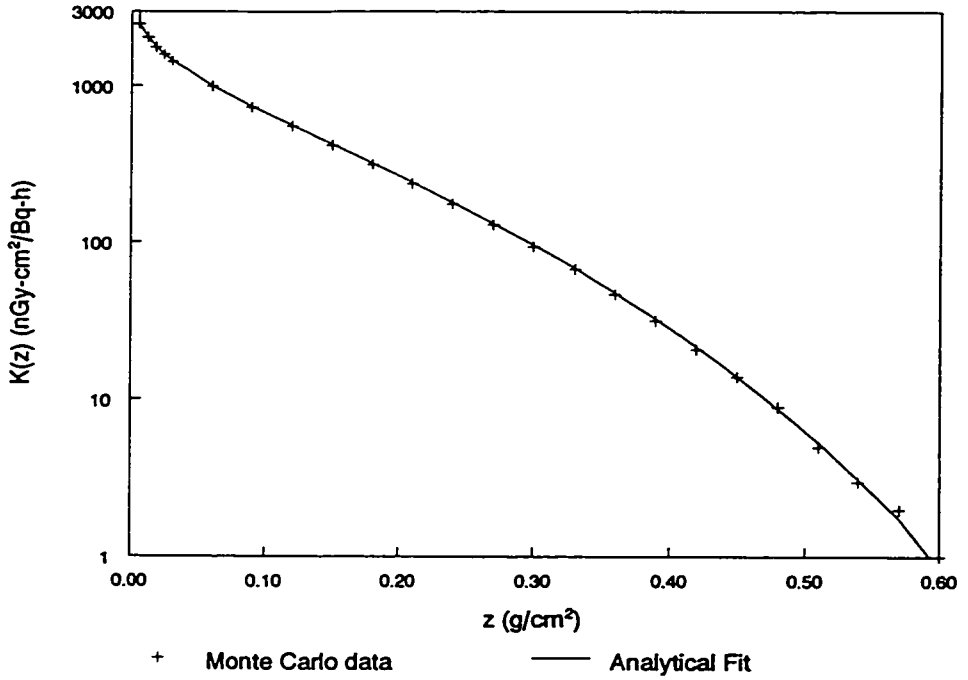

Figure 6.2 Analytical fit to Monte Carlo simulated $K(x)$

Due to the unrealistic nature of the plane source, the kernel at the source, $K(0)$, is infinity. Therefore, an analytical fit to the $K(z)$ is required before it can be integrated. A fitting function was chosen so that $K(z)$ goes to zero at the end of the β range, R, and at z near 0, $K(z)$ behaves as an exponential integral function, E_1. The fitting function is in the form of,

$$K(z) = a[E_1(\mu z) - E_1(\mu R)] + b\left(1 - \frac{z}{R}\right)^4, \tag{6.7}$$

where the ratio, a/b, and μ are free parameters, and

$$E_1(z) = \int_1^{\infty} \frac{e^{-xz}}{x} dx\,. \tag{6.8}$$

The parameter, a, is constrained so that the area of $K(z)$ is the average energy released. The E_1 function generally describes the dose point kernel at distance z for γ photons. But the main goal here is simply to find a suitable analytic function for the plane source kernel data so that its integral can be computed. Figure 6.2 displays the analytical fit to the $K(z)$ for ^{32}P in water, and Figure 6.3 shows the relative dose as a function of depth, $d(z)/d(0)$. The latter graph is the one used for the dose loss correction.

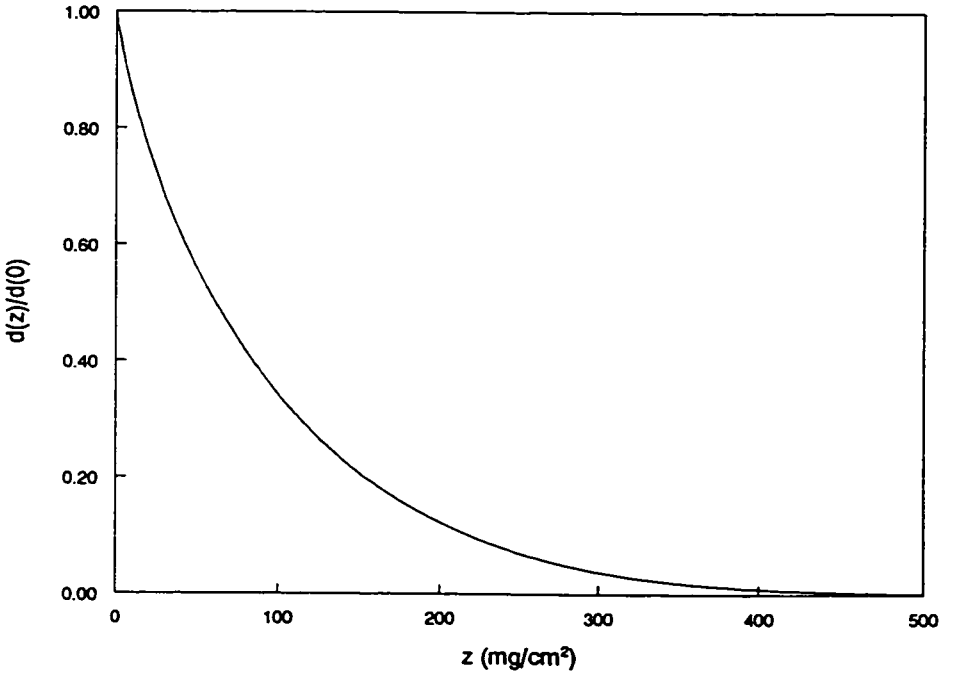

Figure 6.3 Relative depth dose distribution in water exposed to ^{32}P volume source

6.2.1.2 Air gap and Mylar area densities

Since the ^{32}P irradiation facility was designed to hold 100 mL of solution, and only 99 mL or less was transferred into the container, it is inevitable that there would be an air gap between the source boundary and the film. After the transfer of the ^{32}P

solution, the container was leveled. Unfortunately, the air gap appeared as a large bubble trapped in the middle of the container, and the gap thickness was not the same everywhere. However, from the dimensions of the container and the total volume transferred, it is possible to calculate the average thickness of the air gap. It was estimated that the horizontal width of the "bubble" was estimated to be about 35.56 mm wide. Therefore, from simple geometry, the average air gap was determined to be about 1.56 mm, or 0.188 mg/cm^2.

There were also two thin Mylar sheets between the source boundary and the film. One was used to protect the film from becoming contaminated, and the other was to prevent the source from evaporating. The area density was determined by weighing a large Mylar sheet. Then the weight was divided by the area of the sheet, yielding an area density of approximately 0.269 mg/cm^2.

6.2.1.3 Film substrate area density

The radiochromic films used in this and the ^{60}Co irradiation experiments were the GDM MD-55-2 type, lot # 37175. Klassen *et al.* (1997) did an extensive study on the components of the GDM, all with lot # 941206. They found that the GDM was made up of 7 layers with three different components. Niroomand-Rad *et al.* (1998) also obtained the components of the layers and their thickness through private communications with the manufacturer. Note that the paper does not mention the lot # of the films in presenting their data. Presumably, all of the double layered GDM films to date have the same nominal thickness and components. However, the measured thickness of the layers varies

slightly between the two studies, and their comparison is summarized in Table 6.2. The first column is the layer number such that layer 1 is the top layer of the film, and layer 7 is the bottom layer. Column 2 lists the components of the GDM as termed by Klassen *et al.* (left) and Niroomand-Rad *et al.* (right). The last two columns list the thickness of each layer as given by Klassen *et al.* and Niroomand-Rad *et al.*, respectively. It should be noted that the manufacturer's data sheet (Fairman 1998) supplied to us gives the nominal thickness of the radiosensitive gel/sensitive layers as 15 μm, while the overall nominal thickness of the film is 260 μm. An illustration of the various layers of the film is depicted in Figure 6.4. The layer number corresponds to that in the first column of Table 6.2.

Layer #	**Components (Klassen *et al.*/ Niroomand-Rad *et al.*)**	**Thickness (μm) by Klassen *et al.* (lot # 941206)**	**Thickness (μm) by Niroomand-Rad *et al.***
1	Mylar/Polyester base	66 ± 1	67
2	Radiosensitive gel/Sensitive layer	12 ± 2	15
3	Glue/Pressure sensitive adhesive	40 ± 2	44.5
4	Mylar/Polyester base	25 ± 1	25
5	Glue/Pressure sensitive adhesive	40 ± 2	44.5
6	Radiosensitive gel/Sensitive layer	12 ± 2	15
7	Mylar/Polyester base	66 ± 1	67
Overall	GDM	260 ± 1	278

Table 6.2 Thickness and components of GDM layers

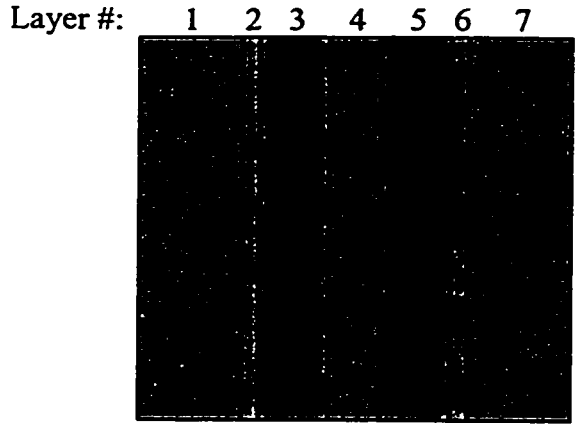

Figure 6.4 Schematic view of the GDM layers

From the Table above, the first radiosensitive layer of the film is behind the Mylar/polyester base layer, and the second radiosensitive layer is behind 5 layers. Therefore, to make the substrate correction possible, the area density of each component must be calculated. Unfortunately, of the 3 different components in the GDM, only the volume density of the Mylar/polyester base (1.4 g/cm^3) is known. Hence, the volume densities of the other 2 components are assumed to be about the same, so that their average volume density can be calculated from the thickness and the volume density of the entire film and the Mylar/polyester base layer. The area density of an uncut film was measured to be about 32.9 mg/cm^2. Using the film's physical thickness, the volume density was calculated. Table 6.3 shows the calculated results of the volume and area densities for each layer, based on the data given by Klassen *et al.* and Niroomand-Rad *et al.*

Layer #	Klassen *et al.*		Niroomand-Rad *et al.*	
	Volume Density (g/cm^3)	Area Density (mg/cm^2)	Volume Density (g/cm^3)	Area Density (mg/cm^2)
1	1.4	9.24 ± 0.14	1.4	9.38
2	1.052 ± 0.067	1.27 ± 0.23	0.895	1.34
3		4.21 ± 0.34		3.99
4	1.4	3.50 ± 0.14	1.4	3.50
5	1.052 ± 0.067	4.21 ± 0.34	0.895	3.99
6		1.27 ± 0.23		1.34
7	1.4	9.24 ± 0.14	1.4	9.38
Overall	1.266 ± 0.005	32.9	1.184	32.9

Table 6.3 Calculated volume and area densities for each GDM layer

6.2.2 Correction to the expected dose

The graph of the relative dose as a function of depth in Figure 6.3 was used in the correction to the absorption of dose in various media. Cross *et al.* (1992) have shown that the depth dose curve is relatively insensitive to the medium in which the dose is deposited as long as the depth is expressed as area density. Thus, the area densities of various media that the β particles have to travel before depositing their energy in the radiosensitive layers of the film were added without correction. Note that there is self absorption in the radiosensitive layer itself. Therefore, since the layer is fairly thin, to a good approximation, the amount of self absorption is assumed to be equal to that by half the layer thickness. In summary, the sum of the area densities of various media in front of the first radiosensitive layer, x_{sum1}, is,

$$x_{sum1} = x_a + 2x_m + x_1 + \frac{1}{2}x_2, \tag{6.9}$$

where x_a and x_m are the area densities of the air gap and the Mylar sheet, respectively, and the subscripts of 1 and 2 denote the layer number as assigned in Table 6.2 and 6.3. The sum of the area densities in front of the second layer, x_{sum2}, is,

$$x_{sum2} = x_a + 2x_m + x_1 + 1\frac{1}{2}x_2 + 2x_3 + x_4 . \qquad (6.10)$$

Note that $x_2 = x_6$, and $x_3 = x_5$. From the data calculated from Klassen *et al.*, it was found that x_{sum1} = 10.60 ± 0.18 mg/cm^2 and x_{sum2} = 23.78 ± 0.84 mg/cm^2. The area densities correspond to a fraction of dose loss (see Figure 6.3) of 14.61 ± 0.19% and 26.71 ± 0.65%, respectively, resulting in an average loss of 20.66 ± 0.48%. From Niroomand-Rad *et al.*, x_{sum1} = 10.78 mg/cm^2 and x_{sum2} = 23.59 mg/cm^2, giving an average loss of absorbed dose of 20.68%, which agrees with the percentage loss in dose in the Klassen *et al.*'s case.

Table 6.4 lists the results of the dose correction. The first column is the assigned film number. Column 2 is the activity at the time of irradiation. The activity was calculated from equation (4.1) after diluted samples from the solution in the ^{32}P container were taken before the irradiation and twice after the irradiation. It was found that the count rates obtained from the liquid scintillation counter were constant to within 1σ, indicating there was no significant evaporation loss in the duration of the experiment. The third column is the dose rate at the source boundary through the use of equation (6.3), and the fourth column is the period of irradiation. Column 5 shows the calculated value of the dose at the surface of the film (see equation (6.4)) without the correction for

dose absorption in the various media, while the final column lists the dose values deposited in the films with the correction.

Film Number	$A(0)$ (GBq)	$\dot{d}_b$ (Gy/d)	t_P (d)	d_s (Gy)	Corrected Dose in Film (Gy)
1	1.1516	55.314	5.549	269.01	213.41 ± 1.48
2	0.8792	42.229	3.936	151.29	120.02 ± 0.83
3	0.7260	34.873	2.260	74.64	59.21 ± 0.41
4	0.6505	31.243	1.230	37.30	29.59 ± 0.21
5	0.6126	29.427	0.665	19.26	15.28 ± 0.11
6	0.5831	28.006	0.360	9.995	7.929 ± 0.055
7	0.5931	28.489	0.175	4.964	3.938 ± 0.027
8	0.5880	28.245	0.088	2.480	1.968 ± 0.014
9	0.5855	28.121	0.045	1.264	1.003 ± 0.007
10	0.5841	28.057	0.0225	0.631	0.501 ± 0.003
11	0.5835	28.024	0.0111	0.311	0.247 ± 0.002

Table 6.4 Expected ^{32}P uniform dose deposited in films

6.2.3 Measured dose

The ^{32}P irradiated films were scanned along with their respective reference films in the same manner as those irradiated by the ^{60}Co source. The optical densities and their uncertainties were calculated from equations (6.1) and (6.2) for all 10 scans on every film. Then each $OD(\lambda)$ was smoothed to filter the noise from the thin-film interference. However, instead of averaging the $OD(\lambda)$'s from the 10 scans that were made, each $OD(\lambda)$ was used to obtain the calculated dose from the ^{60}Co calibration using the interpolating-spline fitting and χ^2 minimization method (see Chapter 5). The resulting doses were then averaged to acquire the standard deviation in the average dose deposited

in the film. Table 6.5 shows the measured dose obtained from the ^{60}Co calibration (column 2) and the comparison with the expected dose from the ^{32}P counting (column 3), mentioned in the last section.

Film Number	Measured Dose (Gy)	Expected Dose (Gy)
1	212.01 ± 0.64	213.41 ± 1.48
2	114.87 ± 0.09	120.02 ± 0.83
3	59.12 ± 0.23	59.21 ± 0.41
4	29.43 ± 0.05	29.59 ± 0.21
5	15.06 ± 0.07	15.28 ± 0.11
6	8.06 ± 0.06	7.929 ± 0.055
7	4.19 ± 0.01	3.938 ± 0.027
8	2.06 ± 0.04	1.968 ± 0.014
9	1.01 ± 0.03	1.003 ± 0.007
10	0.510 ± 0.006	0.501 ± 0.003
11	0.194 ± 0.012	0.247 ± 0.002

Table 6.5 Comparison between measured and expected doses

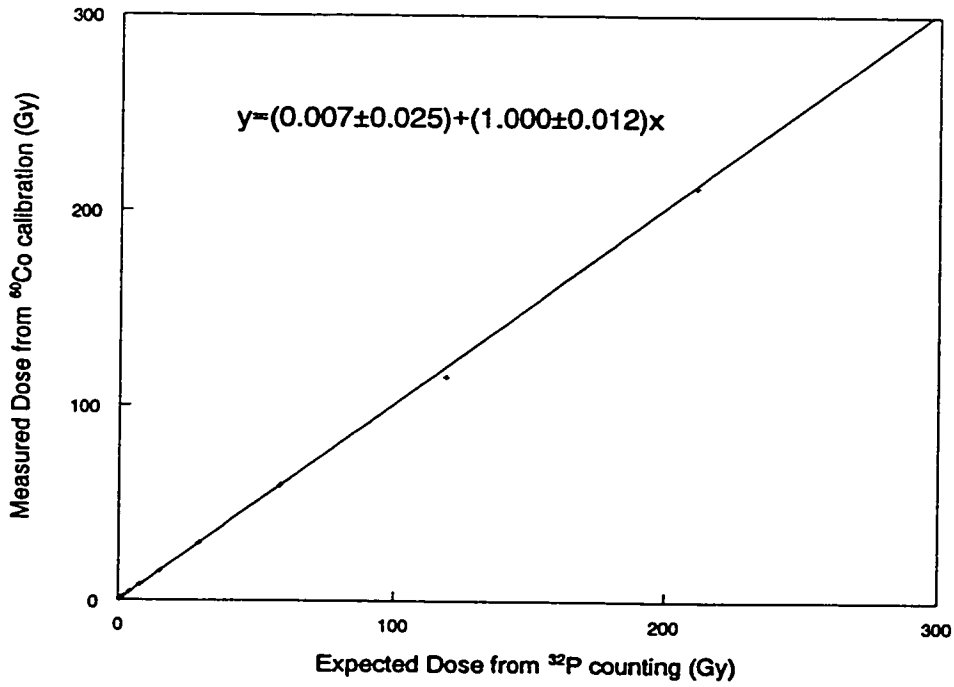

Figure 6.5a Plot of measured dose against expected dose

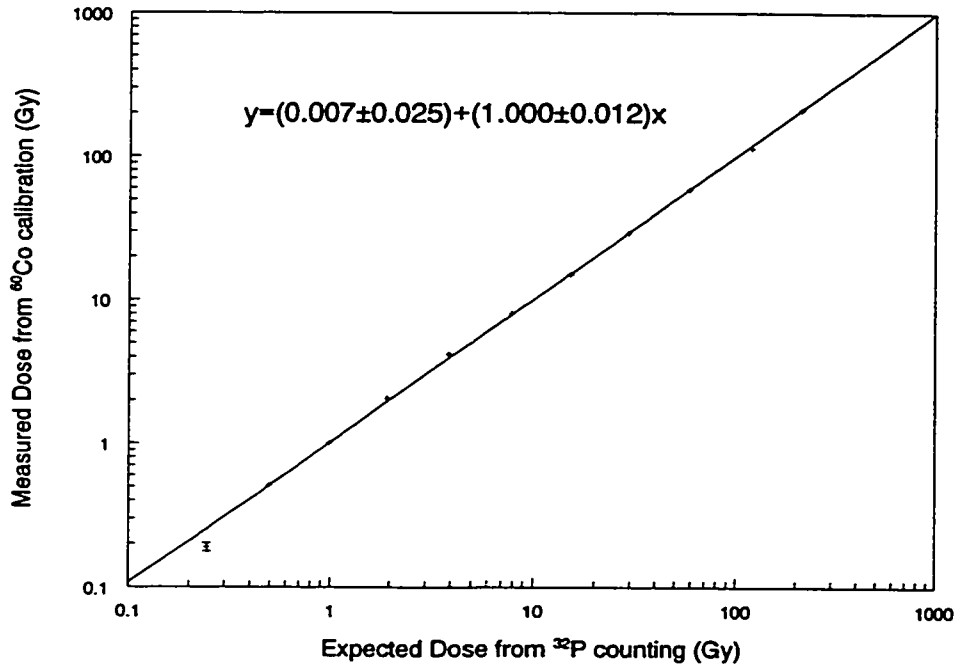

Figure 6.5b Log-log plot of measured dose against expected dose

The measured and expected dose comparison can be expressed graphically. Figure 6.5a displays a plot between the doses, and Figure 6.5b shows the log-log plot of the same graph. The data points on the graphs were fitted with a straight line by a linear regression weighted by a weighting factor, which was taken to be the inverse square root of the sum of the square of the uncertainties in the measured and expected doses. The coefficient of determination, R^2, of the fit was determined to be 0.999997, and the equation of the fitted line is,

$$d_M = (1.000 \pm 0.012) d_E + (0.007 \pm 0.025), \qquad (6.11)$$

where d_M and d_E are the measured and expected doses, respectively. The chi-square of the fit was calculated to be approximately 147.7, much greater than the degrees of freedom of 10. This indicates the probability of the data corresponding to the straight line

model is almost 100%, and the random fluctuations of the fit are larger than the experimental uncertainties. The fitted slope of the equation is essentially 1, and the fitted intercept is insignificant, indicating that the measured dose agrees with the expected dose.

6.3 Edge-on ^{32}P β irradiation

The irradiation to a film edge-on to the ^{32}P volume source was performed to determine the depth dose distribution of β particles in a Lucite block. This experiment was carried out twice. The first time was done immediately after the uniform ^{32}P β irradiation experiment while the source was still fairly active. The activity of the source at the time of the edge-on irradiation was determined to be 0.5615 ± 0.0019 GBq, by counting the samples retrieved from the ^{32}P container before and after the irradiation. The second time was done with a fresh source, and the activity of the source was determined, in a similar fashion as before, to be 0.8086 ± 0.0016 GBq. The determination of the activities enabled an estimate of the edge dose of the film to be about 270 Gy in the first trial and 400 Gy in the second.

6.3.1 Determining the optical density

In the first trial, the optical density of the irradiated film was determined similarly as in the uniform β irradiation experiment, except that an extra scan was required in this case to obtain the depth dose profile on the film. The extra scan was on the irradiated film in the y direction to measure the intensity as a function of depth, $I''(y)$. Therefore,

the optical density as a function of depth (wavelength dependence is implicit) was determined by,

$$OD(y) = \log\left(\frac{I_{\circ}(y_{\circ})}{\langle I_r \rangle} \times \frac{\langle I_r' \rangle}{I(y_{\circ})} \times \frac{I''(y_{\circ})}{I''(y)}\right) \tag{6.12}$$

where $y_{\circ}$ is a reference point that was scanned on the irradiated film before and after the irradiation, and the other variables have the same definitions as in equation (6.1). The uncertainty in the $OD(y)$ has two more terms from the relative uncertainties in $I''(y)$ and $I''(y_{\circ})$ in the square root than in equation (6.2). The irradiated film was scanned in this way 9 more times at different x coordinates so that the $OD(\lambda,x,y)$ was determined.

The optical density in the second trial was originally determined in the same way as the first. However, it was found that the $OD(\lambda)$ in the region at a distance greater than the β range of about 7.1 mm in Lucite had negative values at all wavelengths. Therefore, the $OD(\lambda,x,y)$ was determined relative only to points with the highest intensity transmission in this region, without employing any points on the reference films. The rationale of this treatment of data and the speculation of the cause of this anomaly will be discussed in the next chapter.

6.3.2 Determining the depth dose distribution

The $OD(\lambda,x,y)$ from the two irradiated films was smoothed and then converted to dose, $d(x,z)$, using the ^{60}Co calibration. Note the change of nomenclature of depth from y to z when describing dose. This is because the variable y is generally used to describe the

scan direction, while z is commonly preferred to indicate depth. Then the depth dose distribution, $d(z)$, was obtained by averaging the scans at the 10 different x coordinates to achieve higher precision, since $d(z)$ is supposed to be constant in x. The uncertainty in $d(z)$ is assumed to be the standard deviation in the mean value of $d(z)$. Figure 6.6 illustrates the depth dose distribution of β dose in Lucite from the first trial, while Figure 6.7 displays the distribution from the second. Note that the uncertainties in the depth were estimated by how well the position of the front edge of the film ($y = 0$) could be aligned horizontally as viewed in the MSP. These two distributions will be compared with the Monte Carlo simulation in the next chapter.

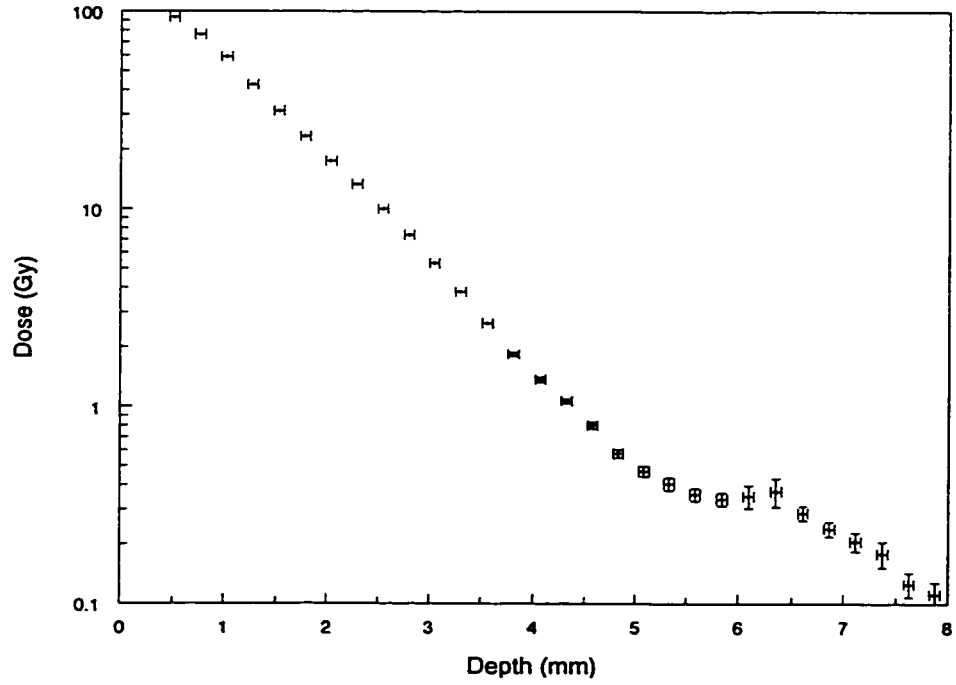

Figure 6.6 Depth dose distribution of β dose in Lucite (1st trial)

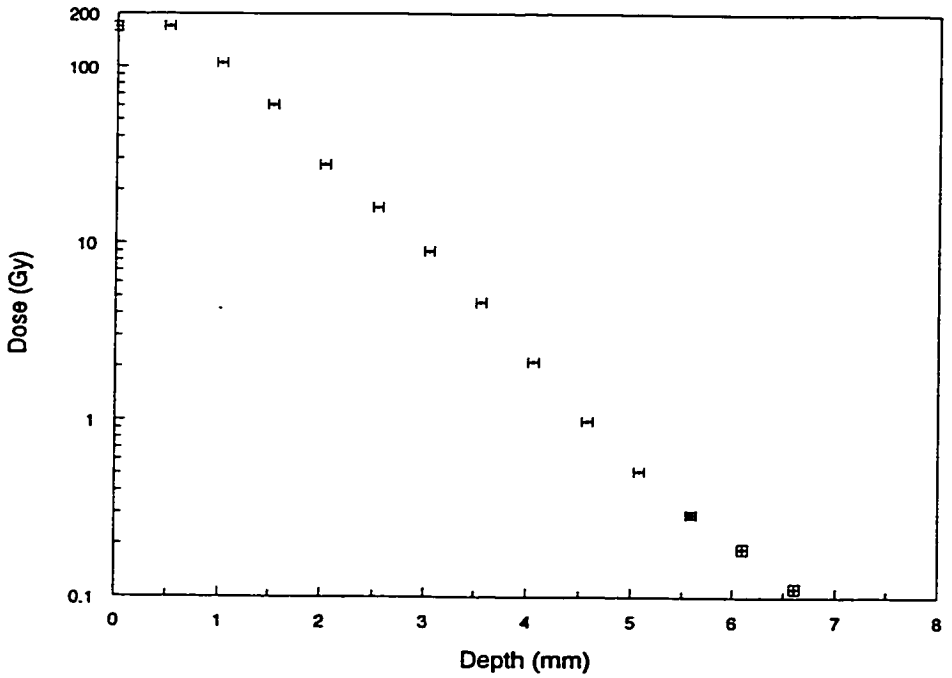

Figure 6.7 Depth dose distribution of β dose in Lucite (2^{nd} trial)

6.4 Edge-on 10 MeV electron beam irradiation

The edge-on irradiation by a 10 MeV electron beam was performed to examine the dose distribution of high energy electrons in a Lucite phantom. Three films were irradiated separately for 640, 50, and 5 s. These films will be referred to as films 1, 2 and 3, with film 1 having the longest exposure and film 3 the shortest. In the following subsections, the determination of the dose distribution in the films will be described. Then the background subtraction from the dose distribution follows. Since film 1 has higher entrance dose deposited than the largest calibrated dose, and film 3 has problems with low sensitivity in the regions away from beam entrance, all 3 films were used to reconstruct the dose distribution.

6.4.1 Determining the dose distribution

The optical density of the films was determined in a similar way as in the ^{32}P edge-on irradiation. The difference is that no reference films were employed in this case. For a horizontal scan at a fixed y, the $OD(x)$ was determined by,

$$OD(x) = \log\left(\frac{I_b}{I(x_r)} \times \frac{I'(x_r)}{I'(x)}\right), \tag{6.13}$$

where $I'(x)$ is the intensity transmission at a point in the horizontal scan, $I'(x_r)$ is the intensity of a reference point during the scan, $I(x_r)$ is the intensity of the same reference point in a separate scan with a blank region with transmission intensity of I_b. For films 1 and 2, the blank region was found near the far corners of the film. But for film 3, there was no noticeable difference in optical density between the regions near the front or far edge.

The horizontal scans were repeated for different depths to obtain the $OD(x,y)$. McLaughlin *et al.* (1991) have found that the energy dependence of the GDM on optical density was minimal between ^{60}Co gamma radiation and 10 MeV electrons. Therefore, the ^{60}Co calibration was used to convert the optical density into dose as a function of horizontal distance and depth, $d(x,z)$. It should be pointed out for $z < 14$ mm, the peak dose deposited in film 1 was larger than the highest calibrated dose. Thus, there were no data available in the peak area for film 1 near the front edge.

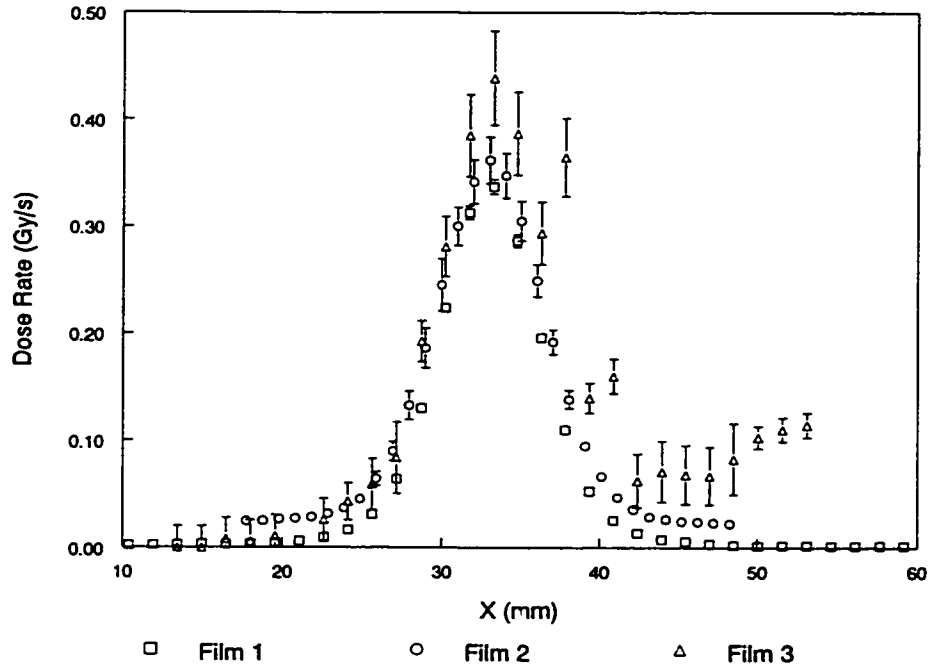

Figure 6.8 Dose rate as a function of lateral distance at $z = 14$ mm

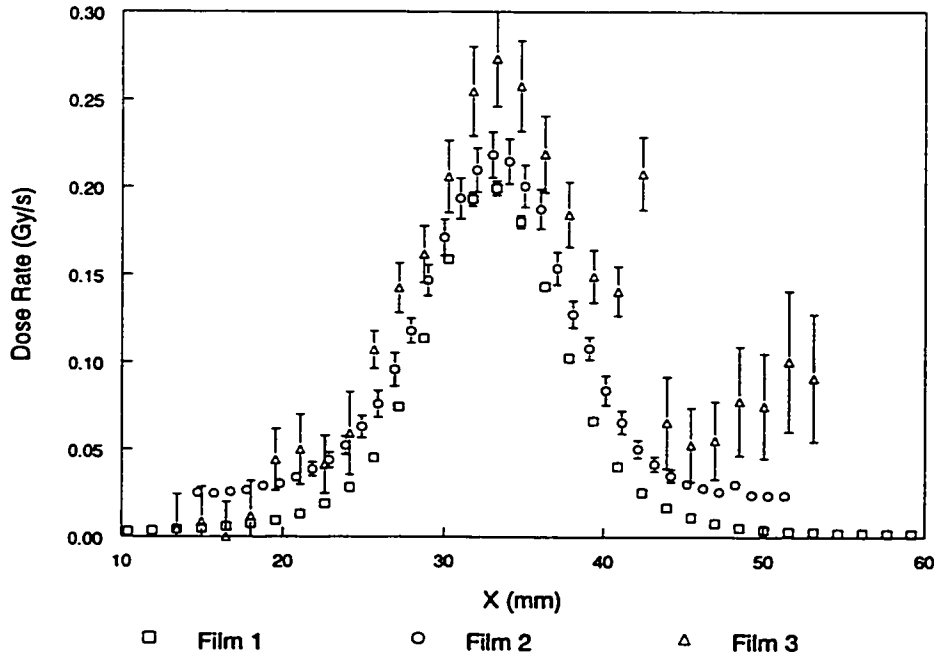

Figure 6.9 Dose rate as a function of lateral distance at $z = 19$ mm

Figures 6.8 and 6.9 compare the dose rate of the three irradiated films at approximately $z = 14$ and 19 mm, respectively. Note that the three curves on each graph were slightly shifted in x so that their centroids would appear to coincide with one another. The dose rate was calculated by dividing the actual dose received by the films by their respective exposure times. The uncertainties of the experimental data were difficult to estimate since, unlike the ^{32}P edge-on irradiation, the $OD(x,y)$ is not constant in either x or y. In addition, the interpolating-spline fitting and χ^2 minimization method returns a fitting uncertainty that represents only a small fraction of the total uncertainty in dose. However, the uncertainties of the measured dose listed in Table 6.5 can be used as a rough estimate of the uncertainties here. Note that the listed uncertainties are actually the uncertainties in the mean value of dose. Therefore, they must be multiplied by $\sqrt{10}$ to obtain the uncertainties in the population. Since the uncertainties are dominated by the standard deviation in the film uniformity, and the films used in this experiment are more nonuniform than those used in other experiments, it can be assumed that the uncertainties in this experiment are larger than the others by a scaling factor between their film uniformity variances. It was determined that this scaling factor was approximately 2 (see Section 3.6).

6.4.2 Background correction

The graphs presented in Figures 6.8 and 6.9 demonstrate that the three curves do not match exactly as would be expected. One of the obvious reasons is that there is a

background in the films, and this should be subtracted. In particular, film 3 seems to display a linear background with a nonzero slope, which is not expected based on the symmetry of the beam spread. Before the background could be subtracted, all the $d(x)$ curves were first fitted with analytical functions to find out their characteristics.

6.4.2.1 Fitting dose distributions

The spread of every $d(x)$ curve appears to behave similar to a Gaussian distribution, but not near the peak or the tails (bases) of the curve. Nevertheless, the Gaussian distribution fit can provide information on the centroid, peak width, peak height, and the background. Due to the fact that the dose curves appear to be on a linear slope for the film 3 data, the Gaussian distribution was modified to include a linear background. The equation used for the fitting is,

$$d_{fit}(x) = a_1 + a_2 x + a_3 e^{\frac{-(x-a_4)^2}{2a_5^2}}, \tag{6.14}$$

where a_i's are the fitting parameters. In particular, a_1 and a_2 fit the intercept and slope of the background, respectively. a_3 fits the height of the peak above the background. a_4 represents the position of the centroid, and a_5 is the standard deviation of the distribution.

The $d(x)$ curves were all fitted with the equation above. A typical fitting result at z = 19 mm is listed in Table 6.6 and is illustrated graphically in Figure 6.10. It should be mentioned that the weighting factors, i.e. the inverse variances, of the dose distribution of film 1, $d_1(x)$, had to be adjusted slightly to improve the fitting to the peak.

Film Number	1	2	3
a_1 (Gy/s)	0.005 ± 0.001	0.027 ± 0.001	-0.020 ± 0.018
a_2 (Gy/s/mm)	-(0 ± 3) × 10^{-5}	-(6.3 ± 2.4) × 10^{-5}	0.0018 ± 0.0006
a_3 (Gy/s)	0.192 ± 0.002	0.188 ± 0.002	0.206 ± 0.016
a_4 (mm)	33.04 ± 0.04	33.18 ± 0.05	33.44 ± 0.37
a_5 (mm)	4.21 ± 0.05	4.58 ± 0.05	5.55 ± 0.51
R^2	0.998	0.999	0.913

Table 6.6 Fitting results of the dose rate distribution at z = 19 mm

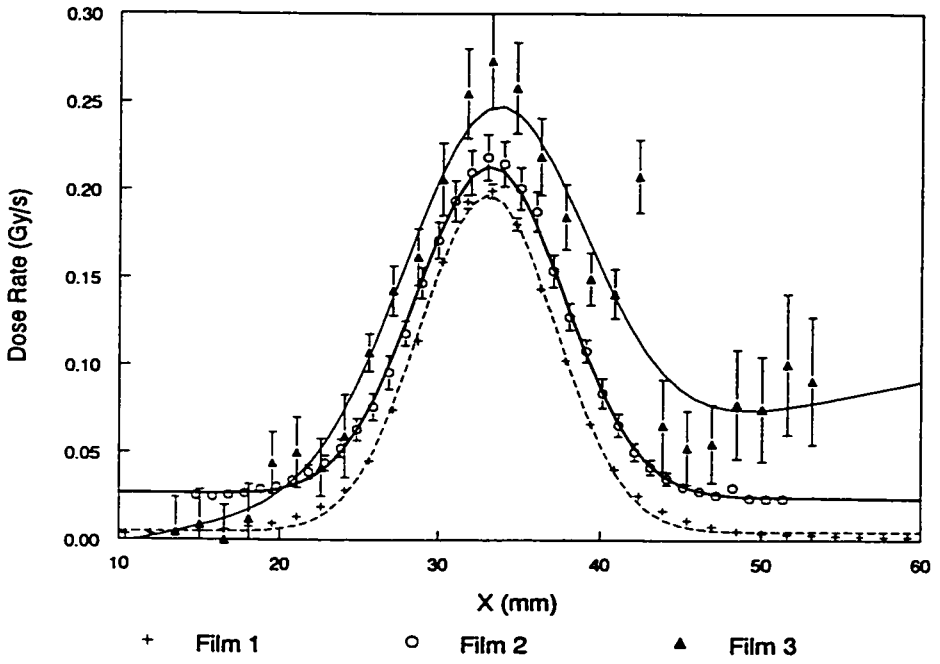

Figure 6.10 Fitted dose rate distribution at z = 19 mm

6.4.2.2 Determining the centroid position

The background removal and the reconstruction of the $d(x)$ curves require the centroids of all three films to line up. Therefore, it is necessary to examine the position of the centroids at a function of depth. Figure 6.11 displays this relationship for all three films. It should be noted that for each film, the centroid positions obtained from the modified Gaussian distribution fit are plotted relative to the centroid position closest to

the film front edge. All three graphs show deviation of the centroid position from the beam axis at increasing depth. It should be pointed out that this deviation is not observed in film 1 or 3 if the maximum dose position were used as the "centroid".

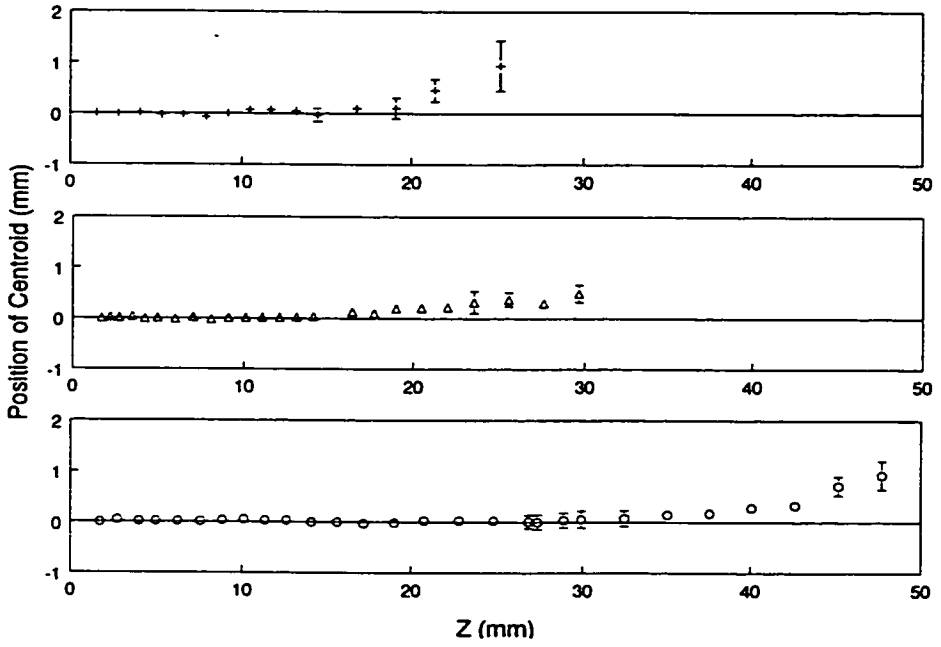

Figure 6.11 Centroid position as a function of depth for films 1 (bottom), 2 (middle), and 3 (top)

6.4.2.3 Background removal

Since the centroid positions vary with depth, every $d(x)$ curve was shifted so that its centroid would be at $x = 0$. This shifting was accomplished by $d(x - a_4(z))$ to generate the shifted $d(x')$ at every z. Although the origin of the background is not known, it appears that the background dose in film 1, as roughly determined by examining the bases of the $d(x)$, is approximately the same as that of film 2 at various depths. Therefore, at each depth, the $d(x')$ is assumed to be in the following form,

$$d(x') = \dot{d}(x')t + c(x'), \tag{6.15}$$

where $\dot{d}(x')$ is the dose rate, t is the time of exposure, and $c(x')$ is the background. Unfortunately, film 3 appears to have a background on a nonzero slope, while the other films do not. Since, in theory, $d(x')$ should be symmetric, in order to reduce the effect of this sloping background and improve the sensitivity in $d(x')$, the curves were "folded" over the centroid by averaging the dose on each side of the centroid. This is illustrated by,

$$\overline{d}(x') = \frac{d(-x') + d(x')}{2}. \tag{6.16}$$

Now, the background, $c(x')$, at a given z can be computed by using equation (6.15) on the dose distributions $\overline{d}_1(x', z)$, $\overline{d}_2(x', z)$, and $\overline{d}_3(x', z)$, where the subscripts denote the film number. First, each curve was fitted by a 2-d interpolating bicubic spline so as to generate a set of dose distributions at fixed x_i and z_j values for all three films. Then solving equation (6.15) for $\overline{d}_1(x_i', z_j)$ and $\overline{d}_2(x_i' z_j)$, the background was determined to be,

$$c_{12}(x_i', z_j) = \frac{\overline{d}_2(x_i', z_j)t_1 - \overline{d}_1(x_i', z_j)t_2}{t_1 - t_2}, \tag{6.17}$$

and the dose rate is,

$$\dot{d}_{12}(x_i', z_j) = \frac{\overline{d}_1(x_i', z_j) - \overline{d}_2(x_i', z_j)}{t_1 - t_2}. \tag{6.18}$$

Equation (6.15) was also solved for $\bar{d}_2(x_i', z_j)$ and $\bar{d}_3(x_i', z_j)$ to determine the background, $c_{23}(x_i', z_j)$, and the dose rate, $\dot{d}_{23}(x_i', z_j)$. The combined $\dot{d}_{12}(x', z)$ and $\dot{d}_{23}(x', z)$ were used to reconstruct the dose distribution.

6.4.3 Dose distribution reconstruction

Since film 3 had the least amount of exposure, it suffers from low signal-to-noise problems in regions away from the beam entrance. Therefore, the $\dot{d}_{23}(x', z)$ curve is only good for small x' and z. In contrast, the entrance dose in film 1 was larger than the highest calibrated dose. So the $\dot{d}_{12}(x', z)$ curve is only good for the tail of the curve or z larger than 14 mm. Figure 6.12 shows the dose rate distributions, $\dot{d}_{12}(x', z)$ (circles) and $\dot{d}_{23}(x', z)$ (triangles), at z = 1.7078 mm. Note that the dose rate has been converted to dose per electron, after divided by the beam current. In this example, the dose distribution was reconstructed by taking the first 10 points of the $\dot{d}_{23}(x', z)$ curve, and the rest from the $\dot{d}_{12}(x', z)$ curve, which does not have the right dose for $x' < 2.5$ mm.

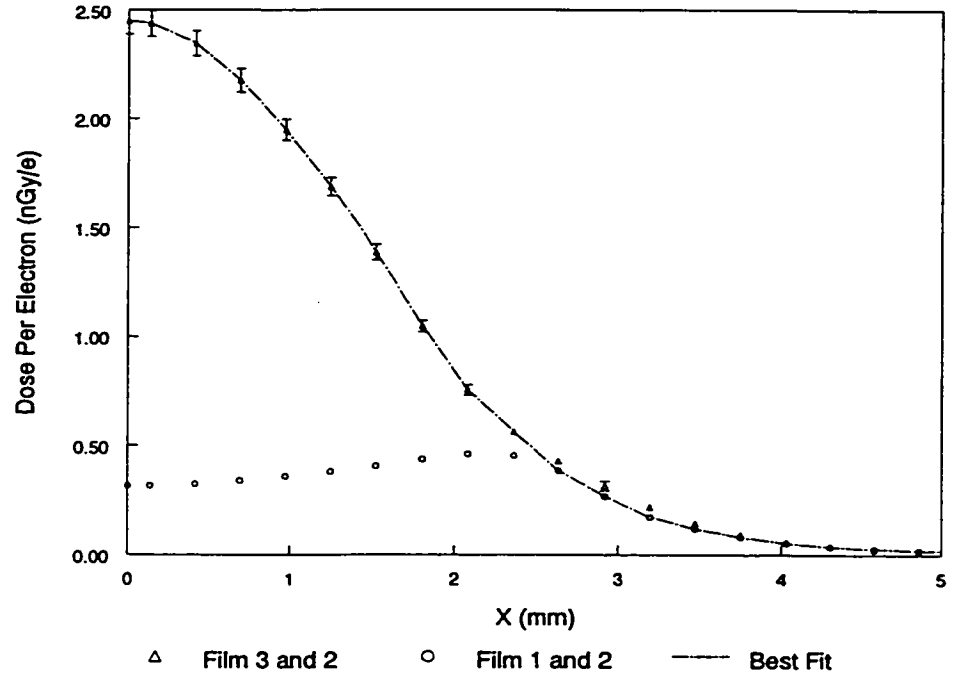

Figure 6.12 Dose reconstruction at $z = 1.7078$ mm

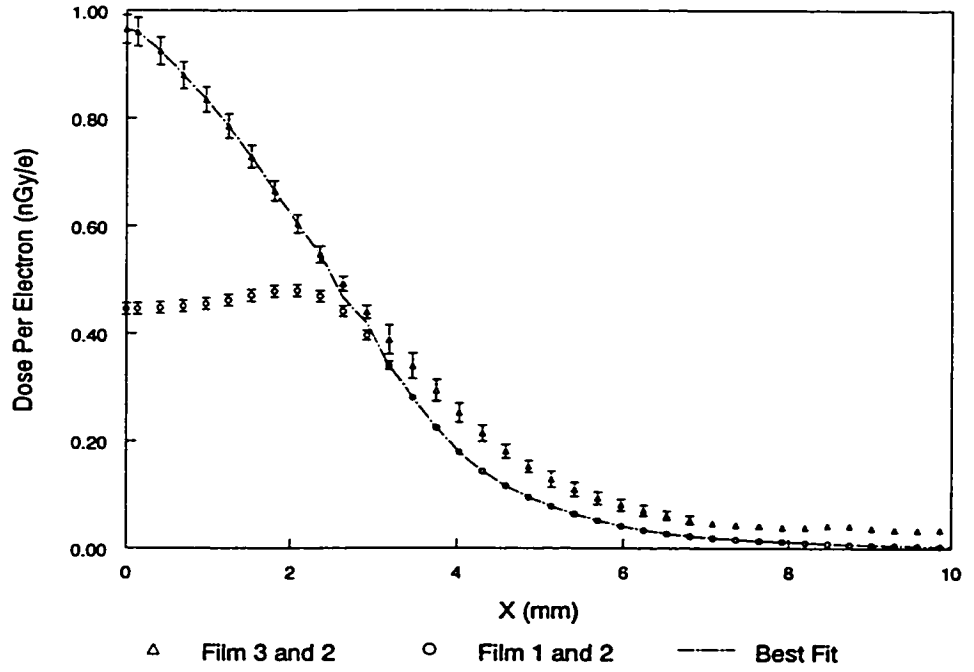

Figure 6.13 Dose reconstruction at $z = 9.0738$ mm

In the case where the $\dot{d}_{23}(x',z)$ curve does not meet the $\dot{d}_{12}(x',z)$ curve, the discontinuity between the closest points of the two curves was joined by averaging the points at or near the discontinuity. This method is illustrated by Figure 6.13 ($z = 9.0738$ mm), where the 2 dose values from both curves were averaged at the 11^{th} and 12^{th} points to produce a continuous distribution, $\dot{d}(x',z)$. For the dose distribution beyond $z = 14$ mm, only the $\dot{d}_{12}(x',z)$ curve was used since the peak dose of $\dot{d}_{23}(x',z)$ has very poor sensitivity.

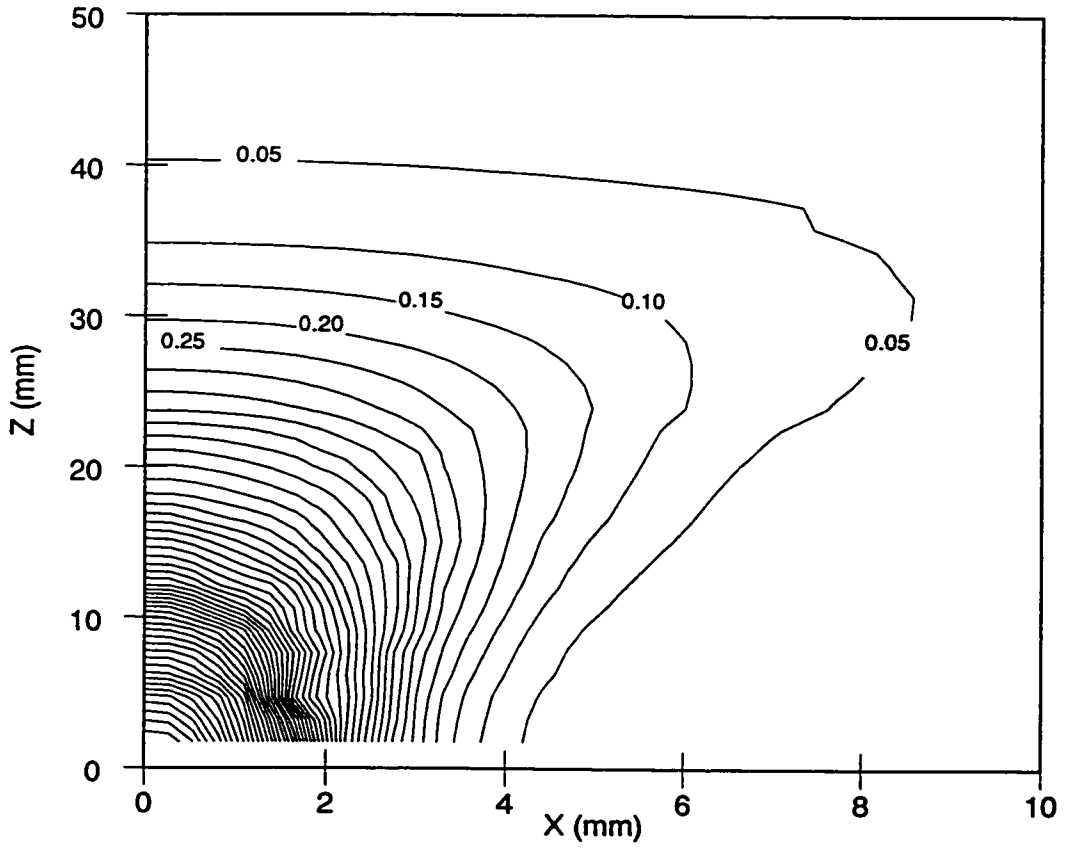

Figure 6.14 Contour plot of reconstructed dose distribution.

Figures 6.14 displays a contour plot of the reconstructed $\dot{d}(x',z)$. In the plot, 48 contour lines are drawn from 0.05 nGy/e to 2.40 nGy/e, with each successive contour representing a change of 0.05 nGy/e. The $\dot{d}(x',z)$ is also shown in a 3-d log mesh plot, illustrated in Figure 6.15. Individual $\dot{d}(x')$ at various depths will be displayed and compared with Monte Carlo simulation results in the next chapter.

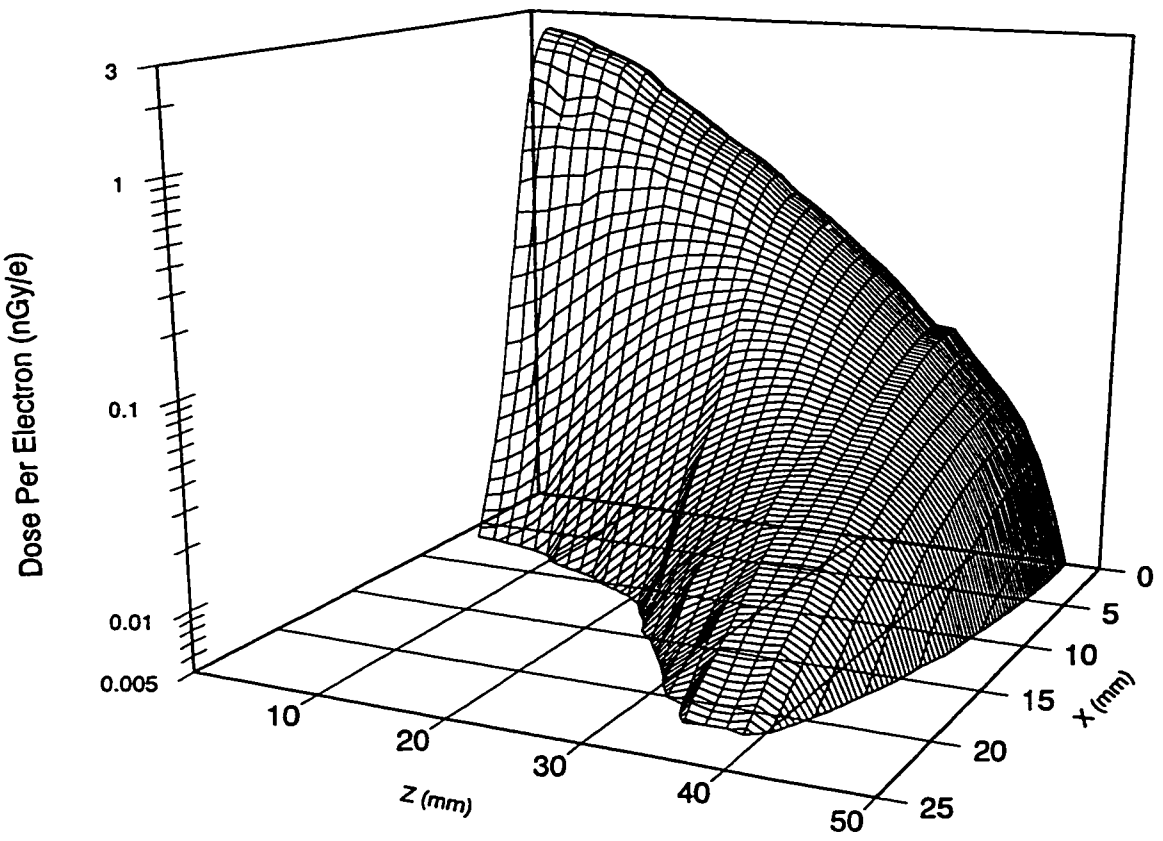

Figure 6.15 3-d log plot of reconstructed dose distribution

The dose distribution at the centroid position as a function of depth, $\dot{d}(0,z)$, is displayed in Figure 6.16. It should be pointed out that an extra point at z = 0.13 mm was added by using equation (6.18) on the peak dose measured from the surface lateral beam dose profiles of two films at different exposure periods (see next section). The depth dose distribution was fitted with a simple exponentially decreasing function. With an R^2 = 0.99992, the fitted parameters for the dose rate in nGy/e as a function of depth were determined to be,

$$\dot{d}(0,z) = (0.0002 \pm 0.0019) + (2.939 \pm 0.079)\, e^{\frac{-z}{(8.25 \pm 0.13)}}. \qquad (6.19)$$

The experimental data will also be compared to results obtained by the Monte Carlo simulation in the next chapter.

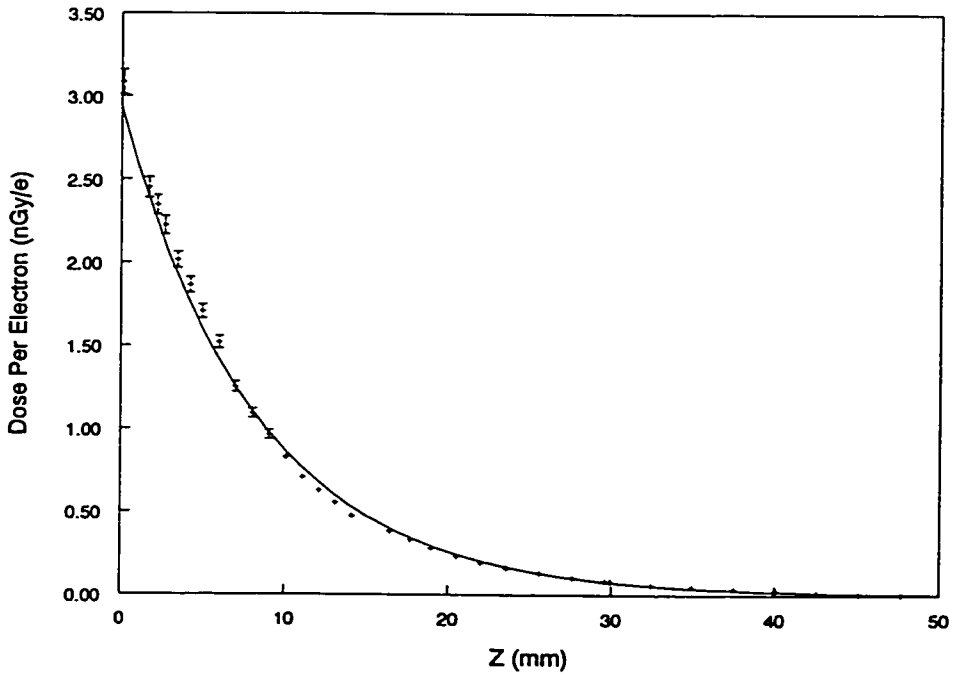

Figure 6.16 Depth dose distribution at centroid

6.4.4 Lateral beam profile

The small films that were put on top of the Lucite phantom measured the beam profile on the surface of the phantom. The net optical density on the film was calculated with respect to a point on the film with the highest transmission. Then, the optical density was converted to dose by using the ^{60}Co calibration. Figures 6.17 and 6.18 show contour plots of the surface dose distribution for two films with exposures of 50 and 5 s, respectively. The films, which will be referred to as film S2 and S3, were each irradiated along with the edge-on film 2 and 3, respectively. Note that the coordinates are somewhat arbitrary. But the y-axis of the plots is as close as possible to parallel to the top edge of the edge-on films. In Figure 6.17, there are 21 contour levels in the plot, each representing 5 Gy, to a maximum level of 105 Gy. In Figure 6.18, 19 contour levels, with each level representing 0.7 Gy, up to a maximum of 13.3 Gy are shown. In both plots, the beam profile appears to be elliptical with its semi-major axis not parallel to the y-axis. The dose distribution was, therefore, fitted with a 2-d Gaussian surface in the form of,

$$d(x,y) = a_0 + a_1 \exp\left\{-\frac{1}{2}\left[\left(\frac{\hat{x}(x,y)}{a_3}\right)^2 + \left(\frac{\hat{y}(x,y)}{a_5}\right)^2\right]\right\}, \tag{6.20}$$

where a_i are the fitting parameters, and $\hat{x}(x,y)$ and $\hat{y}(x,y)$ are in a rotated frame of coordinates relating to x and y, respectively, by,

$$\begin{aligned} \hat{x}(x,y) &= (x-a_2)\cos(a_6) + (y-a_4)\sin(a_6), \\ \hat{y}(x,y) &= (y-a_4)\cos(a_6) - (x-a_2)\sin(a_6). \end{aligned} \tag{6.21}$$

The fitting parameter, a_0, represents the background, which is assumed to be a constant, and a_1 models the maximum dose in $d(x,y)$. a_3 and a_5 fit the standard deviation of the

Gaussian peak in the x and y directions, respectively. The fitted centroid position is at (a_2,a_4), while the angle of rotation is a_6. Table 6.7 lists the results of the fitting for both films.

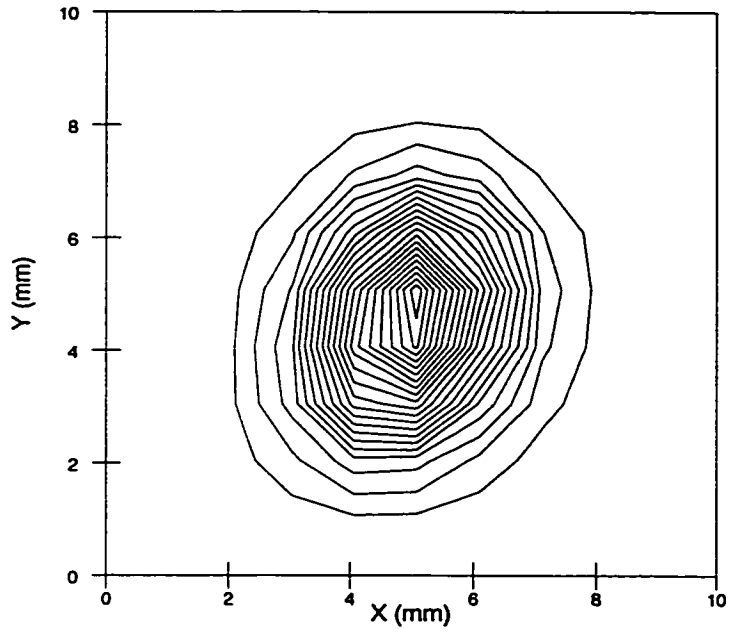

Figure 6.17 Contour plot of surface dose distribution on film S2

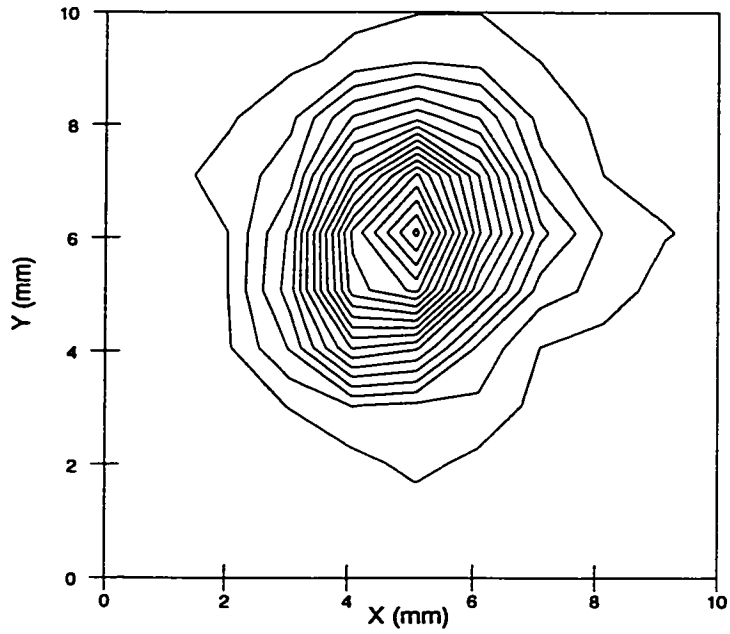

Figure 6.18 Contour plot of surface dose distribution on film S3

Film Number	S2	S3
a_0 (Gy)	0.91±0.11	0.36±0.03
a_1 (Gy)	112.01±0.73	13.40±0.16
a_2 (mm)	4.945±0.007	4.883±0.013
a_3 (mm)	0.970±0.007	1.036±0.013
a_4 (mm)	4.565±0.009	6.007±0.017
a_5 (mm)	1.391±0.010	1.459±0.019
a_6 (radians)	-0.283±0.013	-0.302±0.025
R^2	0.997	0.990

Table 6.7 Fitting results of $d(x,y)$ for films S2 and S3

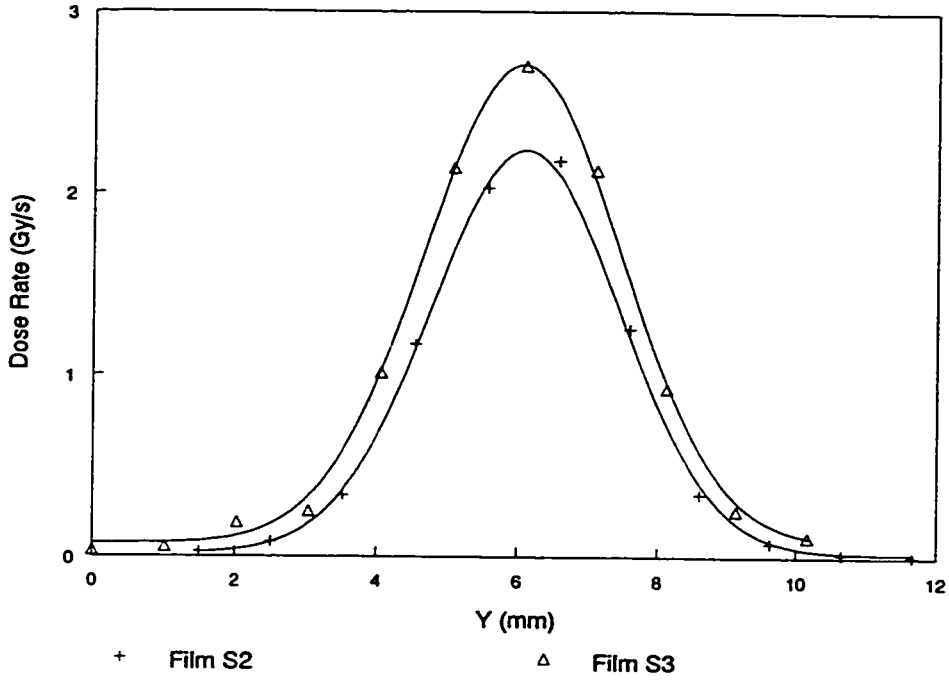

Figure 6.19 Fitted lateral dose rate distribution for films S2 and S3

The profile in y, converted to dose rate, nearest to the peak dose in x was extracted from the contour plots of both films and is illustrated in Figure 6.19. The data points are shown with their respective 2-d Gaussian fitted surface functions. Note that the y coordinates of the film S2 scan were shifted so that its centroid would coincidence with that of the film S3 scan.

6.4.5 Lateral electron beam spread

The lateral spread of the electron beam can be characterized by the variance of the lateral dose distribution as a function of depth. The lateral spread gives information on the electron scattering of the beam within the Lucite phantom. It is also related to the linear scattering power of the beam, which will be discussed in the next chapter. The

variance, $\sigma^2(z)$, was calculated by finding the second moment of the reconstructed $\dot{d}(x',z)$ at all z:

$$\sigma^2(z_j) = \frac{\sum_i \dot{d}(x_i', z_j) x_i'^2}{\sum_i \dot{d}(x_i', z_j)}. \tag{6.22}$$

The uncertainties in the variance were derived by the usual error analysis, yielding,

$$\delta\left(\sigma^2(z_j)\right) = \frac{\sqrt{\sum_i \left[\left(x_i'^2 - \sigma^2(z_j)\right)\delta\left(\dot{d}(x_i', z_j)\right)\right]^2}}{\sum_i \dot{d}(x_i', z_j)}, \tag{6.23}$$

where the symbol, δ, denotes uncertainties. Note that the uncertainty symbol has been changed from the earlier σ to distinguish the uncertainty in the variance from the standard deviation of the lateral distribution. Figure 6.20 displays the variance of the lateral distribution as a function of depth. The variance increases with depth until $z \sim 3.5$ cm, where the variance decreases sharply toward the end of the electron range. This behaviour and the comparison with Monte Carlo data and theories will be discussed in the next chapter.

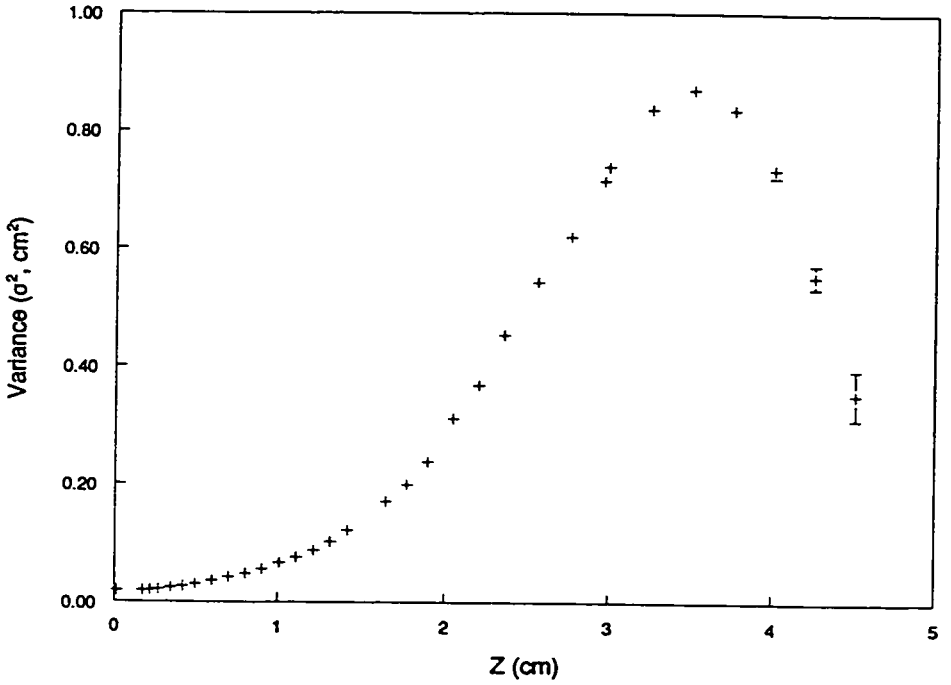

Figure 6.20 Variance of lateral distribution as a function of depth

CHAPTER 7

DISCUSSION

The results presented in Chapter 6 will be discussed and compared with theoretical or expected data in this chapter. In particular, the results of the intercalibration between the uniform ^{60}Co and ^{32}P irradiations are examined. The depth dose distributions of the edge-on irradiation by β particles and electrons will be compared to their respective expected results. Much of the expected results are derived from Monte Carlo (MC) simulations. The methodology in simulating the irradiation geometry will be described.

7.1 Optical density-to-dose methodology

The methodology of the optical density-to-dose conversion using the interpolating-spline fitting and χ^2 minimization method (ISFCSMM) has been presented in Chapter 5. The theoretical and experimental testing of the method was described in Sections 5.2.3.1, 6.1, and 6.2. The theoretical test, performed by deviating the optical density with a Gaussian distributed random value, demonstrates that the methodology is feasible. It also shows that the uncertainties associated with the calculated dose using the ISFCSMM are very small. Therefore, the uncertainties in dose, obtained experimentally, are dominated by external factors such as film nonuniformity and instability of the MDIS, etc. It is possible to improve the dose precision further by minimizing the effects of these

external factors. For example, the nonuniformity effects of the film can be reduced by employing the double-irradiation method by Zhu *et al.* (1997).

Although the ISFCSMM has been found to be theoretically feasible, experimentally, the precision and accuracy of the method depend on the number and the choice of wavelengths utilized. The choice of wavelengths depends on the dose deposited, and it leads to the proposed 2-step process of the χ^2 minimization method as described in Section 5.2.4. With the wavelengths carefully selected, increasing the number of these wavelengths would improve the precision of the resulting dose. However, experimentally, the time it takes to scan a film increases almost linearly with the number of wavelengths. For example, it can take over 2 hours to finish one horizontal scan at 126 wavelengths. Therefore, to reduce the scanning time, one can use a faster scanner, a multiple wavelength p-i-n diode, or simply reduce the number of wavelengths. However, if the number of wavelengths is so few that filtering the experimental data noise cannot be achieved, the calculated dose may not have good precision or accuracy. Hence, an optimal number of strategically chosen wavelengths dependent on the dose range is worth exploring.

7.2 Comparison between measured and expected doses

The comparison between the measured and expected doses (see Section 6.2.3) serves to provide an experimental test of the optical density-to-dose methodology using the ISFCSMM, and to confirm the possibility of intercalibration between γ and β irradiations. The results of the comparison have been shown in Table 6.5, Figures 6.5a

and 6.5b, and the comparison is summarized in equation (6.11). The equation demonstrates a linear relationship between the measured and expected doses, with slope and intercept essentially of 1 and 0, respectively, as expected.

The values of the measured dose in Table 6.5 have precision of better than 1% above 4 Gy, 1 – 3 % between 0.5 and 4 Gy, and ~ 6% at about 0.2 Gy. Most of the measured dose values agree within uncertainties with the expected values at the 95% confidence level. But the films of number 2, 7, and 11 do not show agreement even within 3 standard deviations and have percentage deviations of -4.3, +6.4, and -21% from the expected values, respectively. It should be pointed out that the dose deposited to film number 11 (~ 0.2 Gy) is actually smaller than the lowest calibrated dose of 0.33 Gy. If additional films are calibrated between 0 and 0.33 Gy, the accuracy of the low dose measurements may improve. But the accuracy and precision are still limited by the background noise of the measurement. The overall root mean square relative deviation between the expected dose and the measured dose was calculated to be about 7%. If the last data point (film #11) were to be ignored, the relative deviation improves to about 3%. From the present results, the measurable low dose limit is set conservatively at 0.5 Gy. Note that this level of accuracy was obtained with limited or no control of external factors, such as temperature during irradiation and storage, exposure to ambient light and readout light source, etc, which could affect the film response. Other factors that might have affected the results are described in the following subsections.

7.2.1 Calibration dose uncertainties

The uncertainties in the measured dose (see Table 6.5), calibrated from the ^{60}Co irradiation, were obtained by calculating the standard deviation of the 10 scans on different parts of the film and did not take into account the uncertainties in the calibration dose. The uncertainties in the calibration dose include many factors such as the precision of the ionization chamber used to calibrate the ^{60}Co source, the uncertainties in the SSD, the field size, the timing device that controls the exposure period, and the transit time of the source before and after the irradiation. The combination of these uncertainties is about 1% of the absorbed dose (Farrell 1999). However, it is expected that the actual percentage uncertainties at very low doses would be larger. Incorporating these uncertainties into the measured dose would give a slightly better agreement between the measured and expected doses, but would not alter their relative deviations.

7.2.2 Efficiency of the liquid scintillation counter

The counting efficiency of the liquid scintillation detector was obtained experimentally by Niven (1998) to be $100 \pm 1.5\%$. The possibility that the efficiency can be greater than unity is clearly unexpected. It is difficult to determine the reason(s) for this anomaly. Nevertheless, the counting of high energy beta particles, because of their high light output, is extremely efficient, typically greater than 99% (see for example, Fox *et al.* 1999). Therefore, any systematic error as a result should be less than 1%.

7.2.3 Dose to film conversion

The measured and expected doses given in Table 6.5 are actually the doses to water, rather than the doses to film. The reason is that the standard dose calibration in clinical settings is to water, and it is usually this value that is calculated and compared in papers or reports. If the dose to water is to be converted to the dose to film, then the conversion should be done to the radiosensitive layers of the film. This conversion is not trivial, however, because of the numerous layers of the film involved.

For the calibration films irradiated by the ^{60}Co photons, the γ-rays passed through air and 5 cm of polystyrene before reaching the film, which was enclosed by polystyrene of saturation thickness. The dose rate was calibrated by a technician using an ionization chamber; the measured current was converted to the dose rate to water in accordance with the method recommended by the AAPM Task Group 21 (Schulz *et al.* 1983). If the film is treated as a uniform single layer made of Lucite, chosen because of its proximity to the actual film materials, then the dose to film, d_{film}, can be calculated from the dose to water, d_{water}, by,

$$d_{film} = d_{water} \frac{(\bar{\mu}_{en}/\rho)_{film}}{(\bar{\mu}_{en}/\rho)_{water}}, \tag{7.1}$$

where $\bar{\mu}_{en}/\rho$ is the mean mass energy-absorption coefficient. Using data obtained from Hubbell and Seltzer (1997), the ratio of the mean mass energy-absorption coefficients of Lucite to water at photon energy of 1.25 MeV was calculated to be 0.969. This value is very close to the one quoted by Schulz *et al.* (1983) of 0.965.

For the films irradiated by ^{32}P in the irradiation facility, the β particles had to travel through water, air, and Mylar sheets before reaching the film. Again, the measured dose deposited to the film is given in dose to water. The dose to film can be approximated by equation (2.13). This equation states that every time the β particles cross a boundary, the dose in the new medium can be calculated with respect to the dose in the previous medium multiplied by the stopping power ratio between the two media, provided that the fluence of the particles is the same in both media. Therefore, under the same assumption of the Lucite makeup of the film as above, the dose to film can be calculated by,

$$d_{film} \approx d_{water} \frac{(\bar{S}/\rho)_{air}}{(\bar{S}/\rho)_{water}} \times \frac{(\bar{S}/\rho)_{mylar}}{(\bar{S}/\rho)_{air}} \times \frac{(\bar{S}/\rho)_{film}}{(\bar{S}/\rho)_{mylar}} = d_{water} \frac{(\bar{S}/\rho)_{film}}{(\bar{S}/\rho)_{water}}. \qquad (7.2)$$

The mean stopping power ratio between Lucite and water at the average energy of 0.6949 MeV of ^{32}P β particles is 0.968, obtained from ICRU (1984b). This value is almost identical to that of the mean mass energy-absorption coefficient ratio between Lucite and water in the ^{60}Co case. Therefore, in the first order approximation, the use of dose to water for comparison is justified.

7.2.4 Expected dose corrections

The loss of β dose corrections in air, Mylar sheets and film substrate have been described in Section 6.2.2. The corrections used the depth dose distribution generated from MC simulation for a plane source in water. Therefore, the loss of dose in the

medium was not the dose to medium, but to water. However, Cross *et al.* (1992) have shown that, if the depth of the dose distribution is expressed in area density, then the integral of the plane source to produce a volume source is insensitive to the medium of the absorbed dose. On the other hand, when β particles cross a boundary, the dose in the new medium is changed by approximately the mass stopping power ratio between the two media (see equation 2.13). However, as long as the dose loss correction is performed in dose to water, this boundary effect would effectively be cancelled out. Thus, it is justified to compute the correction factor by summing the thickness in area density of all the attenuating media. The overall dose loss correction factor was calculated to be 20.67%, while the correction factor due to the film substrate only was determined to be about 20%. Using the dose point kernel method, Fox *et al.* (1999) also calculated the film substrate correction factor for ^{32}P irradiation and found it to be about 17%. Although the discrepancy is not large, it may indicate a need to refine the techniques involved.

7.2.5 Comparison with other methods

Direct comparison of the precision and accuracy of dose, obtained using the ISFCSMM, with other methods is difficult because the quoted uncertainties in the measured dose are dependent on many other external factors, such as the uncertainties arising from the dose irradiating and measuring equipment. Moreover, the accuracy of the calculated dose is usually not known because it requires an independent method to test the calibration. Typically, combined uncertainties in the measurements of optical density are about 2.5% to 5% at 1 σ (McLaughlin *et al.* 1991 and Meigooni *et al.* 1996).

Klassen *et al.* (1997) managed to improve the precision to less than 1% by using a double-irradiation method. But their method was tested only up to 12 Gy. The precision, i.e. the uncertainties, in the measured dose in Table 6.5 is better than 1% from about 4 to 210 Gy, less than 3% from about 0.5 to 4 Gy, and 6% at about 0.2 Gy. This is better than the typical precision obtained, except at low doses.

Another strength of the ISFCSMM is the large range of dose that can be measured. The data presented in Table 6.5 suggests that the range is from 0.5 Gy to beyond 212 Gy. This range is much larger than the suggested range of 1 to 50 Gy by the manufacturer (Fairman 1998), and 3 to 100 Gy by the AAPM Task Group 55 (Niromand-Rad *et al.* 1998). The upper limit can probably be increased to about 500 Gy (Klassen *et al.* 1997). With a properly controlled environment and more sensitive instruments, the lower limit may be extended to below 0.1 Gy (see Table 5.1).

7.3 Edge-on ^{32}P irradiation

The edge-on ^{32}P irradiation results have been presented in Section 6.3. The experiment was performed twice. In the first trial, it was discovered that there was no control on the ambient light in the laboratory where the experiment took place. Therefore, potentially, the dose deposited in the film might include a significant UV dose, especially near the end of the β range of about 7 mm in Lucite. To address this problem, the experiment was repeated with shielding against any ambient light. As mentioned in Section 6.3.1, it was found that in the second trial, the $OD(\lambda)$ had negative values at all

wavelengths at distances greater than the β range. The negative values are not expected because physically, they indicate a loss of dose over the course of the experiment, which is impossible. The fact that the reference films do not suffer from this problem also rules out potential problems with the readout instruments or film fading. Therefore, it is speculated the Mylar sheet that was used in protecting the film during irradiation (see Section 4.3.1) might have extracted a very thin layer of the film when the Mylar sheet was removed at the end of the irradiation experiment. This is a fair speculation because the outer layer of the film is made of Mylar as well.

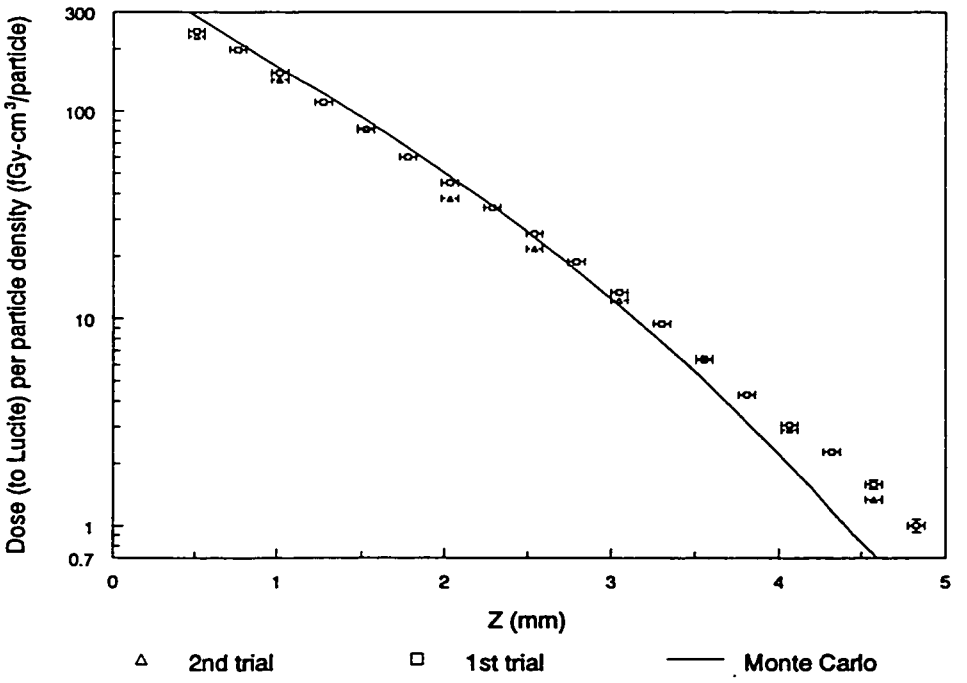

Figure 7.1 Comparison between experimental and MC simulated depth dose distributions (^{32}P edge-on irradiation)

To remedy this problem, it is assumed that a constant thickness of the thin layer was removed so that the film had the same thickness throughout. This thin layer is also assumed to be small enough so that correction to the film calibration is negligible. Furthermore, an assumption is made that the dose deposited in the film beyond the β range is solely due to the Bremsstrahlung photons, and its contribution is relatively constant over the entire film. The constant contribution assumption is fair because photons can travel a much longer distance than β particles. Hence, the optical density was computed with respect to the points on the film with the highest intensity transmission. It is possible that the film in the first trial also suffered from this problem. But the dose that was potentially contributed by the ambient light might have masked the problem.

Figure 7.1 shows a direct comparison of the two trials (see Figures 6.6 and 6.7) along with data from MC simulation, which will be described in the next subsection. The dose distributions have been converted to fGy (femto-Gy) per source particle density of the β particles. In addition, assuming the UV and Bremsstrahlung dose contribution in the first trial is constant, a dose of 0.5 Gy was subtracted from the original dose distribution before the conversion. This value was chosen because it is roughly the Bremsstrahlung dose just beyond the end of the β range in Lucite. Therefore, only the β dose distributions of the two trials were compared. The uncertainties in the dose were obtained from the standard deviation in the mean of the 10 x-scans of each film. The graph illustrates that the two sets of dose distribution for the most part agree to within

10% for most points. In the second trial, however, there are two points that, at about z = 2 and 2.5 mm, do not appear to follow the general shape. Those points are about 16% smaller than those in the first trial. Perhaps these points are simply bad points on the film. It should be noted that the dose near the front edge (up to ~ 1.5 mm) is not very reliable because the optical density varies unpredictably near a film edge (Klassen *et al.* 1997). It should also be pointed out that the minimum measurable dose of 0.5 Gy is equivalent to about 0.7 fGy/source-particle-density. This minimum measurable dose does not include the subtraction of the 0.5 Gy in the first trial.

7.3.1 Comparison with Monte Carlo simulation

The MC curve in Figure 7.1 was generated using the Tiger code of the Integrated Tiger Series (ITS) version 3.0 (Halbleib 1988a) as follows. The Tiger code can only simulate a depth dose distribution created by a plane source. Therefore, the ^{32}P volume source was modeled by a series of plane sources in water. Table 7.1 lists the components of the simulated geometry. The material in each layer of the ^{32}P irradiation facility is listed in column 1, and the layers are in the same order as the simulation. Each layer is assumed to be infinitely wide. The first layer simulates the air above the ^{32}P irradiation facility. The second layer models the Lucite top where the film was inserted. In this layer, over 100 subzones were divided and scored individually to determine the simulated dose distribution as measured by the film. The third layer consists of a Mylar sheet that was used to prevent evaporation and contamination. The fourth layer simulates the source solution, which is essentially water with a small amount of HCl, while the fifth

layer refers to the bottom part of the ^{32}P container. Column 2 describes the composition and the weight fraction of each layer. The density and the thickness of the layers are listed in columns 3 and 4, respectively.

The source was simulated by encompassing the beta spectrum of ^{32}P, using 50 energy bins divided equally from 0 to 1.71 MeV. The direction of the source particles was assumed to be isotropic. Since only one plane source is allowed in the Tiger code in each MC simulation run, the simulation was performed 19 times at 19 different plane source positions in layer number 4. The simulation was performed on a computer using the Intel Pentium® II processor at 266 MHz. Each run tracked 10 million histories (or particles), and it took roughly about 15 hours to complete.

Layer Material	Composition: Weight Fraction	Density (g/cm^3)	Thickness (cm)
1. Air	C: 0.000124 N: 0.755267 O: 0.231781 Ar: 0.012827	0.0012048	500 +
2. Lucite	H: 0.080538 C: 0.599848 O: 0.319614	1.19	2.8
3. Mylar	H: 0.041959 C: 0.625017 O: 0.333025	1.40	0.00025
4. ^{32}P mixed solution (in water)	H: 0.111527 O: 0.884237 Cl: 0.004236	1.004375	3.15
5. Lucite	Same as layer 2	1.19	~ 17

Table 7.1 Simulated geometry for ^{32}P edge-on irradiation

At the end of each simulation, the Tiger code outputs the results in a file that contains the average dose, d, times unit area, a, deposited by a source particle in each scoring subzone. The ith subzone is at distance z_i and the plane source is at distance $-z'$, from the front edge of the ^{32}P solution. Then, using the results from all 19 simulations at various plane source distances, the dose deposited per source particle density in the ith subzone was calculated by,

$$\frac{d(z_i)}{[N]} = \frac{a}{N}\int_t d(z_i - z')dz', \tag{7.3}$$

where N is the number of source particles, and t = 3.15 cm is the thickness of the ^{32}P source. This integral was accomplished by spline fitting the $ad(z_i - z')/N$ as a function of the 19 plane source positions, and then, integrating the spline fitted function over the source thickness, t. This process was repeated for all the subzones of interest so as to generate the depth dose distribution from a volume ^{32}P source.

To compare the MC results with the experimental β dose distributions, the tail end dose of about 0.36 fGy per source particle concentration, deposited by the Bremsstrahlung photons, was subtracted from the MC generated depth dose distribution. Furthermore, since the simulated dose is to Lucite, the mass stopping power ratio of water to Lucite of 1.033 was multiplied to the MC dose to provide the dose distribution to water. Note that although the dose was converted to the dose to water, the shape of the distribution is still to Lucite; the multiplication of the mass stopping power ratio does not alter the shape.

The MC data appear to be in close agreement with the experimental values from the first trial from about $z = 1$ to 3 mm. However, beyond 3 mm, the MC values begin to deviate significantly from the two sets of experimental data. It is not clear what factor(s) would cause this discrepancy, though similar discrepancies are also observed in the electron edge-on irradiation experiment (see next section). An attempt was made to shift the curve, constrained by the area under the curve, by "shrinking" it sideways and "expanding" it vertically by a factor of 1.07. The shifting appears to provide a better fit, though no physical reasons can be associated with the shift.

7.4 Edge-on 10 MeV electron beam irradiation

The results of the edge-on irradiation by the 10 MeV electron beam have been shown in Section 6.4. The determination of the optical density of each irradiated film, which is described in Section 6.4.1, was relative to a blank region on the same film. This method implicitly assumes that the blank region, which is either near the front (away from the beam axis) or near the far corners of the film (> 11 cm from the front), depending on where the highest transmission is, has no dose deposited. However, it appears that there are no true dose free regions. At the front edge of the film away from the beam axis, a very small amount of dose seemed to have been deposited, likely due to the secondary electron and Bremsstrahlung doses resulting from the interaction between the electron beam and the thin stainless steel exit window of the linear accelerator. At increasing depth, the "external" dose begins to diminish. At the same time, the Bremsstrahlung dose created in the Lucite phantom begins to take over. This

Bremsstrahlung dose gradually decreases as the electrons approach their range of about 4.3 cm. Fortunately, the radiation yield at 10 MeV in Lucite is only about 3.7%, and at low energy (~ 10 keV) is of the order of 10^{-2}%. Therefore, only the high energy electrons near the beam entrance can potentially give a significant Bremsstrahlung dose. Factoring in the small solid angle projected from the beam entrance to the far corners of the film, the Bremsstrahlung dose contribution to the blank regions should not be very significant. Therefore, the resulting decrease in the optical density, and thus, the measured dose, calculated with respect to the blank regions should be minimal.

Another potential problem that can alter the dose distribution arose during the film readout. The film was mounted in a holder, which clamped the film edges tightly, without any support underneath. Therefore, potentially, the film could have sagged in the middle. Since the height of the X-Y stage was adjusted to give an optimal reading, any deviation from this height would result in a lower transmission. The lower transmission could be interpreted as an increase in dose. Hence, extreme care was taken to ensure that the film was flat during scanning.

7.4.1 Experimental lateral dose distribution

The measured optical density was converted to dose using the ^{60}Co calibration. Figures 6.8 and 6.9 display the dose rate distributions of films 1, 2 and 3 at depth z = 14 and 19 mm, respectively. None of the three curves agree entirely with one another, though films 1 and 2 appear to differ only by a constant background. It is not certain why there is such discrepancy between the two curves. Perhaps film 2 was accidentally

exposed to ambient light. It is possible that the electron beam current changed slightly between irradiations. But this change would only alter the curve by a multiplication factor, and it still does not explain the origin of the background.

The dose rate distribution of film 3 appears to be on a linear, non-zero slope. Moreover, a number of points seems to be out of place. These anomalous points are not unexpected because the films used for this experiment are the earlier batches of the MD-55-2 version. They are supposed to be less uniform than the later batches, and the nonuniformity tends to be more apparent at low doses. The presence of the linear slope background, however, cannot be explained by any obvious mechanism. One speculation is that the film was somehow exposed to an unknown weak external source. It should be mentioned that the distributions of film 3 shown in both Figures were not used in the reconstruction of the dose distribution.

7.4.2 Centroid position

In order to remove the background of the dose distribution as described in Section 6.4.2, the lateral dose rate distributions of all three films were first fitted with a modified Gaussian distribution (see Figure 6.10). The reason that the Gaussian fit was chosen is primarily the result of the Fermi-Eyges equation. As discussed in Section 2.6, the Fermi-Eyges equation is expected to break down at the end of the electron range. However, it appears that the modified Gaussian fit is actually slightly better near the end of the range than at the beginning, though the fit is less than perfect near the peak or the tails throughout. Despite this revelation, the purpose of the fit is simply to provide

information on the dose distributions to aid the background removal. The most useful piece of information from the fit was the centroid position, which was used to align the lateral dose distributions from the three films.

The centroid position of the lateral dose distributions was unexpectedly found to be dependent on depth (see Figure 6.11). It is not clear if the dependence is physically real, since this phenomenon is not observed in film 1 or 3 at the maximum dose position as a function of depth. Fortunately, the difference between the centroid and maximum dose positions is small (< 1.5 mm near the end of the range) compared to the width of the peak. Therefore, aligning the lateral dose distribution curves of the three films using the Gaussian fitted centroid or the maximum dose position does not appear to show any noticeable difference.

The depth dependence of the centroid, displayed in Figure 6.11, shows that the deviation of the centroid position increases with depth, but not at the same rate for all three films. Since the rate of increase is not linear, this likely rules out a possible cause that the electron beam was not aligned to the center axis of the phantom. One plausible cause is the emergence of an apparent secondary peak, spotted on the right side of the centroid of film 3 in Figures 6.8 and 6.9. The relative height of the peak, with respect to the central main peak, appears to increase with depth. Its presence would affect the centroid position by shifting it toward the direction of the secondary peak. The peak, however, is not observed in the other two films. Perhaps its presence is masked due to its smaller relative size to the central peak. If, in fact, the peak is physically real, its origin is likely from the electron scatter of the main beam, which would probably be improperly

collimated. However, this explanation would lead to the expectation that the relative height of the secondary and the central peak would be constant in all three films. Clearly, this is not the case.

Another plausible cause is that the beam was deflected by an external magnetic field during the irradiation experiment. A numerical calculation of the electron beam path in the presence of a magnetic field is shown in Appendix A. Although the shape of the beam path resembles the centroid deviation curve, it does not explain the difference in the rate of the centroid shift with increasing depth for the three films. It is possible, though unlikely, that the magnetic field strength varied between experiments. Finally, it is conceivable that the deviation is not physically real. It may simply be due to a nonlinear background inherent in the films, but not accounted for in the fitting.

7.4.3 Surface dose distribution

The contour plots of the surface dose distributions of the electron beam have been shown in Figures 6.17 and 6.18. The plots indicate that the beam profile is elliptical, rather than circular as would be expected. As mentioned in the last subsection, the centroid position as a function of depth is nonlinear, and this likely disproves the possibility that the elliptical beam profile was caused by an off-angle projection onto the phantom. A more probable explanation to the elliptical shape is the result of the beam optics in the linear accelerator.

The distribution was fitted with a 2-d Gaussian surface with excellent agreement for both surface films of S2 and S3. Since the beam width is 3 mm wide, it was expected

that the measured beam profile would be flat at the center. A MC simulation of the lateral dose distribution, discussed later in Section 7.4.4.1, also shows a non-flat beam profile at the center near the surface, indicating that the stainless steel window has scattered the beam sufficiently before reaching the phantom. But it is also possible that the beam has an intrinsic Gaussian cross section.

The fitted parameters, a_3 and a_5 (see equation (6.20) and Table 6.7), represent the standard deviation of the Gaussian surface in x and y, respectively. Each parameter is approximately the same for both films, with $a_3 \sim 1$ mm and $a_5 \sim 1.4$ mm. Therefore, the full width at half maximum of the surface dose is ~ 2.4 mm in x and ~ 3.2 mm in y. This is consistent with the beam diameter of 3 mm.

The one-dimensional dose rate profile in y near the peak dose is plotted in Figure 6.19 for both films. The dose rate for film S3 is higher than that for film S2. However, no sign of a linear background with a non-zero slope is observed for either film. The two curves appear to differ by a multiplication factor of roughly 1.2 to 1.3 and a constant of about 0.05 Gy/min. The multiplication factor may be due to a small difference in beam current between the two experiments, while the constant may be a result of the choice of the blank region on the films.

7.4.4 Reconstructed lateral dose distribution

The lateral dose distribution in dose per electron was reconstructed using the measured data from the three irradiated films, and the method has been described in Section 6.4.3. The contour plot of the reconstructed dose distribution is shown in Figure

6.14. The contour shape is consistent with theoretical prediction using the Fermi-Eyges theory for a 10 MeV electron pencil beam in water (Jette *et al.* 1983). However, comparing with the data shown in Brahme (1985), obtained using an algorithm for a narrow 10 MeV electron beam in water, the contour does not have the "pointed" feature along the beam axis beyond the range of the electrons. This feature is attributed to the dose deposited by Bremsstrahlung photons, which are created by the incident electrons in the first few centimeters of their range.

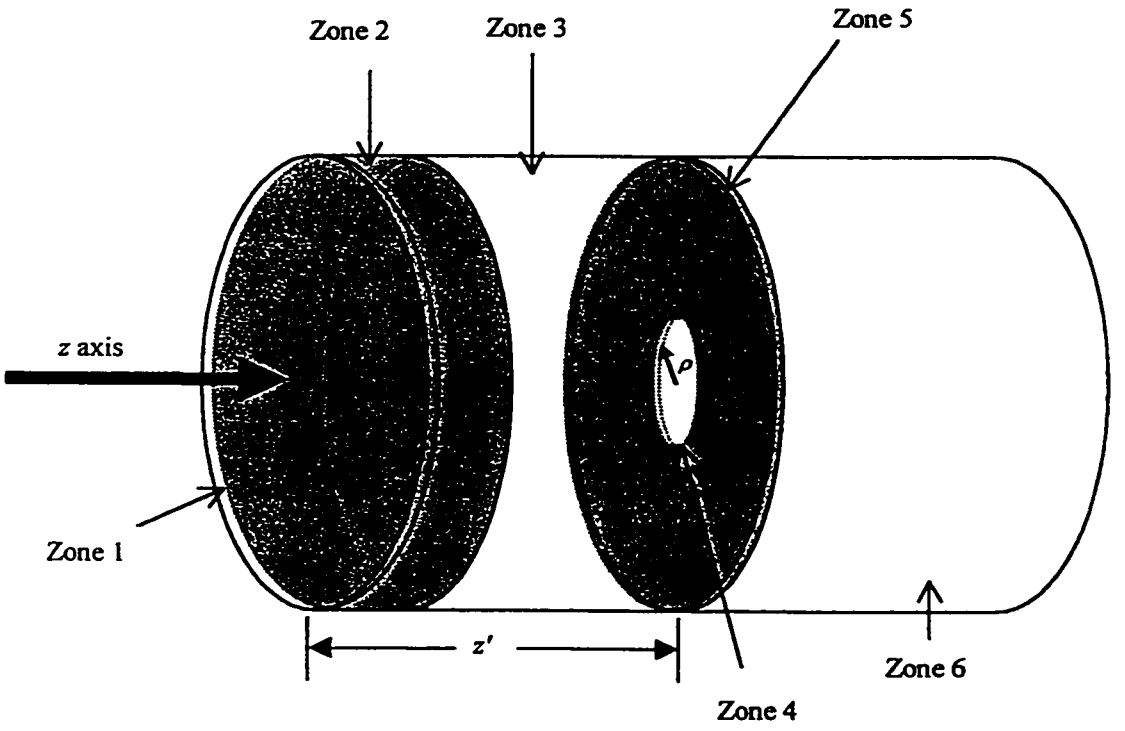

Figure 7.2 Simulated geometry of Lucite phantom

7.4.4.1 Comparison with Monte Carlo simulation

The 10 MeV electron beam dose distribution in Lucite was simulated using the Cyltran code of the ITS, version 2.1 (Halbleib 1988a). The Cyltran code allows one to model an irradiated phantom in a cylindrical geometry, with the source as an external beam. To illustrate the modeling graphically, Figure 7.2 shows a diagram of the irradiation geometry. The z axis defines the beam axis, and the beam enters from the left side of the diagram. ρ is the radius coordinate of the cylinder. The modeled geometry is divided into 6 zones. The region of interest is zone 4, where the lateral dose distribution is simulated.

Table 7.2 lists the properties and dimensions of each zone. Columns 1 and 2 display the zone number and its corresponding material, respectively. Note that the stainless steel exit window of the electron beam is simulated by a thin piece of iron, with density of 7.86 g/cm^3, in zone 1. The thickness of the zones is listed in column 3. In zones 3 and 6, the variable z' represents the transaxial distance between the front end of the cylinder and the center of zone 4 or 5 (see Figure above). The MC run was repeated at various z' from 0.9127 cm to a thickness beyond the range of electrons in Lucite. The last column shows the radius of each zone. In zone 4, the zone is further divided into 90 subzones in concentric rings to be scored individually. Therefore, each ring has a width of approximately 0.0278 cm and a thickness of 0.01 cm. The scored rings give the lateral dose distribution of the electron beam in Lucite.

Zone	Material	Thickness (cm)	Radius (ρ, cm) (min – max)
1	Iron	0.0127	0 – 20
2	Air	0.9	0 – 20
3	Lucite	z' - 0.9177	0 – 20
4	Lucite	0.01	0 – 2.5
5	Lucite	0.01	2.5 – 20
6	Lucite	20.005 - z'	0 – 20

Table 7.2 Properties and dimensions of simulated geometry

The electron beam was simulated by an electron source, with energy of 10.05 MeV and a radius of 0.15 cm, entering in the direction of z. As in the case of the ^{32}P edge-on simulation, the MC run was performed on the Intel Pentium® II 266 MHz computer. 10 million histories were tracked for each run, and a run typically took about one day to complete. In order to attain a precise lateral dose distribution as a function of depth, many runs (> 30) at various z' were acquired.

Figures 7.3 to 7.10 show samples of the MC generated lateral dose distributions (in ρ) at various depths, compared with experimental data given in dose to Lucite (see Figures 6.12 to 6.15). Note that z = 0 corresponds to the front of the Lucite phantom. The experimental dose was originally to water, but the MC simulated dose is to Lucite. Therefore, an average mass stopping power ratio of Lucite to water of 0.963 was multiplied with the original experimental dose to obtain the dose to Lucite. Note that the mass stopping power ratio is very insensitive to energy. From 10 MeV to 1 MeV, the difference in the ratio is less than 0.5%. However, it was found that even after the mass stopping power correction, the experiment data were still consistently higher than the

corresponding MC values by about 8.6% at the peak near the front edge. It is speculated that the average beam current, given as 0.1 nA, might have been varied by the same percentage. Another possibility is the potential discrepancy caused by the fact that the calibration films were not the same batch as the irradiated films, though they were both of the MD-55-2 type. But there has been no indication from the manufacturer or any published papers that the composition or the layer thickness of the films has changed, except the uniformity, from earlier batches to later ones. Hence, this is not a likely explanation. In any case, the experimental values were further reduced by 8.6% to match the MC values to provide a fair comparison in the Figures. Note that the experimental data are denoted by the open square symbol with error bars, and the MC results are represented by two histograms, which refer to the highest and lowest possible values of the dose distribution. These values were obtained by adding or subtracting the MC data values by their respective statistical uncertainties at one standard deviation.

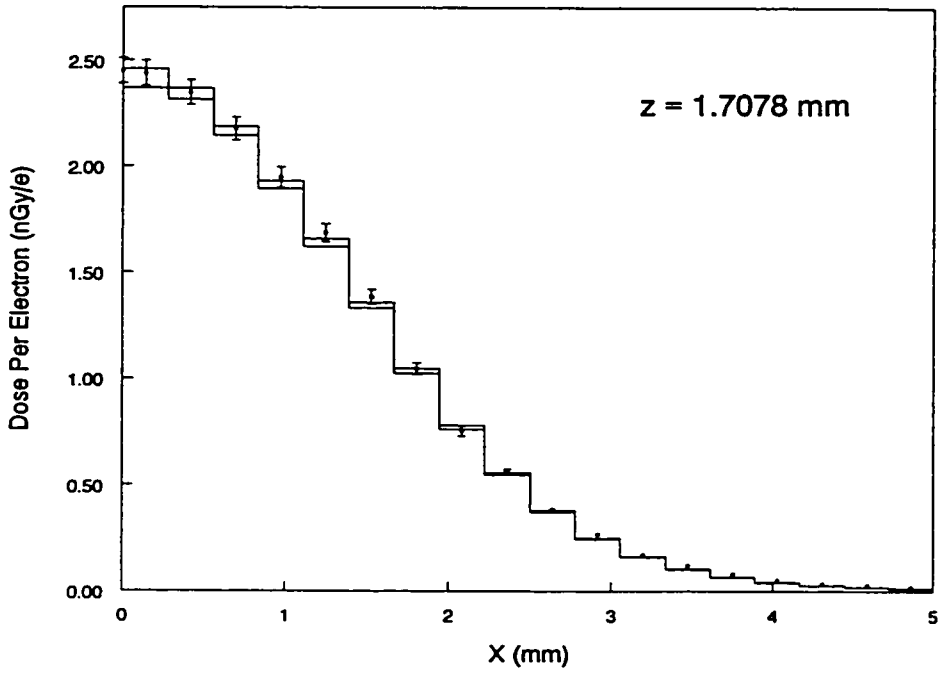

Figure 7.3 Comparison between experimental and MC simulated lateral dose distributions (z = 1.7078 mm)

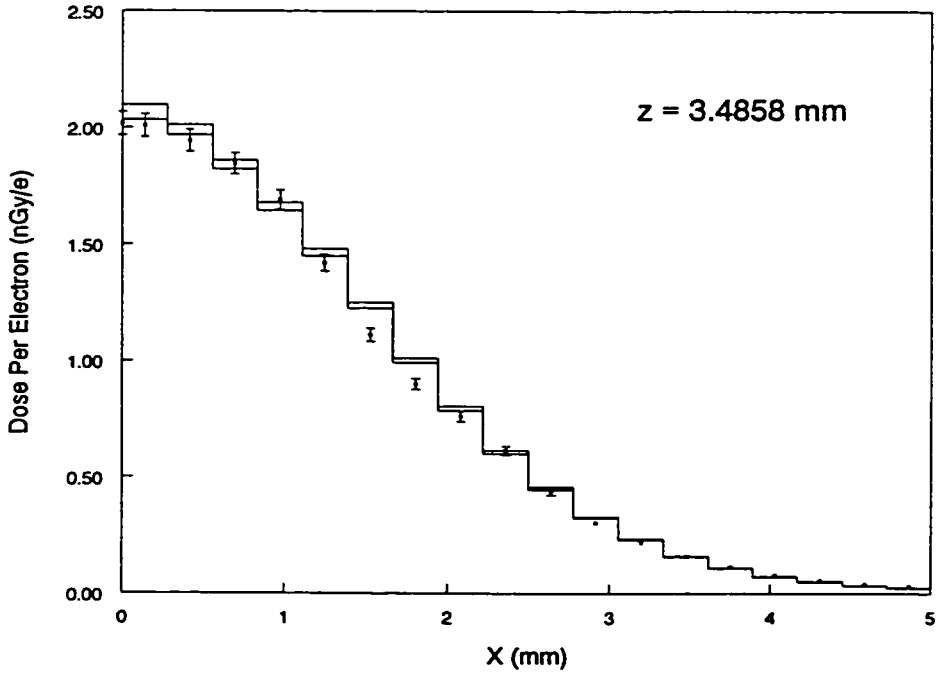

Figure 7.4 Comparison between experimental and MC simulated lateral dose distributions (z = 3.4858 mm)

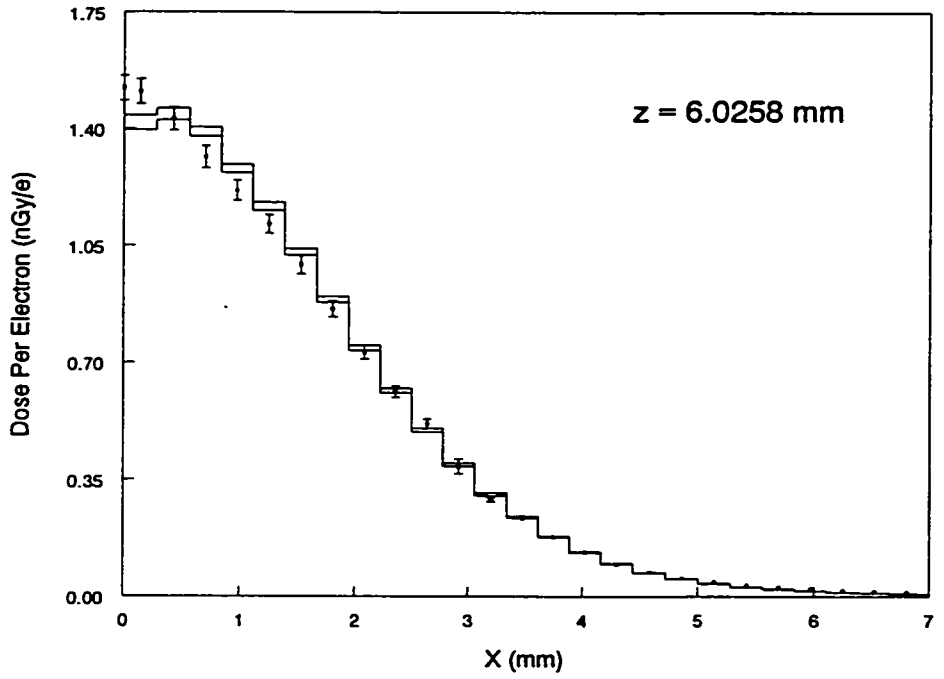

Figure 7.5 Comparison between experimental and MC simulated lateral dose distributions (z = 6.0258 mm)

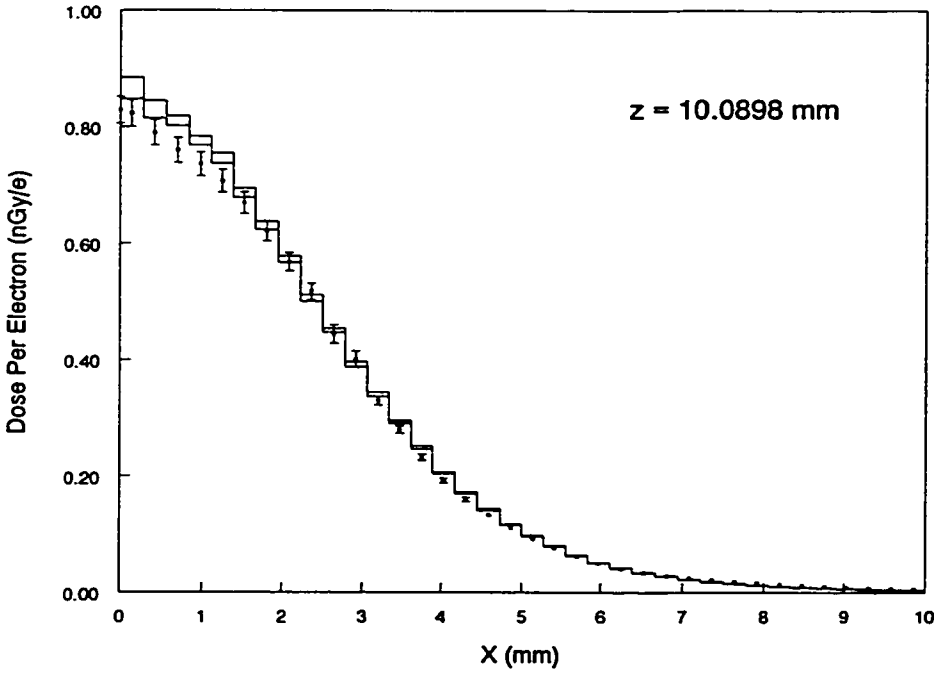

Figure 7.6 Comparison between experimental and MC simulated lateral dose distributions (z = 10.0898 mm)

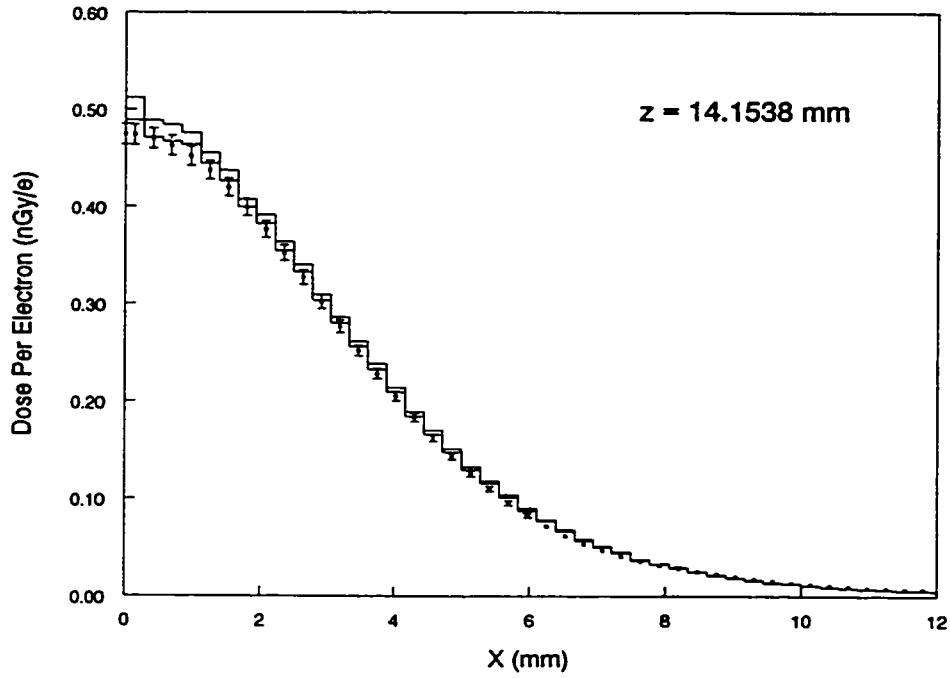

Figure 7.7 Comparison between experimental and MC simulated lateral dose distributions (z = 14.1538 mm)

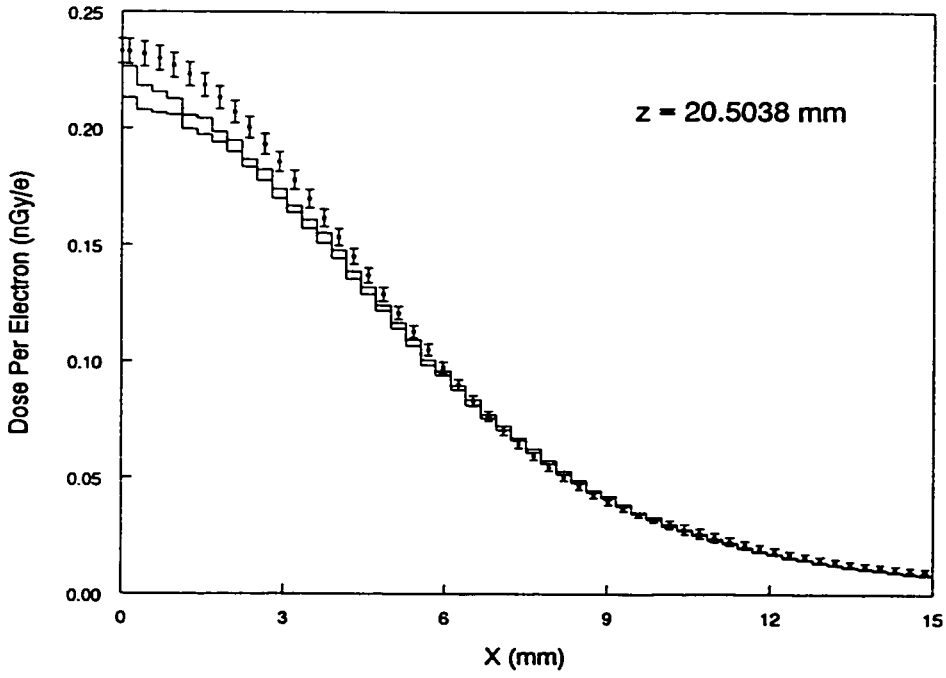

Figure 7.8 Comparison between experimental and MC simulated lateral dose distributions (z = 20.5038 mm)

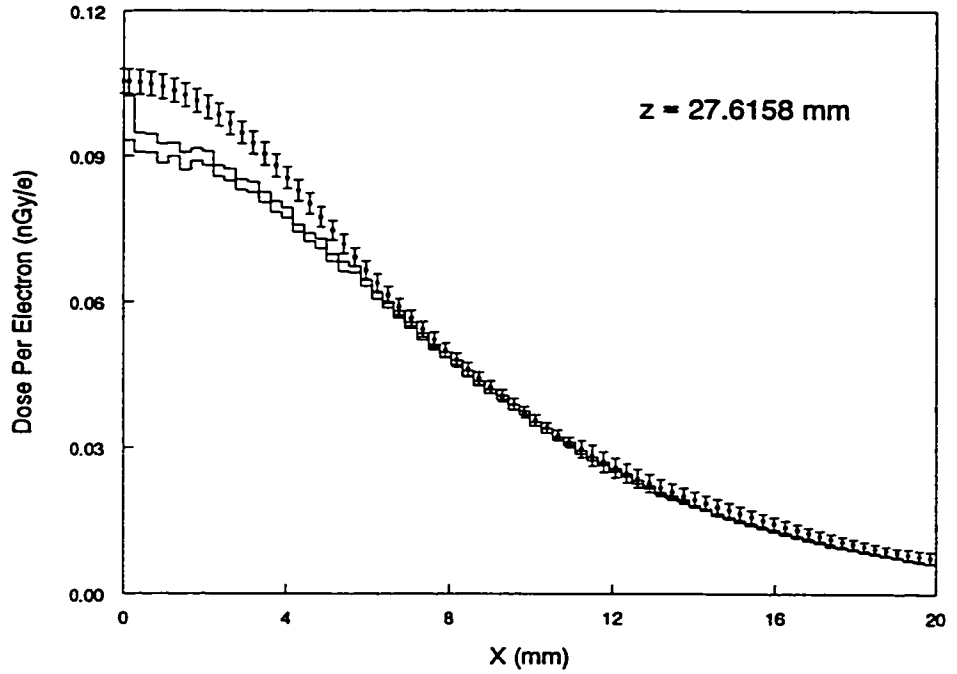

Figure 7.9 Comparison between experimental and MC simulated lateral dose distributions ($z = 27.6158$ mm)

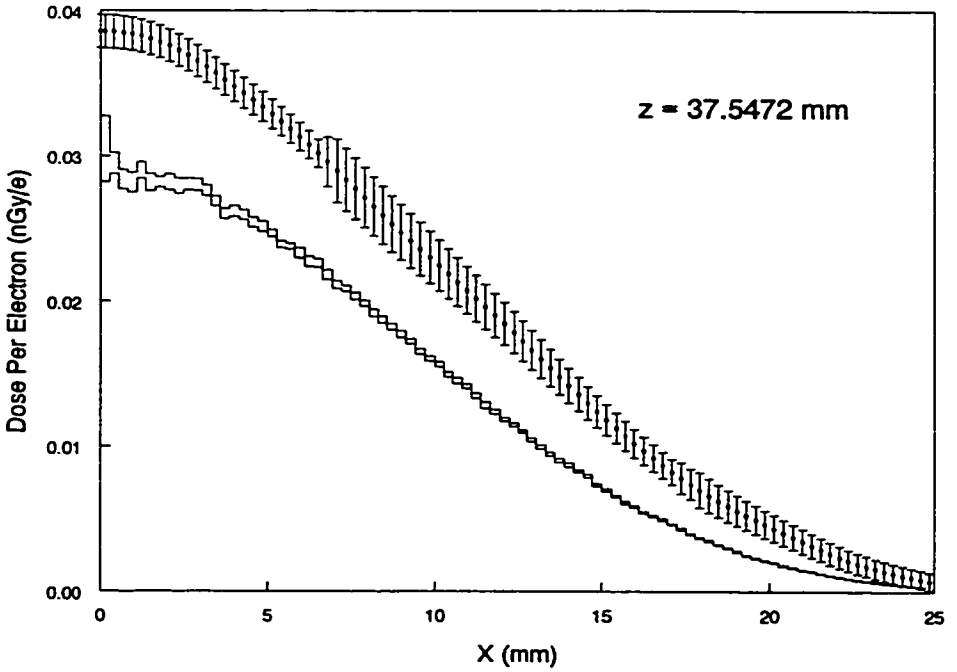

Figure 7.10 Comparison between experimental and MC simulated lateral dose distributions ($z = 37.5472$ mm)

The above Figures demonstrate that overall, the experimental data of the lateral dose distributions compare favorably with the MC generated results, except near the end of the electron range. At z = 1.7078 mm, Figure 7.3 shows that the two distributions agree within uncertainties except at the tail end, where the experimental values are slightly higher than the MC data. This small discrepancy may be physically real since the minimum detection limit of 0.5 Gy corresponds to about 0.02 nGy/e. However, it may also be due to the incorrect modeling of the stainless steel window by a layer of iron. A random survey of the composition of 9 common stainless steels was conducted. It was found that typically, they are made of iron, chromium, manganese, molybdenum, copper, nickel. Of the 9 stainless steels, their effective atomic numbers were calculated, and they range from 25 to 27. Therefore, if the stainless steel window is made of elements with effective atomic number higher than that of iron (Z = 26), then there would be slightly more Bremsstrahlung photons produced, thus increasing the dose slightly at the tail end.

In Figure 7.4 (z = 3.4858 mm), the two distributions agree fairly well except at the two points near the lateral distance of about 1.5 mm, where the experimental values are about 10% lower than those of the MC simulation. However, these two experimental data points appear to be out of place with the others. It is likely that these are just bad points that are inherent in the film.

In Figure 7.5 (z = 6.0258 mm), the experimental dose distribution near the beam axis (i.e. at x = 0) up to 2 mm appears to be consistently slightly lower than the MC distribution, except for the first two points. The discrepancy at the first two points may simply be due to the fact that the MC statistics are poor because of the small scoring

region near the beam axis. Recall that the scoring subzones are a result of dividing the thin cylinder of interest (zone 4) into concentric rings. However, the consistently smaller experimental dose distribution is also observed in Figure 7.6 at z = 10.0898 mm up to x = 6 mm, except between about 1.5 to 3 mm. This trend continues somewhat at z = 14.1538 mm (Figure 7.7). In all three cases, the experimental tail dose remains slightly higher than that of the MC simulation. At z = 20.5038 mm (Figure 7.8), the trend reverses. The experimental data values are now consistently higher than the corresponding MC values, up to x = 6 mm. The difference at the peak is about 5%. But the tail dose points agree well. This trend is also observed in Figure 7.9 at z = 27.6158 mm, with the experimental dose value at the peak about 8% higher than that of the simulated dose. The trend also suggests that the deviation becomes larger at increasing depth. Beyond the depth of about 32 mm, the experimental dose distribution is higher than the MC simulated distribution at all x. This is demonstrated in Figure 7.10 at z = 37.5472 mm. The discrepancies that the experimental values are consistently higher or lower than those of the MC results appear to be real, suggesting perhaps a need to refine the Cyltran code. However, the experiment can be improved with a reduced air gap, a beam exit window material preferably with known composition, a lower atomic number to reduce Bremsstrahlung production, and a more recent and uniform film.

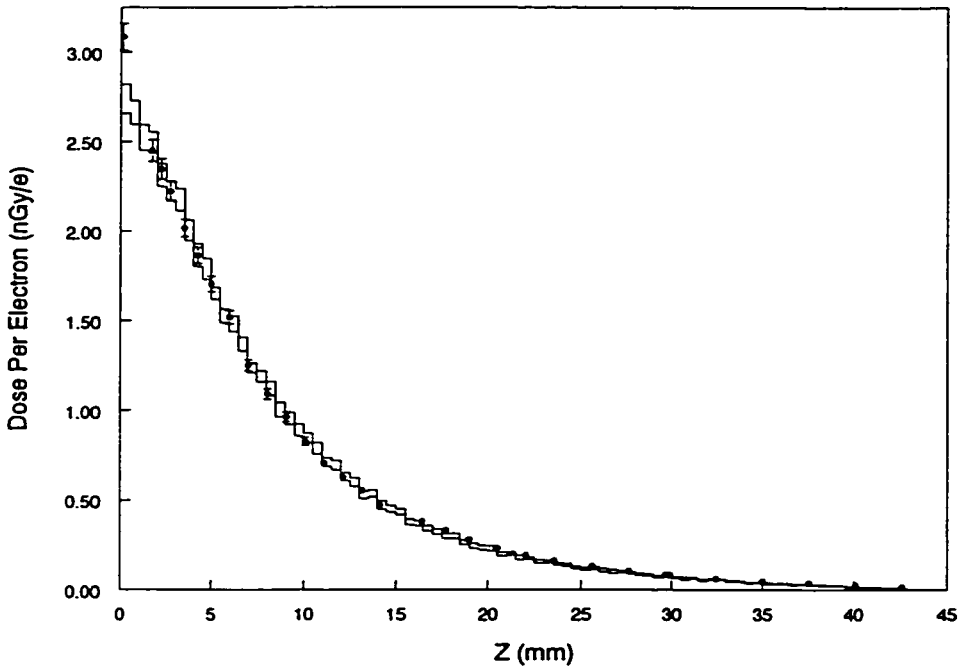

Figure 7.11 Comparison between experimental and MC simulated depth dose distribution at centroid

7.4.5 Depth dose distribution at the centroid

The depth dose distribution at the centroid in the Lucite phantom has been shown in Figure 6.16 and was fitted with a simple exponentially decreasing function. The distribution is similar to that of photons, which also decreases exponentially, though the interaction process is very different. To model the electron depth dose distribution, a separate MC simulation was employed using a slightly different geometry than the one shown in Figure 7.2. The new geometry has a thin cylinder inserted at $z = 0$ to 4.75 cm, with $\rho = 0 - 0.01$ cm in the center. The other zones are modified accordingly to complete the rest of the cylinder. The thin cylinder is the scoring zone of interest and is further divided into 95 subzones along the z axis.

Figure 7.11 displays the comparison of the depth dose distribution at the centroid between the experimental and MC results. The experimental data agree with the MC data within uncertainties except at the first point (difference of about 12%) and the points beyond z = 15 mm. The discrepancy of these latter points is consistent with the lateral distribution results compared earlier. The disagreement at the very first point is, however, not too surprising because the experimental data point was obtained separately from the surface films S2 and S3. Then, a 2-d Gaussian surface was fitted to the surface lateral distribution to obtain the maximum dose value at the Gaussian peak. It is possible that the peak of the surface distribution was not at the center of the phantom; and therefore, did not align with the top of the edge-on film during the experiment. Another possibility is that the peak of the surface dose distribution does not behave as a Gaussian peak.

7.4.6 Lateral electron beam spread

The result of the lateral spread of the electron beam, characterized by the lateral variance, has been presented in Section 6.4.5 and Figure 6.20. The variance increases gradually with depth, as would be expected since electron scattering increases with depth. However, as the electrons approach their range, the variance begins to decrease sharply. This behaviour can be explained by the fact that the scattered electrons away from the beam axis reach their range at a shorter depth than those near the beam axis. As a result, the variance near the end of the range only measures the lateral spreading of the remaining electrons near the beam axis.

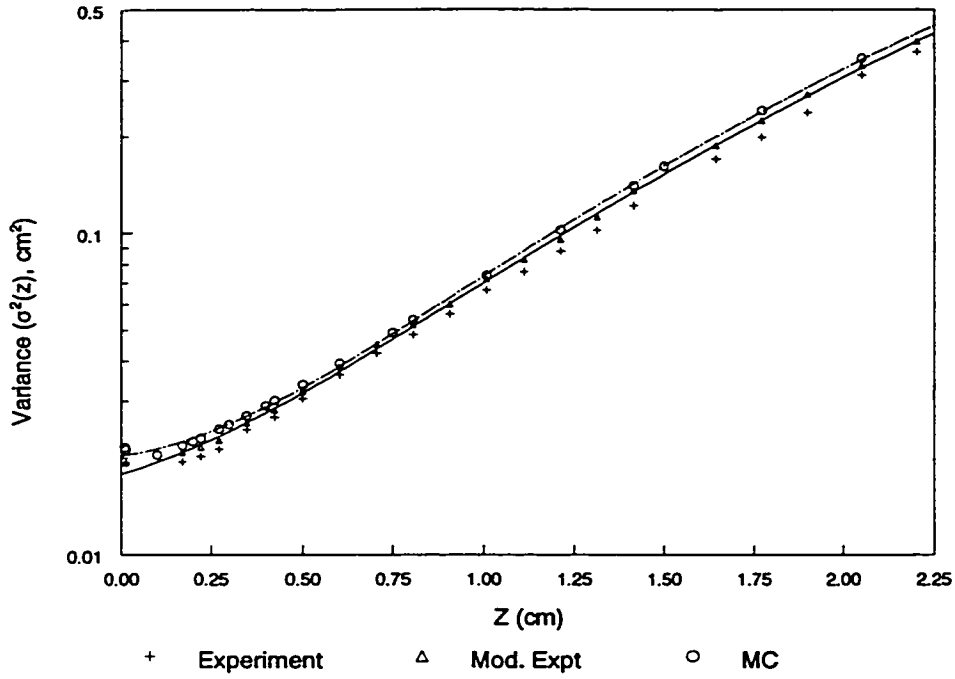

Figure 7.12 Comparison of variance as a function of depth among experimental, MC, and modified experimental data. Shown also are the fitted lines to the modified experimental (solid) and the MC (dash-dot) data

Figure 7.12 displays a comparison of the variance as a function of depth among the experimental data, shown earlier in Figure 6.20, the MC data, which were computed in the same manner as the experimental data, and the modified experimental data, which will be described later. The polynomial fitted curves of the MC and modified experimental data up to their inflection points are also shown. But the fits will be described in the next subsection. The MC values are higher than the experimental values by about 10% at small z, i.e. near the beam entrance, up to a maximum difference of about 20% at $z \sim 1.8$ cm. This revelation is somewhat unexpected because the experimental and MC lateral dose distributions agree very well near the beam entrance except at the tail end, where the experimental data are slightly higher than the MC values.

Since the computation of the variance is highly sensitive to the lateral tail end dose (see equation (6.22)), one would expect the converse to be true. However, it turns out the main reason is that the combination of the sensitivity of the radiochromic film used in the electron irradiation and the background subtraction method results in very poor accuracy below about 0.5 Gy. Consequently, the tail end dose regions were not used in computing the experimental variances, thus lowering their actual values slightly. It should be noted that if a sufficiently large number of dose points on the lateral distribution are used, the calculated variance would become very insensitive to the number of points. To correct for this systematic error, the Monte Carlo data were spline fitted to provide the lateral dose distribution values at the same depths as the experimental data. Then, neglecting the same tail dose regions as the experimental data, modified MC variances were computed. The modified experimental variances were subsequently obtained by multiplying the ratio of the MC variance to the modified MC variance at each depth. This ratio ranges from about 1.05 to 1.14. The modified experimental variances are closer to their corresponding MC values and are lower by only 2 to 10%. The original experimental variances will not be used in any further calculations or discussion since they are not as accurate as the modified values.

One anomalous phenomenon is observed near the beam entrance for the MC data. The variance at $z = 0.01$ cm is actually about 5.6% larger than that at $z = 0.1$ cm. This reverse characteristic is not expected. But it is likely due to an increase in dose deposited at the tail end of the lateral dose distribution by the Bremsstrahlung photons and short-ranged secondary electrons produced by the beam interaction with the stainless steel exit

window. This phenomenon is not observed in the modified experimental data, however, possibly because of the limit of the experimental precision.

7.4.7 Linear scattering power of electron beam

The scattering of the electron beam within the Lucite phantom can also be examined by determining the linear scattering power, $T(z)$, which has been described in Section 2.5.4. It is defined as the rate of increase of the variance in the angular distribution with distance z. This angular distribution, $\theta(z)$, measured from the initial beam direction, represents the angular spread of the beam at distance z. The angular spread is related to the variance of the radial distribution, $\overline{r^2}(z)$. If the beam is assumed to be narrow and has a cross section with a Gaussian distribution, the variance of the radial distribution is related to the scattering power by (ICRU 1984a),

$$\overline{r^2}(z) = \overline{r_i^2} + 2\overline{r\theta_i}z + \overline{\theta_i^2}z^2 + \int_0^z (z-u)^2 T(u)du\,, \tag{7.4}$$

where $\overline{r_i^2}$ is the initial variance of the radial distribution, $\overline{\theta_i^2}$ is the mean initial variance of the angular distribution, and $\overline{r\theta_i}$ is the initial covariance of the simultaneous radial and angular distribution of the beam, incident on the plane $z = 0$. Appendix B shows that the linear scattering power can be determined by,

$$T(z) = \frac{1}{2}\frac{d^3}{dz^3}\overline{r^2}(z)\,. \tag{7.5}$$

Note that the variance of the radial distribution of a pencil beam can be calculated by equation (2.27) and is equal to $A_2(z)$, which is identical to the fourth term in equation (7.4). Since the angular spread of the beam is symmetric, the variance of the radial distribution, $\overline{r_i^2}$, is the variance of the lateral distribution, $\sigma^2(z)$, of the $\dot{d}(x')$ at depth z.

The linear scattering power can, in theory, be determined by fitting the measured $\sigma^2(z_j)$ to an analytic function and then finding its third derivative as in equation (7.4). However, the third derivative of the fitted function is extremely sensitive to the uncertainties in the fitting parameters. Therefore, a polynomial function was first assumed in $T(z)$. After numerous trials and errors, and with the aid of the theoretical function in equation (2.20), it was determined that a second-order polynomial in the following form,

$$T(z) = a_0 + a_1(z + a_3) + a_2(z + a_3)^2, \tag{7.6}$$

was adequate. Then, a fitting function for the $\sigma^2(z_j)$, which must satisfy equation (7.5), was searched. This fitting function must also only contain the 4 free parameters, a_i (i = 1, 2, and 3), in the above equation so as to reduce the sensitivity of the uncertainties in the fitting parameters. Finally, a relatively simple function in the form of,

$$\sigma^2(z) = \frac{a_0}{3}(z + a_3)^3 + \frac{a_1}{12}(z + a_3)^4 + \frac{a_2}{30}(z + a_3)^5, \tag{7.7}$$

appeared to be suitable. Figure 7.12 displays the results of the polynomial fit to the variance of the lateral distribution as a function of depth for both the experimental and MC data. The fit was only performed up to the inflection point at about z = 2.2 cm

because the approach used neglects the finite electron range effects; otherwise, the variance in the lateral distribution would have increased indefinitely.

The results of the polynomial fit of the $\sigma^2(z)$, along with the variances and covariances of the fitting parameters, for both the modified experimental (column 2) and MC data (column 3) are shown in Table 7.3. Substituting the fitting parameters into equation (7.6), the linear scattering power was evaluated for both sets of data. The uncertainties in $T(z)$ was calculated by utilizing the general error propagation equation (Bevington and Robinson 1992 (Chap 3)) using both the variances and covariances of the fitting parameters:

$$\delta(T) = \sqrt{\sum_{i=0}^{3}\left(\frac{\partial T}{\partial a_i}\right)^2 \delta^2(a_i) + \sum_{i=0}^{3}\sum_{j>i}^{3} \frac{\partial T}{\partial a_i}\frac{\partial T}{\partial a_i}\delta^2(a_i a_j)}\,, \tag{7.8}$$

where $\delta^2(a_i)$ is the variance or the square of the standard error in the fitting parameter a_i, $\delta^2(a_i a_j) = \delta^2(a_j a_i)$ is the covariance of the fitting parameters a_i and a_j, and

$$\frac{\partial T}{\partial a_0} = 1, \quad \frac{\partial T}{\partial a_1} = z + a_3, \quad \frac{\partial T}{\partial a_2} = (z + a_3)^2, \quad \frac{\partial T}{\partial a_3} = a_1 + 2a_2(z + a_3). \tag{7.9}$$

Fitting Parameters	Experiment (modified)	MC
a_0 (cm^{-1})	1.462×10^{-02}	1.716×10^{-02}
a_1 (cm^{-2})	-2.800×10^{-02}	-2.666×10^{-02}
a_2 (cm^{-3})	8.918×10^{-03}	6.669×10^{-03}
a_3 (cm)	3.921	4.914
$\delta^2(a_0)$	7.621×10^{-08}	1.278×10^{-08}
$\delta^2(a_0a_1)$	1.352×10^{-08}	-5.309×10^{-08}
$\delta^2(a_0a_2)$	-6.757×10^{-08}	2.232×10^{-08}
$\delta^2(a_0a_3)$	2.459×10^{-05}	-7.053×10^{-06}
$\delta^2(a_1)$	1.748×10^{-06}	3.920×10^{-07}
$\delta^2(a_1a_2)$	-1.252×10^{-06}	-1.826×10^{-07}
$\delta^2(a_1a_3)$	3.050×10^{-04}	6.396×10^{-05}
$\delta^2(a_2)$	9.409×10^{-07}	8.614×10^{-08}
$\delta^2(a_2a_3)$	-2.354×10^{-04}	-3.050×10^{-05}
$\delta^2(a_3)$	5.973×10^{-02}	1.090×10^{-02}

Table 7.3 Polynomial fitting results of $\sigma^2(z)$

The calculated linear scattering power as a function of depth is displayed in Figure 7.13 for both the modified experimental and MC results, along with theoretical data listed in the ICRU report 35 (ICRU 1984a) and data obtained by equation (2.20) given in the ICRU report 56 (ICRU 1997). The theoretical data were given or computed as a function of energy. Hence, the Harder's formula of equation (A.6) (Harder 1965) was used to convert the dependence from energy to depth. The MC values are about 12% larger than the modified experimental data near the beam entrance. But unlike the variances (see Figure 7.12), where the MC values are consistently higher than the experimental data up to the inflection point ($z \sim 2.2$ cm), the two $T(z)$ curves converge gradually until about $z =$ 0.9 cm, where they begin to diverge. At $z = 2.2$ cm, the MC $T(z)$ is about 7% smaller than the modified experimental value. The two sets of theoretical data differ by the choice of

the screening angle (see equation (2.21)), and the ICRU 56 data appear to be larger than the ICRU 35 data by a constant factor of approximately 16%. It is not known which screening angle is supposed to give a more accurate evaluation.

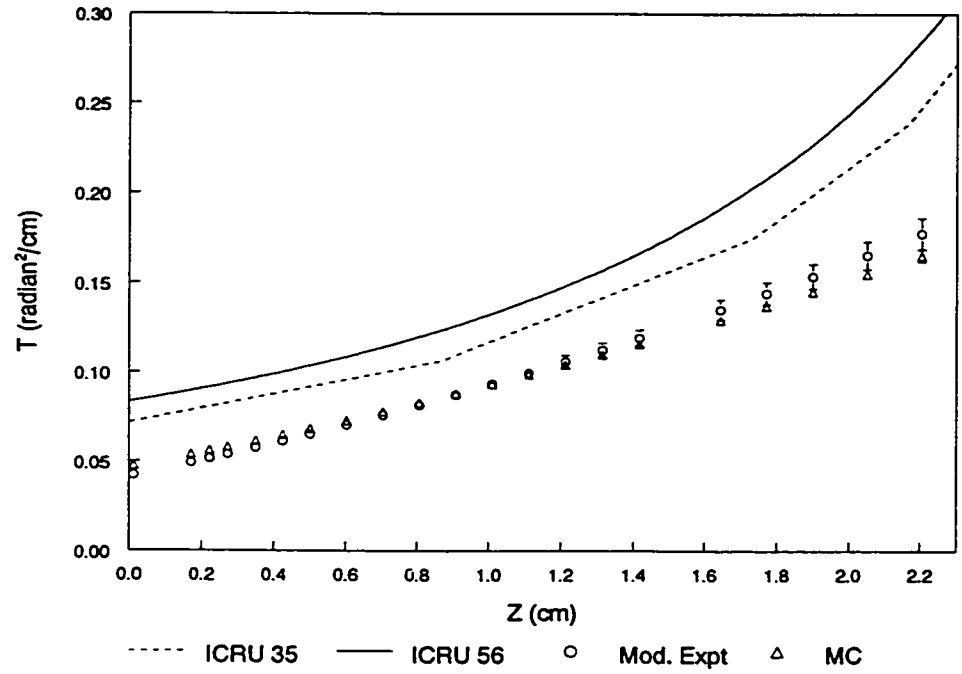

Figure 7.13 Comparison of linear scattering power as a function of depth for experimental data, MC data, and theories

Both the MC and modified experimental data are significantly lower than the theoretical data from the ICRU 35 and 56. In fact, the ICRU 35 values are larger than the corresponding modified experimental values by as much as a factor of 1.8. It should be stressed that the theoretical $T(z)$ assumes only primary electrons are involved in the scattering, and the spin and relativistic effects of the electrons are not included. The MC and experimentally evaluated $T(z)$, however, include the spin and relativistic effects and

contributions from secondary electrons and Bremsstrahlung photons. Generally, primary electrons are more forward scattered than secondary electrons at a given depth. But the neglect of the relativistic effects in the theories implies that the electrons would be less forward scattered. Furthermore, the effect of the spin neglection is not known. At larger z, the angular spread is further complicated by the fact that the secondary electrons tend to have a shorter range than their primary counterparts. The combined effects may either increase or decrease the theoretical $T(z)$ values. However, the experimental finding is consistent with that reported by Vilches *et al.* (1999), who have obtained values of the linear scattering power in air at mean beam energy between 5 and 11 MeV larger than those quoted in the ICRU 35 by a factor of ~ 2.

The advantage of using equation (7.5) to determine the linear scattering power is that the first three terms in equation (7.4) all disappear after the third derivative. Therefore, the linear scattering power is independent of the initial lateral variance, the initial angular variance, and the initial lateral and angular covariance of the beam. However, it is also important to examine these parameters by evaluating the values of these three terms. The evaluation was performed to both the modified experimental and the MC variances using the following method. It involves calculating the constants in the z^0, z^1, and z^2 terms for the fitted variance equation in (7.7), and then identifying them with the first three terms of equation (7.4). Using simple algebra, it was determined that,

$$\overline{r_i^2} = \frac{1}{3}a_0 a_3^3 + \frac{1}{12}a_1 a_3^4 + \frac{1}{30}a_2 a_3^5, \tag{7.10}$$

$$\overline{r\theta_i} = \frac{1}{2}a_0 a_3^2 + \frac{1}{6}a_1 a_3^3 + \frac{1}{12}a_2 a_3^4, \tag{7.11}$$

and,

$$\overline{\theta_i^2} = a_0 a_3 + \frac{1}{2}a_1 a_3^2 + \frac{1}{3}a_2 a_3^3. \tag{7.12}$$

As mentioned earlier in Section 7.4.6, the initial MC variance is unexpectedly higher than that at z = 0.1 cm. Although this anomaly is not observed in the modified experimental data, the trend of the modified experimental curve suggests a potential presence of this anomaly. If this anomaly is believed to be the result of the beam interaction with the stainless steel exit window, the irregular points should be ignored in determining the intrinsic beam characteristics. Therefore, the MC and modified experimental variance distributions in Figure 7.12 were refitted without the initial irregular points. The refitting results are displayed in Figure 7.14. The initial characteristics of the beam were then obtained using the above equations on both the originally fitted MC and experimental variance distributions, shown in Figure 7.12, and the refitted distributions. These results are summarized in Table 7.4.

	Experiment (modified)		MC	
	Original Fit	**Refit**	**Original Fit**	**Refit**
$\overline{r_i^2}$ (cm^2)	0.018±0.028	0.017±0.011	0.020±0.029	0.018±0.007
$\overline{r\theta_i}$ (radian-cm)	0.014±0.034	0.018±0.018	0.008±0.027	0.016±0.011
$\overline{\theta_i^2}$ (radian^2)	0.022±0.017	0.018±0.013	0.026±0.010	0.019±0.007

Table 7.4 Calculated initial radial variance, initial angular and radial covariance, and initial angular variance

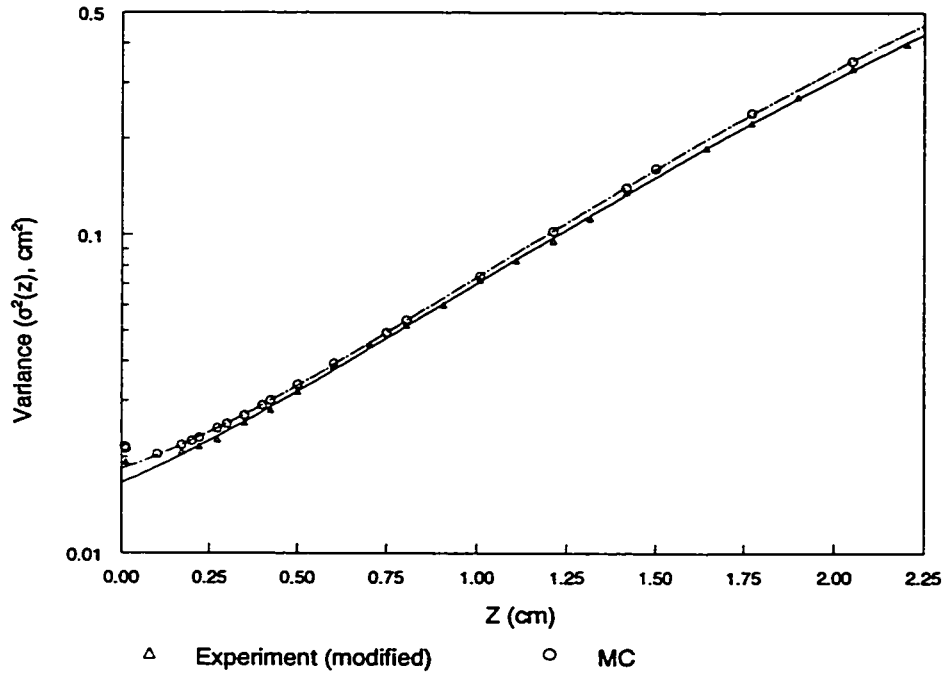

Figure 7.14 Refitted curves to modified experimental (solid) and MC (dash-dot) variances as a function of depth

The initial radial variance (first entry in the first column of the Table) is related to the beam width at the beam entrance of the phantom. As expected, the refitted values are smaller than the originally fitted values. The beam width is estimated to have a radius of 0.15 cm (Klassen and Ross 1997). Assuming the radius is the half width at the half maximum of the peak of the lateral cross sectional beam profile, the variance is equal to the square of the radius divided by a factor of 2ln(2). Therefore, the expected initial radial variance is 0.016 cm^2, which agrees with all the modified experimental and MC values.

The initial angular variance (third entry in the first column) gives information on the amount of divergence of the beam. Again, the refitted values are smaller than the

originally fitted values. The component due to the stainless steel window scattering is related to the linear scattering power by,

$$\overline{\theta_i^2} = \Delta\overline{\theta^2}(0) = T(0)\Delta z\,, \tag{7.13}$$

where Δz is window thickness, and $T(0)$ is the linear scattering power, calculated using equation (2.20) obtained from the ICRU 56, of the stainless steel, which was assumed to be made of iron. The initial angular variance component due to the window scattering was then calculated to be 0.022 radian^2. Since the theoretical $T(0)$ has been found to be about twice as large as the modified experimental value, the initial angular variance component is probably only 0.011 radian^2. This value is smaller than all the modified experimental and the MC values. This disagreement is expected since the above calculation neglects the component due to the inherent divergence of the beam itself, which can be a significant factor.

The initial angular and lateral covariance (second entry in the first column) tells how the angular and lateral spread of the beam depend on each other. But it is not known how to find an independent expected value for it. The experimental value from the original fit is about twice as large as the respective MC value. But the corresponding values obtained from the refit show a much smaller discrepancy.

CHAPTER 8

CONCLUSIONS

In this thesis, the dose distribution by β particles and high energy electrons has been investigated through the use of the the McMaster Dose Imaging System and the radiochromic film (Gafchromic Dosimetry Media, MD-55-2). The investigation entailed the commissioning of the microspectrophotometer and the exploration of the newly proposed interpolating-spline fitting and χ^2 minimization method in film calibration. Then four separate experiments involving irradiation in various geometries were performed. The results from these experiments were compared with expected data, theories, or Monte Carlo simulation results.

The first experiment was performed to irradiate uniformly a set of 11 films for calibration by a ^{60}Co γsource. The films were given a dose to water ranging from 0.33 to 222.57 Gy. The irradiated films were subsequently utilized to provide calibration data for other experiments and to examine the proposed method of film calibration in conjunction with the second experiment. This method involved spline fitting the optical density as a function of both wavelength and dose of the calibration data. An unknown dose to a film could then be determined by minimizing the χ^2 between the measured optical density as a function of wavelength and the spline fitted calibration data. The feasibility of this

method was vigorously tested using manipulated experimental data. It was found that the method provided excellent precision and accuracy.

The second experiment involved irradiating uniformly a set of 11 films, placed in a specially designed irradiation facility, by a ^{32}P volume source. The expected dose (to water) given to the films was calculated by the β counting method based on the equilibrium geometry. The dose was corrected for the loss due to the attenuation of the film substrate and various media between the source and the film. The overall dose loss correction factor was calculated to be 20.67%, while the correction factor due to the film substrate was 20%. The substrate correction factor is close to the value of about 17% obtained by Fox *et al.* (1999) using a different method. Although the small discrepancy may indicate a need to refine the calculation techniques involved, the closeness of the values also validates the method utilized. The measured dose deposited in the films was determined by the optical density of the films and the interpolating-spline fitting and χ^2 minimization method using the ^{60}Co calibration data from the first experiment. It was found that the minimum measurable dose limit was about 0.5 Gy, and the measured dose had a precision of better than 3% for most of the points above the minimum measurable dose. The measured dose was then compared to the expected dose by plotting them against each other. A linear relationship between them was obtained: the slope and the intercept were found to be essentially 1 and 0, respectively. The root mean square relative deviation between them was found to be about 3.5% above the minimum measurable dose limit. This level of accuracy, however, was obtained with limited or no control of various external factors that can affect the film response. Therefore, the

methodology was proven to be successful. In addition, it also extended the useable dose range of the radiochromic films to between 0.5 Gy and beyond 212 Gy. As a result, the McMaster Dose Imaging System and the radiochromic films can be used to measure dose distribution in more complicated geometries.

The success of the methodology led to two more experiments. The third experiment was the volume ^{32}P β irradiation to a film embedded edge-on in a Lucite block to examine the beta depth dose distribution. Two trials were carried out. It was found that for the most part, the two experimental dose distributions differed by less than 10%. This relatively large deviation between the two trials indicates that perhaps a change in the experimental design is needed to better control various systematic errors. The distributions were compared with Monte Carlo simulation, which is in close agreement with the results from the first trial up to a depth of 3 mm. But beyond this depth, the Monte Carlo data appear to be significantly lower than the experimental values. This lack of agreement requires further investigation.

The dose distribution due to the 10 MeV electron beam irradiation to a film embedded in a Lucite phantom completed the final experiment. Three films were exposed for various exposure periods. The lateral and depth dose distributions were reconstructed using the measured data from all three films. During the reconstruction, it was discovered that the centroid of the lateral distribution for all three films varied with depth. The reason for this depth dependence is not certain, and the potential presence of a secondary peak or a beam deflection due to an external magnetic field has been speculated. The reconstructed lateral dose distributions appear to be almost Gaussian,

which is consistent with many other published studies. The experimental lateral dose distribution compared favorably with the Monte Carlo data, except at the lateral tail end, up to a depth of about 20 mm. Beyond this depth, the experimental lateral dose distribution appears to be consistently higher than that of the Monte Carlo simulation. These discrepancies are consistent with the ^{32}P edge-on irradiation, and may actually indicate real disagreement between the experimental and Monte Carlo data. If so, this disagreement is not too surprising because the Monte Carlo simulation uses certain approximations, such as the use of a "condensed random walk" model rather than a direct simulation of every collision. Further investigation under better-controlled external variables and using more uniform films should be conducted.

The lateral spread of the electron beam was also examined by calculating the lateral variance of the dose distribution as a function of depth. The Monte Carlo variance distribution was found to be 2 to 10% higher than the experimental values up to a depth of about 2.2 cm. From the variance distribution, the linear scattering power as a function of depth was evaluated for both the experimental and Monte Carlo results. Both sets of results were compared to theoretical data obtained from the ICRU report 35 and the ICRU report 56. It was found that the ICRU 56 values are approximately 16% larger than the ICRU 35 values, and the ICRU 35 values are larger than the experimental and Monte Carlo values by a factor of as much as 1.8. The disagreement is consistent with the findings by Vilches *et al.* (1999), who obtained values of the linear scattering power in air smaller than the ICRU 35 data by a factor of about 2. This indicates that the values in the ICRU reports are probably too high. The initial beam characteristics were also examined

by fitting the experimental variance as a function of depth. The initial radial variance, the initial angular and radial convariance, and the initial angular variance of the beam were determined. The initial radial variance of about 0.017 cm^2 and the initial angular variance of about 0.018 $radian^2$ were compared with expected values and were found to be in reasonably good agreement.

Future work may include the continuation and expansion of the research described in this thesis, in particular, the investigation of dose distribution in heterogeneous phantoms and dose perturbation at and near the heterogeneous interface. It is hoped the research will soon expand into cancer treatment, nuclear medicine, and radiology etc, where accurate and precise dose measurements in human organs and tissues are often required. In addition, work is underway to improve the readout time of the McMaster Dose Imaging System.

APPENDIX A

DEFLECTION OF ELECTRON BEAM DUE TO AN EXTERNAL MAGNETIC FIELD

Magnetic fields can affect the motion of charged particles by deflecting their paths. If a uniform field perpendicular to the direction of the particles is assumed, then the motion of the charged particles is a circular path, and the radius of curvature can be evaluated by equating the magnetic force acting on the particle with the force of centripetal acceleration. However, for electrons, there are generally two problems that can complicate the particle motion. First, electrons can lose a large fraction of their kinetic energy as they travel within a medium. As a result, the amount of deflection in the path changes accordingly, and the motion is no longer circular. Second, if the energy of the incident electrons is high (of the order of MeV), the motion must be calculated using relativistic force laws.

The radius of curvature can be calculated as follows. The magnetic force, $\bar{F}$, acting on an electron is,

$$\bar{F} = e\bar{u} \times \bar{B}\,, \tag{A.1}$$

where e is the electron charge, $\bar{u}$ is the velocity of the electron, and $\bar{B}$ is the magnetic field. If the magnetic field is assumed to be uniform, and, for simplicity, the field is always perpendicular to the path of the electron, then the magnetic force must be equal to the force of the centripetal acceleration of the electron, thus yielding,

$$euB = \frac{mu^2}{r}, \tag{A.2}$$

where r is the radius of curvature, and m is the relativistic mass, which is related to the electron rest mass m_0 by,

$$m = \frac{m_0}{\sqrt{1 - \frac{u^2}{c^2}}}, \tag{A.3}$$

where c is the speed of light. Equation (A.2) can be simplified and rewritten as,

$$r = \frac{mu}{eB} = \frac{p}{eB}, \tag{A.4}$$

where p is the relativistic momentum. It is related to the kinetic energy, E, of the electron by,

$$p = \frac{1}{c}\sqrt{(E + m_0c^2)^2 - (m_0c^2)^2}\ . \tag{A.5}$$

This equation can be derived from (A.3) by identifying the total energy, i.e. kinetic and rest mass energy, to be mc^2. In addition, if the CSDA is assumed, the kinetic energy is related to the path length, l, of the electron by the Harder's formula (Harder 1965),

$$E = E_0\left(1 - \frac{l}{R}\right), \tag{A.6}$$

where E_0 is the initial electron energy, and R is the range of the electron. Combining equations (A.4), (A.5), and (A.6), the radius of curvature as a function of the electron path length is,

$$r(l) = \frac{1}{eBc}\sqrt{\left[E_0\left(1 - \frac{l}{R}\right) + m_0c^2\right]^2 - (m_0c^2)^2}\ . \tag{A.7}$$

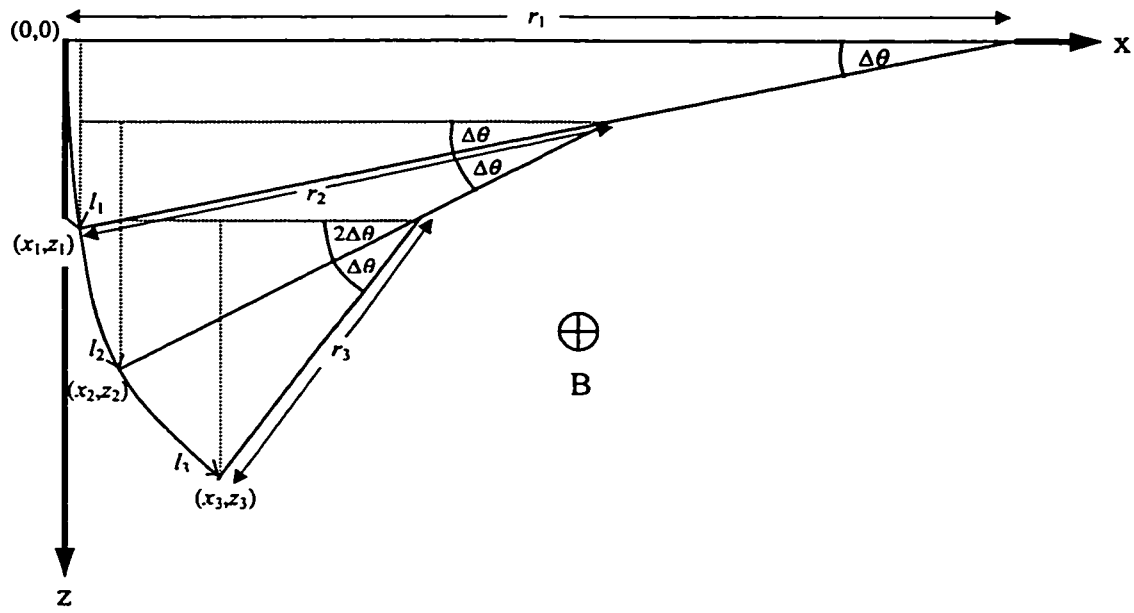

Figure A.1 Diagram of electron beam path deflected by a magnetic field

Figure A.1 shows a diagram of the path of an electron beam in a medium deflected only by a uniform magnetic field (into the page). In other words, the path is equivalent to the centroid position of a scattered beam as a function of depth. The beam enters normal to the medium at the origin (0,0) in the positive z-direction. The motion is governed by the radius of curvature, $r(l)$, such that the path is always perpendicular to the radius. Note that $\Delta\theta$ is taken to be infinitesimally small. As the beam travels by a small increment, $\Delta l = r(l)\Delta\theta$, it loses energy, thus altering the value of $r(l)$. Therefore, $r(l)$ needs to be recalculated for the next increment to obtain a new direction of the beam. Hence, the position of the beam in the medium at any coordinate, (x_n,z_n), can be

determined by its previous position, (x_{n-1},z_{n-1}). For the position (x_1,z_1) on the diagram, the coordinates can be determined by simple trigonometry:

$$\begin{aligned} x_1 &= r_1(0) - r_1(0)\cos(\Delta\theta), \\ z_1 &= r_1(0)\sin(\Delta\theta), \\ l_1 &= r_1(0)\Delta\theta. \end{aligned} \tag{A.8}$$

For (x_2,z_2),

$$\begin{aligned} x_2 &= x_1 + r_2(l_1)\cos(\Delta\theta) - r_2(l_1)\cos(\Delta\theta + \Delta\theta), \\ z_2 &= z_1 + r_2(l_1)\sin(\Delta\theta + \Delta\theta) - r_2(l_1)\sin(\Delta\theta), \\ l_2 &= l_1 + r_2(l_1)\Delta\theta. \end{aligned} \tag{A.9}$$

For (x_3,z_3),

$$\begin{aligned} x_3 &= x_2 + r_3(l_2)\cos(2\Delta\theta) - r_3(l_2)\cos(3\Delta\theta), \\ z_3 &= z_2 + r_3(l_2)\sin(3\Delta\theta) - r_3(l_2)\sin(2\Delta\theta), \\ l_3 &= l_2 + r_3(l_2)\Delta\theta. \end{aligned} \tag{A.10}$$

Therefore, for any (x_n,z_n),

$$\begin{aligned} x_n &= x_{n-1} + r_n(l_{n-1})\big(\cos((n-1)\Delta\theta) - \cos(n\Delta\theta)\big), \\ z_n &= z_{n-1} + r_n(l_{n-1})\big(\sin(n\Delta\theta) - \sin((n-1)\Delta\theta)\big), \\ l_n &= l_{n-1} + r_n(l_{n-1})\Delta\theta. \end{aligned} \tag{A.11}$$

The electron beam path was computed numerically using equations (A.7) and (A.11). Figure A.2 shows the beam path from the numerical calculation results generated by a uniform magnetic field of $B = 3\times10^{-2}$ T, perpendicular to the electron path, using a step size of $\Delta\theta = 10^{-4}$ radians, along with the experimental data from Figure 6.11 for film 2. Note that if the field were parallel to the film placement in the Lucite phantom, the deflection would not be observed.

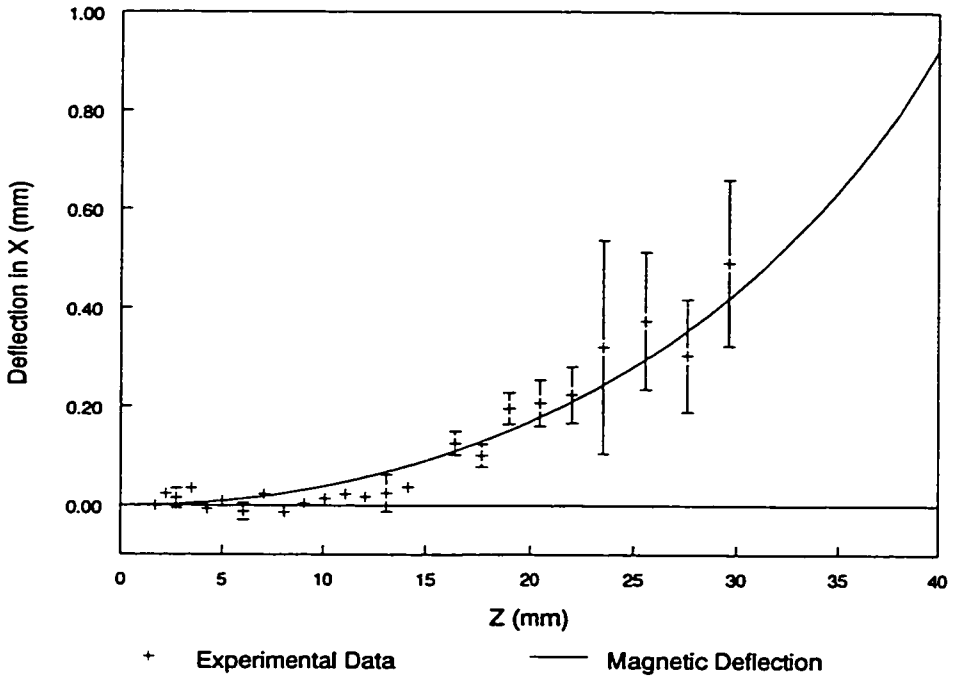

Figure A.2 Comparison of electron beam path between experimental data for film 2 and theoretical calculation

APPENDIX B

MATHEMATICAL DERIVATION

In this appendix, equation (7.5) will be derived from equation (7.4). There are various ways to perform the derivation, such as taking the derivatives directly from first principle, or solving the integral by parts in the fourth term of equation (7.4) before taking the derivatives. For simplicity, the derivation is restricted to the fourth term of (7.4) since the first three terms contain z of second order or less and will all disappear after the third derivative.

The derivation will be carried out by applying the first principle. Let I_4 be the fourth term of equation (7.4):

$$I_4(z) = \int_0^z (z-u)^2 T(u)du\,. \tag{B.1}$$

By definition, the derivative of $I_4(z)$ is,

$$\frac{d}{dz} I_4(z) = \lim_{\Delta z \to 0} \frac{I_4(z+\Delta z) - I_4(z)}{\Delta z}, \tag{B.2}$$

$$= \lim_{\Delta z \to 0} \frac{1}{\Delta z} \left[\int_0^{z+\Delta z} (z+\Delta z-u)^2 T(u)du - \int_0^z (z-u)^2 T(u)du \right]. \tag{B.3}$$

Expanding the square term in the first integral above and discarding the second order Δz term,

$$\frac{d}{dz}I_4(z) = \lim_{\Delta z\to 0}\frac{1}{\Delta z}\left[\int_0^{z+\Delta z}(z-u)^2T(u)du + 2\Delta z\int_0^{z+\Delta z}(z-u)T(u)du - \int_0^{z}(z-u)^2T(u)du\right] \quad \text{(B.4)}$$

$$= \lim_{\Delta z\to 0}\frac{1}{\Delta z}\int_z^{z+\Delta z}(z-u)^2T(u)du + \lim_{\Delta z\to 0}\frac{1}{\Delta z}2\Delta z\int_0^{z+\Delta z}(z-u)T(u)du. \quad \text{(B.5)}$$

Now, the first integral in the above equation can be simplified by using the Mean Value Theorem (MVT) for definite integrals. The MVT states that if a function, $f(x)$, is continuous in $a \le x \le b$, then there exists a value, c, between a and b such that,

$$\int_a^b f(x)dx = (b-a)f(c). \quad \text{(B.6)}$$

Therefore, using the MVT, the first integral term in (B.5) becomes,

$$\begin{aligned}\lim_{\Delta z\to 0}\frac{1}{\Delta z}\int_z^{z+\Delta z}(z-u)^2T(u)du &= \lim_{\Delta z\to 0}\frac{1}{\Delta z}(z+\Delta z-z)(z-u')^2T(u'),\\ &= \lim_{\Delta z\to 0}(z-u')^2T(u'),\end{aligned} \quad \text{(B.7)}$$

where $z \le u' < z+\Delta z$. As $\Delta z \to 0$, $u' \to z$; therefore, the first term goes to zero. The second integral term in (B.5) is trivial. As a result, equation (B.5) becomes,

$$\frac{d}{dz}I_4(z) = 2\int_0^z(z-u)T(u)du. \quad \text{(B.8)}$$

The second derivative can be derived in a similar manner as the first. Using equation (B.2),

$$\frac{d^2}{dz^2}I_4(z) = 2\lim_{\Delta z\to 0}\frac{1}{\Delta z}\left[\int_0^{z+\Delta z}(z+\Delta z-u)T(u)du - \int_0^{z}(z-u)T(u)du\right] \quad \text{(B.9)}$$

$$= 2\lim_{\Delta z\to 0}\frac{1}{\Delta z}\int_z^{z+\Delta z}(z-u)T(u)du + 2\lim_{\Delta z\to 0}\frac{1}{\Delta z}\Delta z\int_0^{z+\Delta z}T(u)du. \quad \text{(B.10)}$$

Again, by the MVT, the first integral term in the above equation vanishes. Hence, equation (B.10) becomes,

$$\frac{d^2}{dz^2} I_4(z) = 2\int_0^z T(u)du \,. \tag{B.11}$$

The third derivative can again be derived using equation (B.2). In a similar manner as before,

$$\frac{d^3}{dz^3} I_4(z) = 2 \lim_{\Delta z \to 0} \frac{1}{\Delta z} \int_z^{z+\Delta z} T(u)du \,. \tag{B.12}$$

Using the MVT, equation (B.12) becomes,

$$\frac{d^3}{dz^3} I_4(z) = 2 \lim_{\Delta z \to 0} \frac{1}{\Delta z} T(u')\Delta z = 2T(z). \tag{B.13}$$

Finally, rearranging the above equation yields,

$$T(z) = \frac{1}{2} \frac{d^3}{dz^3} I_4(z). \tag{B.14}$$

REFERENCES

Aluffi-Pentini F, Parisi V, and Zirilli F. 1988. Algorithm 667: Sigma – a stochastic-integration global minimization algorithm. *Collected Algorithms from ACM 14(4): 366-388.* New York: Association for Computing Machinery.

Andreo P. 1988. Stopping-power ratios for dosimetry. *Monte Carlo Transport of Electrons and Photons 38: 485-501.* eds. Jenkins T M, Nelson W R, Rindi A. New York: Plenum Press.

Attix F H. 1986. *Introduction to Radiological Physics and Radiation Dosimetry.* New York: John Wiley and Sons.

Berger M J. 1963. Monte Carlo calculation of the penetration and diffusion of fast charged particles. *Methods in Computational Physics 1, Advances in Research and Applications: 135-215.* eds. Alder B, Fernbach S, and Rotenberg M. New York: Academic Press.

Berger M J and Wang R. 1988. Multiple-scattering angular deflections and energy-loss straggling. *Monte Carlo Transport of Electrons and Photons 38: 21-56.* eds. Jenkins T M, Nelson W R, Rindi A. New York: Plenum Press.

Bethe H and Ashkin J. 1953. Passage of radiations through matter. *Experimental Nuclear Physics 1: 166-357.* ed. Segrè E. New York: John Wiley and Sons.

Bethe H A, Rose M E, and Smith L P. 1938. The multiple scattering of electrons. *Proceedings of the American Philosophical Society 78: 573-585.*

Bevington P R and Robinson D K. 1992. *Data Reduction and Error Analysis for the Physical Sciences, 2nd Edition.* New York: McGraw-Hill.

Bichsel H. 1968. Charged-particle interactions. *Radiation Dosimetry, 2nd edition 1: 157-228.* eds. Attix F H, Roesch W C, Tochilin E. New York: Academic Press.

Birkoff, R D. 1958. The passage of electrons through matter. *Handbuch der Physik 34: 53-138.* ed. Flügge S. Berlin: Springer-Verlag.

Börgers C and Larsen E W. 1994. Fokker-Planck approximation of monoenergetic transport processes. *Transactions of the American Nuclear Society 71: 235-236.*

Börgers C and Larsen E W. 1996a. Asymptotic derivation of the Fermi pencil-beam approximation. *Nuclear Science and Engineering 123: 343-357.*

Börgers C and Larsen E W. 1996b. On the accuracy of the Fokker-Planck and Fermi pencil beam equations for charged particle transport. *Medical Physics 23(10): 1749-1759.*

Brahme A. 1985. Current algorithms for computed electron beam dose planning. *Radiotherapy and Oncology: Journal of the European Society for Therapeutic Radiology and Oncology 3(4): 347-362.*

Brahme A, Lax I, and Andreo P. 1981. Electron beam dose planning using discrete Gaussian beams: Mathematical background. *Acta Radiologica. Oncology 20: 147-158.*

Briesmeister J F. 1997. *MCNP – a general Monte Carlo N-particle transport code 4B. Report LA-12625.* Los Alamos, New Mexico: Los Alamos National Laboratory.

Butson M and Yu P K N. 1998. Letter to the Editor: Comments on "Quantitative evaluation of radiochromic film response for two-dimensional dosimetry". *Medical Physics 25(5): 793.*

Butson M J, Yu P K N, and Metcalfe P E. 1998. Effects of read-out light sources and ambient light on radiochromic film. *Physics in Medicine and Biology 43: 2407-2412.*

Chiu-Tsao S-T, de la Zerda A, Lin J, and Kim J H. 1994. High-sensitivity GafChromic film dosimetry for ^{125}I seed. *Medical Physics 21(5): 651-657.*

Chu R D H, Van Dyk G, Lewis D F, O'Hara K P J, Buckland B W, and Dinelle F. 1990. GafChromic™ Dosimetry Media: A new high dose, thin film routine dosimeter and dose mapping tool. *Radiation Physics and Chemistry 35(4-6): 767-773.*

Cross W G, Freedman N O, and Wong P Y, 1992. *Tables of Beta-ray Dose Distributions in Water. AECL Report, AECL-10521.* Chalk River, Ontario: Atomic Energy of Canada Limited.

Dierckx P. 1993. *Curve and Surface Fitting with Splines.* Oxford: Oxford University Press.

Evans R D. 1955. *The Atomic Nucleus, International series in pure and applied physics.* New York: McGraw-Hill.

Eyges L. 1948. Multiple scattering with energy loss. *Physical Review 74: 1534-1535.*

Firestone R B, Shirley V S, Baglin C M, Chu S Y F, and Zipkin J, 1996. *Table of Isotopes, 8th Edition.* New York: John Wiley & Sons.

Fairman R M, 1998. International Specialty Products, 1361 Alps Road, Wayne, New Jersey, 07470. Personal communication.

Farrell T. 1999. Hamilton Regional Cancer Center, 999 Concession Street, Hamilton, Ontario. Personal communication.

Fox R A, Barker P, and Smart G. 1999. The use of GAFchromic film to determine the absolute activity of beta emitters. *Physics in Medicine and Biology 44(4): 833-842.*

Glastone S and Edlund M C. 1952. *The Element of Nuclear Reactor Theory.* Princeton, New Jersey: Van Nostrand.

Goudsmit S and Saunderson J L. 1940. Multiple scattering of electrons. *Physical Review 57: 24-29.*

Halbleib J. 1988a. Structure and operation of the ITS code system. *Monte Carlo Transport of Electrons and Photons 38: 249-262.* eds. Jenkins T M, Nelson W R, Rindi A. New York: Plenum Press.

Halbleib J. 1988b. Applications of the ITS codes. *Monte Carlo Transport of Electrons and Photons 38: 263-284.* eds. Jenkins T M, Nelson W R, Rindi A. New York: Plenum Press.

Harder D. 1965. Energiespektren schneller elektronen in verschiedenen tiefen. *Symposium on High-energy Electrons: 260.* eds. Zuppinger A and Poretti G. Berlin: Springer-Verlag.

Hogstrom K R. Mills M D, and Almond P R. 1981. Electron beam dose calculations. *Physics in Medicine and Biology 26(3): 445-459.*

Hubbell J H and Seltzer S M. 1997. *Tables of X-ray Mass Attenuation Coefficients and Mass Energy-Absorption Coefficients from 1 keV to 20 MeV for Elements Z = 1 to 92 and 48 Additional Substances of Dosimetric Interest. NISTIR 5632(1.02).* Gaithersburg, Maryland: National Institute of Standards and Technology.

Huizenga H and Storchi P R M. 1989. Numerical calculation of energy deposition by broad high-energy electron beams. *Physics in Medicine and Biology 34(10): 1371-1396.*

ICRU. 1980. *Radiation Quantities and Units. ICRU Report 33.* Bethesda, Maryland: International Commission on Radiation Units and Measurements.

ICRU. 1984a. *Radiation Dosimetry: Electron Beams with Energies between 1 and 50 MeV. ICRU Report 35.* Bethesda, Maryland: International Commission on Radiation Units and Measurements.

ICRU. 1984b. *Stopping Powers for Electrons and Positrons. ICRU Report 37.* Bethesda, Maryland: International Commission on Radiation Units and Measurements.

ICRU. 1997. *Dosimetry of External Beta Rays for Radiation Protection. ICRU Report 56.* Bethesda, Maryland: International Commission on Radiation Units and Measurements.

Janssen J J, Riedeman D E J, Morawska-Kaczynska M, Storchi P R M, and Huizenga H. 1994. Numerical calculation of energy deposition by high-energy electron beams: III. Three-dimensional heterogeneous media. *Physics in Medicine and Biology 39(9): 1351-1366.*

Janssen J J, Korevaar E W, Storchi P R M, and Huizenga H. 1997. Numerical calculation of energy deposition by high-energy electron beams: III-B. Improvements to the 6D phase space evolution model. *Physics in Medicine and Biology 42(7): 1441-1449.*

Janovský I and Mehta K. 1994. The effects of humidity on the response of radiochromic film dosimeters FWT-60-00 and GafChromic-DM-1260. *Radiation Physics and Chemistry 43(4): 407-409.*

Jeraj R, Keall P J, and Ostwald P M. 1999. Comparisons between MCNP, EGS4 and experiment for clinical electron beams. *Physics in Medicine and Biology 44(3): 705-717.*

Jette D. 1984. The problem of electron dose calculation: I. Multiple-scattering methods. *Medical Dosimetry: Official Journal of the American Association of Medical Dosimetrists 9: 6-13.*

Jette D. 1988. Electron dose calculation using multiple-scattering theory: A. Gaussian multiple-scattering theory. *Medical Physics 15(2): 123-137. Erratum: Medical Physics 16(6): 920.*

Jette D. 1991. Electron dose calculation using multiple-scattering theory: localized inhomogeneities – a new theory. *Medical Physics 18(2): 123-132.*

Jette D. 1995. Electron beam-dose calculations. *Radiation Therapy Physics: 95-121.* ed. Smith A R. Berlin: Springer-Verlag.

Jette D. 1996. Electron beam dose calculation using multiple-scattering theory: a new theory of multiple scattering. *Medical Physics 23(4): 459-477.*

Jette D and Bielajew A. 1989. Electron dose calculation using multiple-scattering theory: second-order multiple-scattering theory. *Medical Physics 16(5): 698-711.*

Jette D and Walker S. 1992. Electron dose calculation using multiple-scattering theory: evaluation of a new model for inhomogeneities. *Medical Physics 19(5): 1241-1254.*

Jette D and Walker S. 1997. Electron dose calculation using multiple-scattering theory: energy distribution due to multiple scattering. *Medical Physics 24(3): 383-400.*

Jette D, Pagnamenta A, Lanzl L H, Rozenfeld M. 1983. The application of multiple scattering theory to therapeutic electron dosimetry. *Medical Physics 10(2):141-146.*

Jette D, Lanzl L H, Pagnamenta A, Rozenfeld M, Bernard D, Kao M, and Sabbas A M. 1989. Electron dose calculation using multiple-scattering theory: thin planar inhomogeneities. *Medical Physics 16(5): 712-725.*

Kawachi K. 1975. Calculation of electron dose distribution for radiotherapy treatment planning. *Physics in Medicine and Biology 20(4): 571-577.*

Klassen N V, van der Zwan L, and Cygler J. 1997. GafChromic MD-55: Investigated as a precision dosimeter. *Medical Physics 24(12): 1924-1934.*

Klassen N V and Ross C. 1997. Personal communication.

Knoll G F. 1989. *Radiation Detection and Measurement, 2nd Edition.* New York: John Wiley & Sons.

Korevaar E W, Dabrowski R, Janssen J J, Storchi P R M, and Huizenga H. 1996. Phase space evolution distribution functions for high energy electron beams. *Physics in Medicine and Biology 41(10): 2079-2090.*

Lax I, Brahme A, Andreo P. 1983. Electron beam dose planning using Gaussian beams: Improved radial dose profiles. *Acta Radiologica. Supplementum 364:49-59.*

Loevinger R. 1950. Distribution of absorbed energy around a point source of beta radiation. *Science 112: 530-531.*

Luo Z-M. 1985a. Improved bipartition model of electron transport. I. A general formulation. *Physical Review **B32**(2): 812-823.*

Luo Z-M. 1985b. Improved bipartition model of electron transport. II. Applications to inhomogeneous media. *Physical Review **B32**(2): 824-836.*

Luo Z-M and Brahme A. 1992. High-energy electron transport. *Physical Review **B46**(24): 15739-15752.*

Luo Z-M and Brahme A. 1993. An overview of the transport theory of charged particles. *Radiation Physics Chemistry **41**(4-5): 673-703.*

Luo Z-M, Jette D, and Walker S. 1998. Electron dose calculation using multiple-scattering theory: A hybrid electron pencil-beam model. *Medical Physics **25**(10): 1954-1963.*

McLaughlin W L, Chen Y-D, Soares C G, Miller A, Van Dyk G, and Lewis D F. 1991. Sensitometry of the response of a new radiochromic film dosimeter to gamma radiation and electron beams. *Nuclear Instruments and Methods in Physics Research **A302**: 165-176.*

McLaughlin W L, Soares C G, Sayeg J A, McCullough E C, Kline R W, Wu A, and Maitz A H. 1994. The use of a radiochromic detector for the determination of stereotactic radiosurgery dose characteristics. *Medical Physics **21**(3): 379-388.*

McLaughlin W L, Puhl J M, Al-Sheikhly M, Christou C A, Miller A, Kovacs A, Wojnarovits L, and Lewis D F. 1996. Novel radiochromic films for clinical dosimetry. *Radiation Protection Dosimetry **66**(1): 263-268.*

Meigooni A S, Sanders M F, Ibbott G S, and Szeglin S R. 1996. Dosimetric characteristics of an improved radiochromic film. *Medical Physics **23**(11): 1883-1888.*

Møller C. 1932. Zur theorie des durchgangs schneller elektronen durch materie. *Annalen der Physik **14**: 568-585.*

Molière G. 1947. Theorie der streuung schneller geladener Teilchen I: Einzelstreuung am abgeschirmten Coulomb-feld. *Zeitschrift für Naturforschung **2a**: 133-145.*

Molière G. 1948. Theorie der streuung schneller geladener Teilchen II: Mehrfach-und Vielfachstreuung. *Zeitschrift für Naturforschung **3a**: 78-97.*

Morawska-Kaczynska M and Huizenga H. 1992. Numerical calculation of energy deposition by broad high-energy electron beams: II. Multi-layered geometry. *Physics in Medicine and Biology 37(11) 2103-2116.*

Mori T. 1985. Tissue heterogeneity corrections for high energy electron treatment planning. *Japanese Journal of Radiological Technology 4: 282-286.*

Mott N F. 1929. The scattering of fast electrons by atomic nuclei. *Proceedings of the Royal Society of London A124: 425-442.*

Motz J W, Olsen H, and Koch H W. 1964. Electron scattering without atomic or nuclear excitation. *Reviews of Modern Physics 36(4): 881-928.*

Muench P J, Meigooni A S, Nath R, and McLaughlin W L. 1991. Photon Energy dependence of the sensitivity of radiochromic film and comparison with silver halide film and LiF TLDs used for brachytherapy dosimetry. *Medical Physics 18(4): 769-775.*

Nelson W R and Rogers D W O. 1988. Structure and operation of the EGS4 code system. *Monte Carlo Transport of Electrons and Photons 38: 287-305.* eds. Jenkins T M, Nelson W R, Rindi A. New York: Plenum Press.

Nelson W R, Hirayama H, Rogers D W O. 1985. The EGS4 code system. *Stanford Linear Accelerator Center Report 265.* Stanford, California: Stanford University.

Niroomand-Rad A, Blackwell C R, Coursey B M, Gall K P, Galvin J M, McLaughlin W L, Meigooni A S, Ravinder N, Rodgers J E, and Soares C G. 1998. Radiochromic film dosimetry: Recommendations of AAPM radiation therapy committee task group 55. *Medical Physics 25(11): 2093-2115.*

Niven E. 1998. *Calibration of Health Physics Instruments. A Master's Project Report.* Hamilton, Ontario: McMaster University.

Ogawa K, Nohara H, Yukawa Y, and Okada T. 1987. Absorption equivalent thickness (AET) method for electron beam treatment planning. *Japanese Journal of Radiological Technology 6: 90-93.*

Press W H, Teukolsky S A, Vetterling W T, and Flannery B P. 1992. *Numerical Recipes in Fortran 77: The Art of Scientific Computing, 2nd Edition.* Cambridge: Cambridge University Press.

Prestwich W V and Murphy R. 1999. Calculated dose response of Gafchromic MD55 film for ^{103}Pd and ^{125}I relative to ^{60}Co. *Radiation Measurements.* (in press).

Prestwich W V and Kus F. 1997. Radial dose profiles for pencil electron beams. *Radiation Physics and Chemistry 50(6): 535-543.*

Reinstein L E, Gluckman G R, and Amols H I. 1997. Predicting optical densitometer response as a function of light source characteristics for radiochromic film dosimetry. *Medical Physics 24(12): 1935-1942.*

Reinstein L E and Gluckman G R. 1999. Optical density dependence on postirradiation temperature and time for MD-55-2 type radiochromic film. *Medical Physics 26(3): 478-484.*

Rossi B. 1952. *High Energy Particles, Prentice-Hall physics series.* New York: Prentice-Hall.

Rossi B, Greisen K. 1941. Cosmic-ray theory. *Reviews of Modern Physics 13: 240-309.*

Saylor M C, Tamargo T T, McLaughlin W L, Khan H M, Lewis D F, and Schenfele R D. 1988. A thin film recording medium for use in food irradiation. *Radiation Physics and Chemistry 31(4-6): 529-536.*

Schulz R J, Almond P R, Cunningham J R, Holt J G, Loevinger R, Suntharalingam N, Wright K A, Nath R, and Lempert, G D. 1983. A protocol for the determination of absorbed dose from high-energy photon and electron beams. *Medical Physics 10(6): 741-771.*

Scott W. 1963. The theory of small-angle multiple scattering of fast charged particles. *Reviews of Modern Physics 35(2): 231-313.*

Seltzer S M. 1988. An overview of ETRAN Monte Carlo methods. *Monte Carlo Transport of Electrons and Photons 38: 153-181.* eds. Jenkins T M, Nelson W R, Rindi A. New York: Plenum Press.

Seltzer S M and Berger M J. 1985. Bremsstrahlung spectra from electron interactions with screened atomic nuclei and orbital electrons. *Nuclear Instruments and Methods in Physics Research B12: 95-134.*

Seltzer S M and Berger M J. 1986. Bremsstrahlung energy spectra from electrons with kinetic energy 1 keV – 10 GeV incident on screened nuclei and orbital electrons of neutral atoms with $Z = 1 - 100$. *Atomic Data and Nuclear Data Tables 35: 345-418.*

Soares C G and McLaughlin W L. 1993. Measurement of radial dose distributions around small beta particle emitters using high resolution radiochromic foil dosimetry. *Radiation Protection Dosimetry 47(1): 367-372.*

Spencer L V and Attix F H. 1955. A theory of cavity ionization. *Radiation Research 3:239-254.*

Sternheimer R M, Seltzer S M, and Berger M J. 1982. Density effect for the ionization loss of charged particles in various substances. *Physics Review B26(11): 6067-6076.*

Stevens M A, Turner J R, Hugtenburg R P, and Bulter P H. 1996. High-resolution dosimetry using radiochromic film and a document scanner. *Physics in Medicine and Biology 41(11): 2357-2365.*

Tulovsky V, Sandison G A, and Papiez L S. 1994. A solution to the Yang equation with electron energy loss following Harder's formula. *Medical Physics 21(9): 1377-1381.*

Vilches M, Zapata J C, Guirado D, Fernández D, Burgos D, and Lallena A M. 1999. A method to determine the in-air spatial spread of clinical electron beams. *Medical Phyiscs 26(4): 550-558.*

Werner B L, Khan F M, and Deibel F C. 1982. A model for calculating electron beam scattering in treatment planning. *Medical Physics 9(2): 180-187. Erratum: Medical Physics 9(5):784.*

Yang C. 1951. Actual path length of electrons in foils. *Physical Review 84: 599-600.*

Zerby C D and Keller F L. 1967. Electron transport theory, calculations, and experiments. *Nuclear Science and Engineering 27: 190-218.*

Zhu Y, Kirov A S, Mishra V, Meigooni A S, and Williamson J F. 1997. Quantitative evaluation of radiochromic film response for two-dimensional dosimetry. *Medical Physics 24(2): 223-231.*